# Heat Transfer in Stationary and Rotating Coolant Channels Using a Transient Liquid Crystal Technique

Justin A. Lamont

Dissertation submitted to the Faculty of
Virginia Polytechnic Institute and State University
in partial fulfilment of the requirements for the degree of

Doctor of Philosophy
in
Mechanical Engineering

Srinath V. Ekkad, Chair
Wing F. Ng
Danesh K. Tafti
Christopher J. Roy
Curtis H. Stern

October 31, 2012
Blacksburg, Virginia

Keywords: Heat Transfer, Gas Turbine Cooling, Stator Winding Cooling, Rotor Winding Cooling, Liquid Crystal Thermography

# Heat Transfer in Stationary and Rotating Coolant Channels Using a Transient Liquid Crystal Technique

Justin A. Lamont

## ABSTRACT

Heat transfer inside rotating coolant channels have a significant impact in design of gas turbine airfoils and other rotating components such as generator windings. The effects of the Coriolis acceleration and centrifugal buoyancy have a significant impact on heat transfer behavior inside such rotating coolant channels due to the complex flow patterns of coolant. Detailed heat transfer knowledge greatly enhances the designers' ability to validate numerical models of newly designed channels. A rotating experimental rig was designed and built to model scaled up coolant channels at speeds up to 750 rotations per minute (rpm). A camera is mounted onto the rotating test section and a transient liquid crystal technique is used to measure detailed heat transfer coefficients on a surface of interest. The experimental set-up is innovative, as it involves no surface heating of the test section, very little instrumentation beyond a few thermocouples and a spray coating of thermochromic liquid crystals on the test surface. To validate the test rig and the experimental method, multipass coolant channels with rib turbulators, large diameter radially outward channels with rib turbulators, and jet impingement cooling schemes are studied during rotation. 90°, W, and M-shaped rib enhancements are studied and detailed heat transfer measurements clearly capture the heat transfer enhancement mechanisms with and without rotation. Jet impingement schemes with single and double rows, normal and off-angle jets, and a cross flow outlet condition are all studied under rotation. Non-rotating studies are also performed for baseline comparisons to rotating conditions. Large aspect ratio, diverging channels with dimple and rib turbulators are studied in a stationary condition. Results for all different test geometries show good comparisons with published studies indicating that the rotating rig and experimental method are valid. Jet impingement schemes produce higher heat transfer compared to the two-pass channels with ribs, however pressure losses are significantly higher. The fewer the jets and H/d=1 produces the highest pressure losses with no significant gain in heat transfer. Off angle jets at H/d=1 produces very high pressure losses with no heat transfer advantage. A final study with radially outward coolant channels is performed with the highest rotation speeds. The structure, test section, and camera are thoroughly designed to withstand the exceptional g-forces. Heat transfer in the radial channels with and without rotation show very little effect of rotation due to the small rotation number.

This work received support from the United States Department of Energy (DOE) National Energy Technology Laboratory (NETL), Graduate Assistance in Areas of National Needs (GAANN) by the United States Department of Education, and General Electric Co. (GE Energy) out of Schenectady, NY, USA.

# Acknowledgements

I would not be here without my mother and father, Deborah and Douglas Lamont, and I would not be achieving the highest degree without their encouragement and support. I owe the world to my wife, Andrea, for her support and understanding through the countless nights of burning the midnight oil.

This work would not have been possible without the guidance and support of my primary advisor, Dr. Srinath Ekkad. His light heart and sense of humor made my graduate school experience very enjoyable. Many thanks to Dr. Mary Ann Alvin of the DOE-NETL for her support and advice in the early stages of my research. Thank you Anil Tolpadi, Gustavo Ledezma, Christopher Kaminski, and Samir Salamah of General Electric Co. (GE Energy) as my work with them has left me a stronger, more well rounded researcher and engineer. Thank you Drs. Mary Kasarda and Curtis Stern for giving me the opportunity to teach and interact with students. The teaching experience has changed my perspective on my abilities. I owe many thanks to the students in the Heat Energy and Fluids Transport Lab (HEFT) both past and present: Chris LeBlanc, Andrew Carmack, Pritish Parida, Santosh Abraham, Kapil Panchal, Colin Reagle, Jacob Delimont, Drew Newman, Sridharan Ramesh, Arnab Roy, Shreyas Srinivasan, Jaideep Pandit, Dorian Blot, Megan Thompson, Hunter Guilliams and Krishnashis Chatterjee.

Thank you Ed, Ben, Earl, and Laura for taking me under your wings and forming me into the man I am today. The skill sets and work ethic I've developed allowed me to succeed.

# Table of Contents

# List of Figures

# List of Tables

# 1. Introduction

This dissertation focuses on rotational effects on heat transfer inside cooling channels. Rotating cooling channels are used in gas turbine blades and industrial size generator rotor windings for thermal management of the materials. By extension, stationary channel heat transfer is studied to develop a baseline understanding of the rotational effects.

For gas turbines, cooling channels are used in the turbine section components where hot gases greatly exceed the material melting points, as shown in Fig. 1.1. The compressor draws in air and raises the pressure. The air enters the combustor and mixes with fuel and is ignited. The hot gases then expand out through the turbine section where the energy is extracted. The trend in the gas turbine industry is to reach higher firing temperatures which would allow more complete combustion, increasing the fuel efficiency of the engine, and increasing the performance of aircraft engines. Hot gas path components, blades and vanes, are actively cooled during operation to prevent failure due to high thermal stresses. To actively cool during operation, blades and vanes are partially hollow. Inside the blades, internal serpentine coolant channels dissipate heat from the inside out, as shown in Fig. 1.2. A common source of coolant used is air directly tapped from the compressor, which can take up to 3-5% of the compressor air (steam can also be a coolant in combined cycle power plants). The temperature of the air is around 500°C. The Reynolds Number, Re, of the coolant in the channels is typically 25,000−30,000 for aircraft engines and roughly 100,000 for industrial gas turbines for power generation. If this 3-5% of compressor air requirement can be reduced, performance will be increased.

Industrial size generators are built with stator (stationary) and rotor (rotating) coils. According to Faraday's Law, with a changing magnetic field (caused by rotating magnetic windings) an electromotive force (emf) is generated in the stator windings. This is the principle behind electrical power generation via rotating machinery. In generators, thermal management of the coils is not for failure prevention of the material, it is a mitigation of resistance loses in electrical power generation. As the coils heat up, the electrical resistance of the material increases, increasing loses. Both the rotor and stator channels are studied in this dissertation.

The research for this dissertation is experimental, therefore a transient liquid crystal technique is used. This method determines heat transfer coefficient, h, distributions inside cooling channel walls.

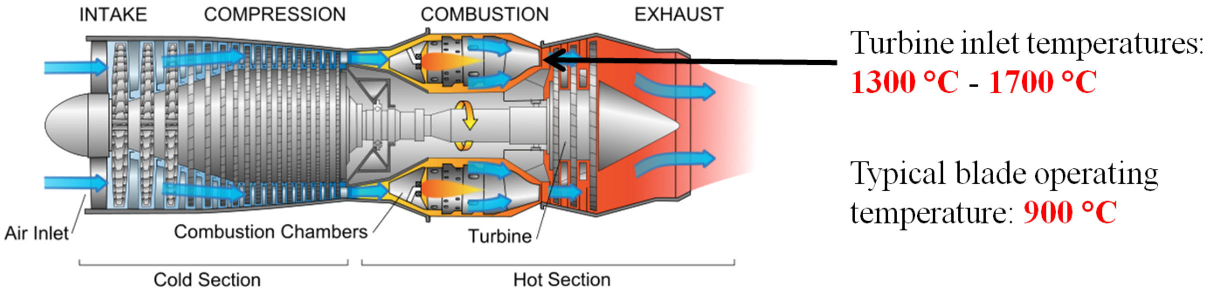

Figure 1.1: Generic gas turbine schematic. Hot gases exiting the combustor, enters the turbine section at temperatures exceeding the blade operating temperatures.

Rotating coolant channels experience two distinct phenomena: the Coriolis acceleration and centrifugal buoyancy. The Coriolis acceleration is defined as

$$a_c = -2\vec{\omega} \times \vec{V} \tag{1.1}$$

where $\vec{\omega}$ is the rotational velocity vector and $\vec{V}$ is the coolant velocity vector. The inertia of the particle and the changing reference frame of the channel creates the Coriolis acceleration. The Coriolis acceleration is dependent on the vector cross product of the rotational velocity of the system and the velocity of the coolant, so the direction of the acceleration changes. This is illustrated in Fig. 1.3, where a particle which moves radially outward from the center

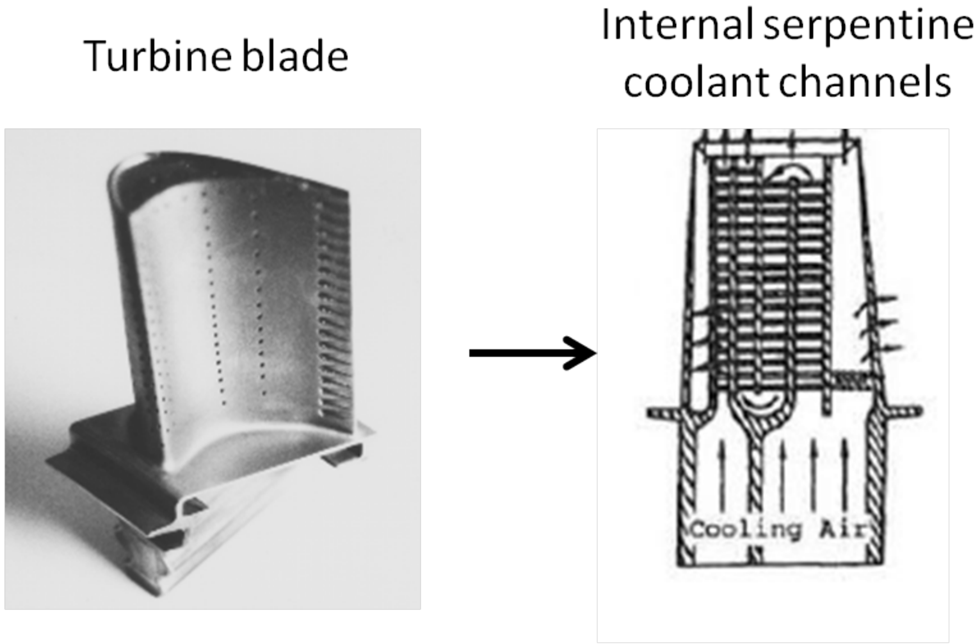

Figure 1.2: Generic gas turbine blade (left). Cutaway view of internal serpentine coolant channels inside turbine blades (right).

of rotation experiences the resulting Coriolis force in a different direction than that of the particle which moves radially inward.

The second phenomenon that occurs during rotation is centrifugal buoyancy (also referred to as rotational buoyancy). Buoyancy occurs due to the large temperature difference between the coolant and the channel walls. For natural convection situations, the Grashoff Number, Gr, is defined as

$$Gr_D = \frac{g\gamma(T_w - T_m)D^3}{\nu} \tag{1.2}$$

where g is gravity, $\gamma$ is the volumetric thermal expansion coefficient (approximately 1/T for ideal fluids, where T is absolute temperature), $T_w$ is the surface temperature, $T_m$ is the bulk fluid temperature, D is the hydraulic diameter of the channel, and $\nu$ is the kinematic viscosity of the coolant. Gr is a dimensionless ratio describing the relative importance of buoyant and

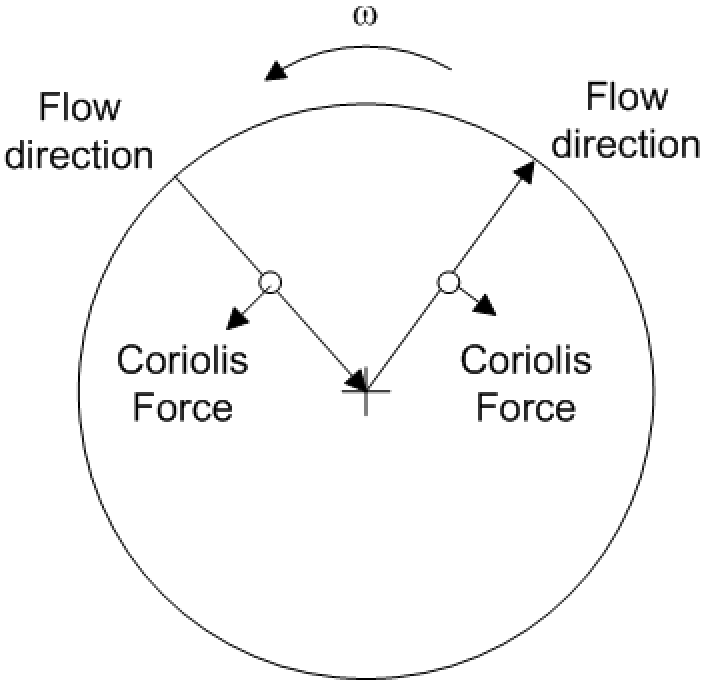

Figure 1.3: Effect of the Coriolis acceleration on a particle which moves radially outward and inward for the same rotational direction.

viscous forces acting on the fluid. For rotating conditions, centrifugal acceleration is stronger than gravity, so g from Eqn. (1.2) is with $\omega^2 R$, where R is the distance to the center of rotation. As the coolant is not driven by natural convection alone, the relative importance of natural convection in the system is calculated by

$$\frac{Gr_D}{Re^2} \tag{1.3}$$

where Re is the Reynolds number. When Eqn. (1.3) is less than one, inertial forces are dominant and buoyancy is not significant. If Eqn. (1.3) is greater than one, buoyant forces are influential on the coolant flow. During rotation, Eqn. (1.3) is known as the buoyancy parameter and can be defined as

$$BP = \frac{\Delta\rho}{\rho}\frac{R_m}{D}\left(\frac{\omega D}{V}\right)^2 \tag{1.4}$$

where $\Delta\rho/\rho$ is the coolant-to-wall density ratio, $R_m$ is the mean rotating radius and

$$Ro = \frac{\omega D}{V} \tag{1.5}$$

is the Rotation number. The rotation number defines the relative importance of rotational forces to inertial forces. In gas turbine engines, typical rotation numbers range from 0.3 to well over 1.0. Typically, buoyancy is only an issue in gas turbine blades, due to the considerable temperature difference between the metal and coolant. In generators, this temperature differential is much less extreme, therefore buoyancy is not a dominating force.

Inside the coolant channels, there are various methods of augmenting the heat transfer. This is done with ribs, dimples, pin fins/protrusions, or jet impingement. All of these methods increase the turbulence inside the channel to promote more mixing. With more mixing, there is more interaction between the coolant and the walls, increasing the heat transfer. The trade off to increasing the turbulence is to increase the pressure that is required to move the coolant through the channel. To measure how effective a cooling scheme is, the following ration is calculated

$$\eta = \frac{Nu/Nu_o}{\Delta p/\Delta p_o} \tag{1.6}$$

where Nu is the non-dimensional heat transfer of the enhanced channel, $Nu_o$ is the heat transfer of the unenhanced (typically a smooth wall) channel, $\Delta p$ is the pressure drop of the enhanced channel, and $\Delta p_o$ is the pressure drop of the unenhanced channel. Nu is defined as

$$Nu = \frac{hD}{k_f} \tag{1.7}$$

where h is the convective heat transfer coefficient and $k_f$ is the thermal conductivity of the coolant.

Experimental investigations in coolant channels of rotating machinery will benefit Computational Fluid Dynamics (CFD) modelling. Understanding the physics under these conditions, designers will have more information and tools to optimize cooling channel design which will reduce the mass flow rate of coolant required, extend operational life (for gas turbine components), and reduce electrical current losses (in generators).

The goal of this research is to develop an experimental rotating rig capable of modelling coolant channels under rotation. At the conclusion of this research, it is possible to rotate a sizeable test section to speeds in excess of 750 rpm. A camera is attached to the test section, which also rotates at 750 rpm.

# 2. Literature Survey

This section discusses the common terminology used in rotating channel heat transfer. The terminology applies to both gas turbine and generator design. Early flow distribution studies are introduced to lay a foundation of understanding in the fluid physics. An understanding of the fluid physics is critical, as this dictates heat transfer distributions. Early heat transfer studies are introduced to develop a baseline validation for the research that follows. Turbulation techniques, such as the use of ribs, dimples, protrusions and jet impingement are common in cooling designs. Studies that focus on these techniques are explored to further the understanding of heat transfer in rotating environments. A wide range of coolant channel geometries are used in practice, therefore, studies on various geometries and model orientation are explored. This research is the next step in the understanding of heat transfer in rotating coolant channels. To understand where this research picks up, the current state of the art in rotating channel heat transfer is discussed.

## 2.1 Common Terminology

Figure 2.1 shows a gas turbine blade cutaway section and profile. From an external perspective, the leading side of the internal coolant channel corresponds to the suction side of the blade, while the trailing side of the coolant channel corresponds to the pressure side of the blade. Where the coolant travels away from the center of rotation, the coolant direction is said to be radially outward. Where the coolant travels towards the center of rotation, the coolant direction is said to be radially inward. The same naming convention is also adopted for generator rotor channels.

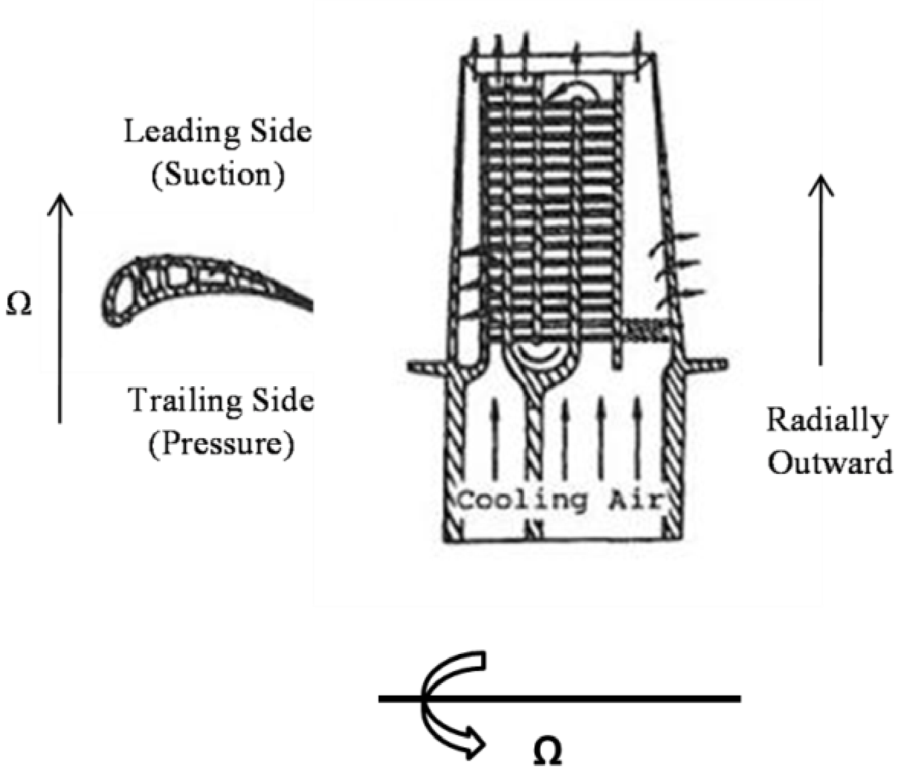

Figure 2.1: Gas turbine blade. (Left) Blade profile with leading and trailing side definitions. (Right) Cutaway view of cooling channels.

## 2.2 Early Flow Distribution Studies

Johnston et al. [1] produced one of the first studies on the effects of rotation on internal flow. As described in Han et al. [2], the experiment consisted of, ”A rotating high-aspect-ratio rectangular channeland the working fluid was water.” The experimental goal was to measure flow instability caused by rotation. The velocity and eddy viscosity distribution were measured to show the effects of flow instability. What was found was that the flow velocity and turbulence near the unstable wall (trailing side) increased with increasing rotation numbers while the stable side (leading side) experienced reductions. As a result, the wall shear stress at the unstable side increased compared to the stationary case, while the shear stress on the stable side decreased. As shown in Eqn. (1.1), the direction of the Coriolis acceleration is different if the flow is radially outward vs. radially inward. To illustrate how this affects the flow pattern within the channel, Han et al. [3] generated a drawing shown in Fig. 2.1 (modified slightly). For radially outward flow, the trailing side has a much higher velocity gradient compared to the leading side, which is consistent with Eqn. (1.1). When the flow turns, the velocity distribution flips and the leading side has the higher velocity gradient, while the trailing side velocity gradient is reduced.

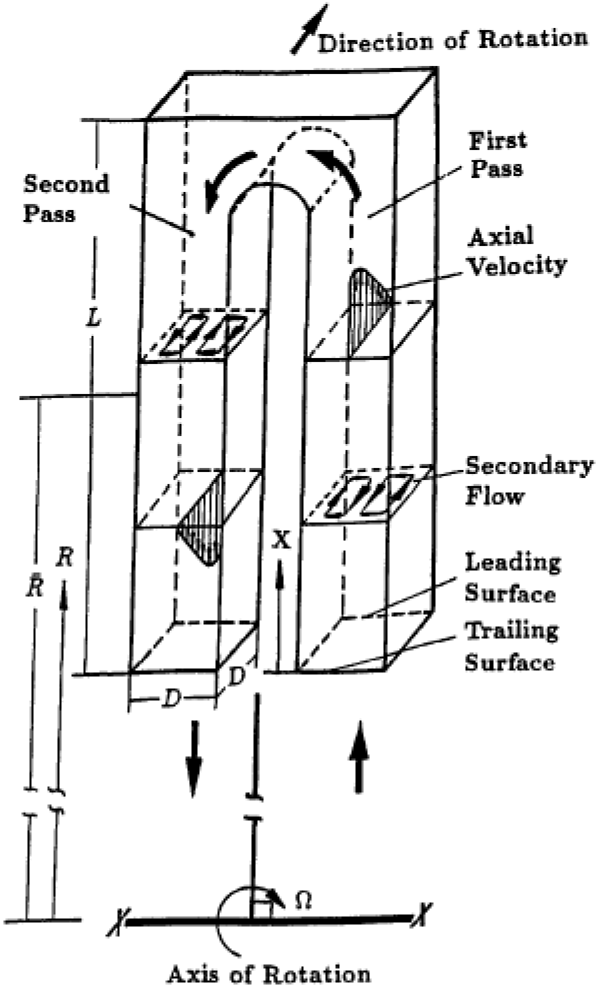

Figure 2.2: Conceptial view of a two-pass rotating coolant flow distribution (Han et al.[3]).

Johnston et al. [1] and Fig. 2.2 show the effects of the Coriolis force alone. Han et al.[3]

generated another illustration to demonstrate the combined effect of the Coriolis acceleration and centrifugal buoyancy, shown in Fig. 2.3. Figure 2.3 shows that when only the Coriolis acceleration is involved, the same velocity profile develops from Fig. 2.2. The centrifugal acceleration is always radially outward, therefore, when involved, the velocity near the trailing side of the first pass (radially outward) experiences a further enhancement of the velocity gradient, while on the second pass (radially inward) the centrifugal acceleration acts to stabilize the profile, thus reducing the velocity gradient on the leading side.

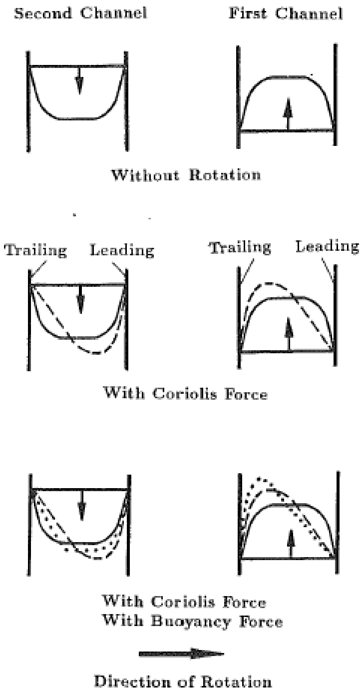

Figure 2.3: Conceptual view of individual and combined effect of the Coriolis acceleration and centrifugal buoyancy (Han et al.[3]).

## 2.3 Early Heat Transfer Studies

One of the earliest and most notable studies on heat transfer in rotating channels was produced by Wagner et al. [4]. Wagner et al. [4] rotated a test section shown in Fig. 2.4

and varied the Ro from 0 to 0.475. Figure 2.4 shows a multi-pass test section to study the effects of the flow direction and turn effects. The walls are lined with copper heaters, creating a heated wall condition. Figure 2.5 shows the results of the study with smooth walls. For the first pass, as Ro increases heat transfer enhances, agreeing with the previous flow studies of Lezius and Johnston [1]. The increased shear on the trailing side wall induces an increase in the heat transfer. The leading side experiences a reduction in the heat transfer compared to the stationary case. However, when each individual increment of Ro is studied, differences are not as clear cut as that experienced on the trailing side. The first data point shows that increased Ro shows a further reduction in heat transfer. However, closer to the turn, the higher Ro does not necessarily decrease the heat transfer. A minimum value of Ro is apparent, which decreases the heat transfer on the leading side, then as that critical Ro is reached and passed, the heat transfer begins to increase again. The second pass shows similar trends as the first pass, however, the magnitude of change is much less. The second pass leading side heat transfer increase with increasing Ro, however, individual step changes are much less than seen in the first pass. The trailing side experiences a reduction in heat transfer compared to the stationary case, however, changes between the Ro cases are significantly less than experienced in the first pass. The dramatically lower changes in heat transfer compared to the stationary case may be attributed to the turn effect encroaching into the second pass. Both the leading and trailing sides experience the turn effects, which may explain why neither vary nearly as much as in the first pass.

## 2.4 Effects of Ribs

Heat transfer augmentation inside a cooling channel is achieved with ribs which turbulate the flow. Many rib geometries, spacing, orientations, and patterns are used. One of the

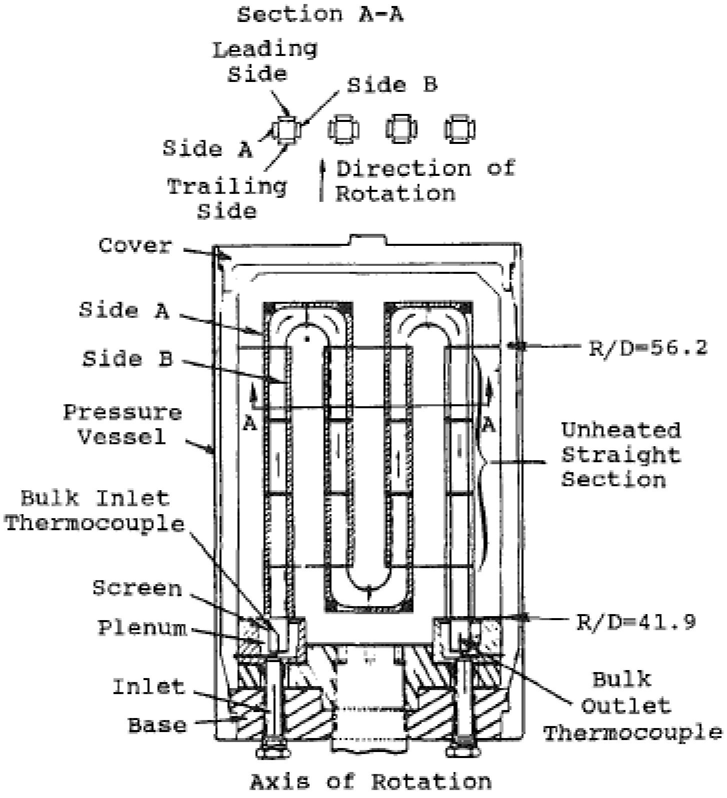

Figure 2.4: Multi-pass test section used in Wagner et al. [4]. Copper bars heat the walls.

most commonly studied rib types are the 90° ribs; ribs which are orthogonal to the direction of the coolant flow. A notable study of 90° ribs was performed by Wagner et al. [5], which applies the same setup as Wagner et al. [4]. Results are shown in Fig. 2.6. As experienced in the smooth wall study, the first pass shows the trailing side heat transfer increases with increasing Ro and the leading side heat transfer decreases with increasing Ro. Also, the average heat transfer levels are all above that experienced in the smooth wall case. The ribs trip the flow which increases the turbulence. The second pass goes according to predictions, as well. The trailing side experiences a decrease with increasing Ro, while the leading side shows an increase with higher Ro. For the second pass trailing side, similar to the smooth wall, the heat transfer is higher than the stationary, but increments of increasing Ro does not significantly change the heat transfer. This trend is also experienced in the leading side

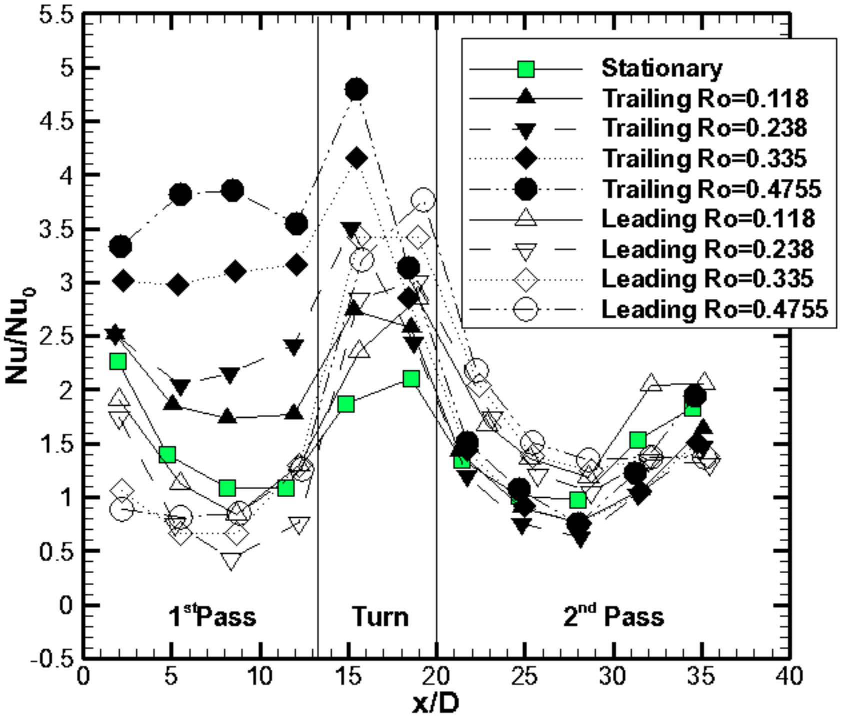

Figure 2.5: Smooth wall results for Wagner et al. [4] for Re=25,000 and density ratio=0.13 and varying Ro.

results. Taslim et al. [6] studied the effects of rotation on 90° ribs with varying blockage ratio (e/H rib heightto−channel height ratio). Results show larger blockage ratios increase the heat transfer. Parsons et al. [7] studied the effect of 90° ribs in a two pass channel. Similar trends are found between [5] and [7].

Research progressed by moving on to the effect of angled ribs instead of orthogonal. Zhang et al. [8] studied the effects of $90^o$ vs. $60^o$ ribs. Results show that for Ro=0-0.5, the $60^o$ ribs have higher heat transfer for both leading and trailing sides. Johnson et al. [9] showed that $45^o$ ribs produce higher heat transfer augmentation than the $90^o$ ribs. Zhang et al. [8] postulates that the angle of the ribs imparts a swirl to the flow, increasing the heat transfer compared to the $90^o$ ribs.

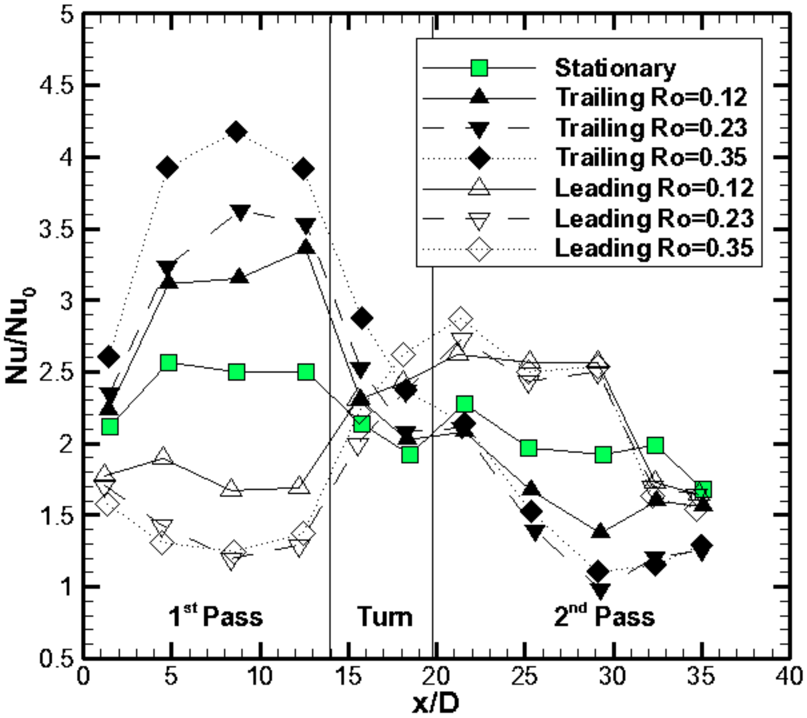

Figure 2.6: 90° ribbed wall results from Wagner et al. [5] for Re=25,000 and density ratio=0.13 and varying Ro.

More geometrically complex ribs are the V, chevron, W, M, and many other variants. Because the heat transfer was increased with angling the rib in the direction of the flow to induce swirl, having multiple angles in the direction of the flow will impart a more complex pattern thus increasing mixing and heat transfer. Taslim et al. [10] was one of the first to investigate the V-shaped ribs in a stationary environment. For e/D=0.083, the V that is pointing downstream produces the highest heat transfer, however it produces the largest friction factors. At e/D=0.125, the $45^o$ ribs produces the higher heat transfer, but produces the highest friction factors for a wide range of Re. For e/D=0.167, the V rib produces the highest heat transfer, again. The overall conclusion for [10] shows that for the largest Re range, the e/D=0.125 $45^o$ angled rib produces the highest thermal performance, $\eta$, even over similar V shaped patterns. Lee et al. [11] and Wright et al. [12] studied the thermal performance of angled, V-shaped, and W-shaped rib channels, respectively. Results for [12] show that the W-shaped ribs for a range of Re=10,000 to 40,000 produce the highest average heat transfer. Discrete ribs are discontinuous or broken ribs. Wright et al. [12] shows that discrete and continuous V and W-shaped ribs have a high performance, higher than the continuous $45^o$ ribs.

## 2.5 Dimples, Protrusions, and Jet Impingement

Other types of heat transfer enhancement techniques are the use of dimples, protrusions, pin-fins, and jet impingement. Griffith et al. [13] explored the use of hemispherical dimples for rotating channels. Results show that the leading and trailing side walls' average heat transfer increases with increasing Ro. Kim et al. [14] showed that increased dimple depth increases the average heat transfer in a channel with dimple roughened walls. When the distance between dimples increases, the average heat transfer reduces. When the channel height increases, the heat transfer reduces. Chang et al. [15] studied pin finned channels at high rotation numbers. Results show that both of the leading and trailing sides increase in average heat transfer as Ro increases. Park et al. [16] explored the use of pin fins at a $60^o$ incline. For both the leading and trailing sides, the heat transfer increases with axial distance.

Instead of using dimples, ribs, or protrusions, jet impingement schemes have been studied to increase in heat transfer in rotating channels. Parsons et al. [17] studied a cooling channel with jet impingement for the leading and trailing sides with radially outward crossflow. Stationary results show the heat transfer decreases from the beginning of the channel to the end. This occurs because the crossflow deflects the jet away from the target surface.

The further down the channel, the more crossflow develops, so the jets are deflected more. During rotation, both the leading and trailing side heat transfer results decrease below the stationary at all locations. This may be due to the development of the boundary layer inside the impingement channel, which is similar to that explained in Fig. 2.3. No matter the leading or trailing side, the jet has to penetrate the skewed velocity profile, reducing the jets effectiveness. Parsons and Han [18] studied a similar jet impingement cooling scheme as [17], however the exit condition is not crossflow. For [18], there are staggered extraction holes along the impingement surface so that there is little to no crossflow. For the stationary case, the heat transfer results stay relatively steady for the length of the channel, whereas, [17] shows a steady reduction. Results for [18] shows that the heat transfer stays constant at a level that is seen at the beginning of the crossflow channel of [17]. During rotation, a reduction in heat transfer is seen for both the leading and trailing sides, which is similar to that on [17]. Akella and Han [19] studied a jet impingement channel with two passes, where the first pass is similar to [17], the coolant has a crossflow condition radially outward. The spent coolant from the first pass then feeds the second pass jet channel which has a crossflow exit condition which is radially inward. Results show that both the first and second channel produce similar results when the test section is rotated in both directions. During rotation, all results are slightly less than the stationary case.

## 2.6 Channel Geometry and Model Orientation

Aside from studying square cross section channels, there have been many studies on the effects of aspect ratio, model orientation, and triangular channels. Figure 2.7 illustrates the cross section of a turbine blade. Figure 2.7 shows several channels which have a varying aspect ratio (AR=Width/Height) from the leading edge of the blade to the trailing edge. At the leading edge of the channel the aspect ratio is low and towards the end of the channel the aspect ratio is high. Some example studies which model rotating channels with varying aspect ratios is Griffith et al. [20], Wright et al. [21], Al-Hadhrami et al. [22], Fu et al. [23], Fu et al. [24], Zhou et al. [25], and Fu et al. [26]. Towards the leading edge of the channel the leading and trailing sides are not normal to the direction of motion. Studies that have explored the effects of channel orientation are Parsons et al. [27], Dutta et al. [28], and Park and Lau [29]. At the trailing edge of the blade, the cooling channel takes on more of a triangular geometry. Studies that have explored triangular channels are Dutta et al. [30], Dutta et al. [31], Lee et al. [32], and Liu et al. [33]. It must be recognized that many of the stated studies are combinations of aspect ratio, model orientation, and triangular channels.

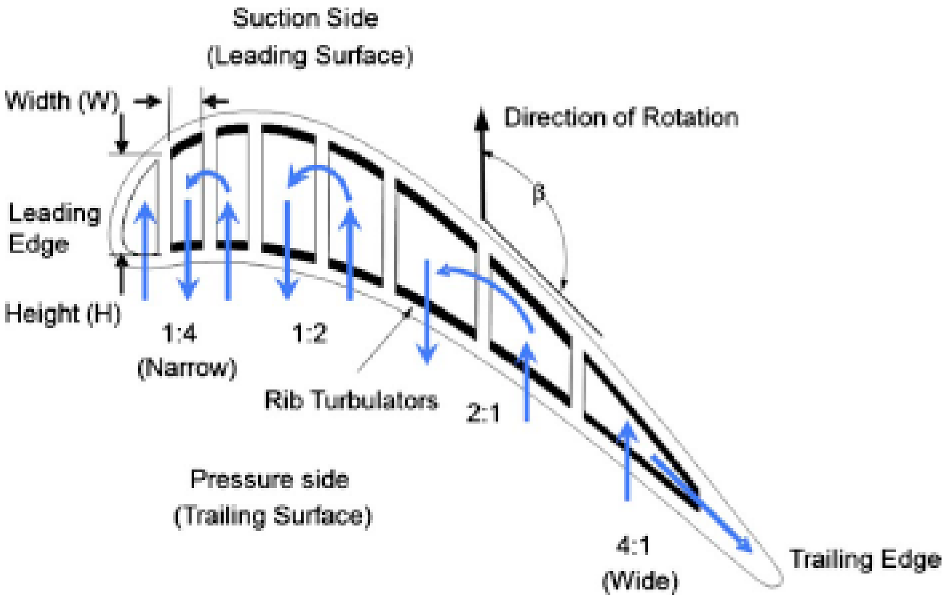

Figure 2.7: Cross section of a turbine blade and geometry of cooling channels (from Wright et al. [12]).

## 2.7 Current State of the Art

The direction this area of research is headed is to explore high Ro, High Re coolant flows with detailed heat transfer measuring techniques. Huh et al. [34] studied a two-pass channel with an AR=2:1 from Ro=0-0.45. Results are similar to previous findings in Wagner et al. [4]. Huh et al. [35] studied the effects of Ro up to 0.45 on two-pass $45^o$ rib channels and at two different model orientations. Results show that the $45^o$ ribs increase the heat transfer significantly for both the leading and trailing sides and in both passes. The ribbed channel experiences less changes in heat transfer at increasing Ro compared to the stationary case. Liu et al. [36] performed a similar study on a smooth AR=1:4 channel up to Ro=0.67. Results are consistent with previous findings. These studies are explored using copper heaters, so the measurements are able to reach steady state thus exploring both the Coriolis force and centrifugal buoyancy. The only drawback is that area average results are presented. The state of the art is to capture high rotation number effects with detailed measurement techniques. Chang et al. [37] studied a radially outward channel with two opposite walls roughened by hemispherical protrusion up to Ro=0.6 with an infrared (IR) thermography technique. The study explored both the effect of Ro and BP. For the leading side, there is a decrease in heat transfer from Ro=0-0.1, then there is a steady increase from Ro=0.1-0.6. The trailing side experiences a steady increase in heat transfer as Ro increases for all Ro. When buoyancy was increased, all heat transfer values increase as well, both leading and trailing. Chang et al. [15] studied the effects of Ro up to 0.8 for a two-pass channel with $45^o$ ribs using the IR technique. Figure 2.8 shows a sample result from the study. Results show that the trailing side first pass increases in heat transfer with increasing Ro. The leading side first pass initially decreases between Ro=0-0.3, then increases when Ro=0.3-0.8. The trailing side second pass decreases from Ro=0-0.3, then increases from Ro=0.3-0.8. The leading side second pass increases in heat transfer for all Ro.

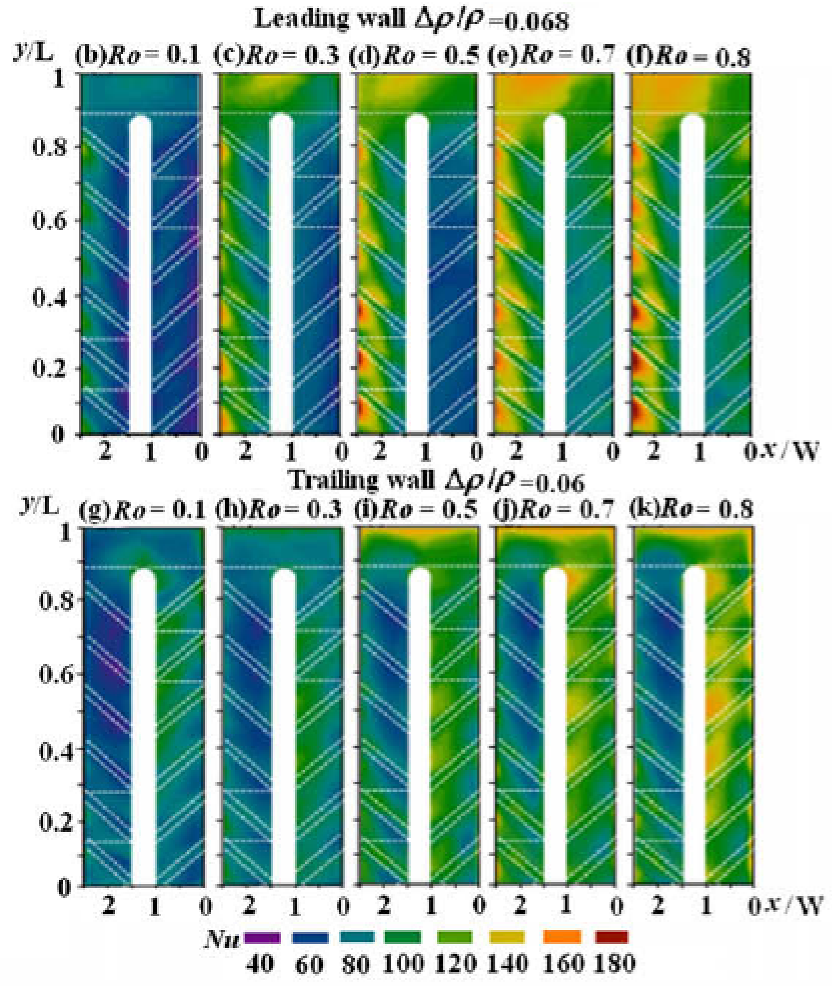

Figure 2.8: Results from Chang et al. [15]. As Ro increases so does leading and trailing side heat transfer.

## 2.8 Choice of Measurement Technique

The state of the art pushes past Ro=0.8 with detailed heat transfer measurements. The goal of this research is to explore a variety of heat transfer augmentation techniques over a wide range of Ro. A transient liquid crystal technique will be used to gather detailed measurements. This technique is described in detail in a following section. In comparison to other detailed measurement techniques, liquid crystals are the most practical. An infrared (IR) thermography technique may be applied, however the IR camera is very expensive ($20,000-60,000) so funding is not available to purchase a camera. Rotating a shared camera is not allowed as the risk for damage is too high. The IR camera is not high speed, so it cannot be stationary and film the test section as it goes by. Another technique is the use of naphthalene sublimation. This technique uses the heat/mass transfer analogy. This technique is explained in detail in Goldstein and Cho [38]. A test section is machined and naphthalene is cast into the test section to become the walls. During testing, the naphthalene sublimates. Detailed surface roughness (using a Linear Variation Differential Transformer) is measured before and after testing to determine how much naphthalene sublimated at a particular location. Data reduction must be performed immediately to reduce the effects of natural sublimation. The results are contoured, however the process is very time consuming and limited. Of the available detailed heat transfer measurement techniques liquid crystal thermography is the most practical and cost effective for the rotating channel heat transfer research.

# 3. Experimental Heat Transfer Rigs

Two separate rigs are used for this research. One is stationary and one is rotating. The rotating rig is capable of taking stationary heat transfer measurements, however, the stationary rig offers a fast, easy setup to quickly provide stationary heat transfer analyses. The following sections provide, in detail, the stationary and rotating rig setups, the differences between the two, and how test section support structures are designed for the rotating rig's tests.

## 3.1 Stationary Heat Transfer Rig

The stationary heat transfer rig is shown in Fig. 3.1. Air is provided through a hose connected to the building air supply. A gate valve is at the entrance of the rig, to control the mass flow of air entering the test section. The air passes through an orifice meter, to measure how much is entering the test setup. The air enters a settling chamber, where the air slows down and settles to an even velocity distribution. After the settling chamber, the air passes over a mesh heater. This mesh heater is connected to a DC power supply, such as an arc welder. An illustration of the mesh heater is provided in Fig. 3.2. Through resistive heating in the thin stainless steel mesh fibers, the air picks up heat before entering the test section. A sample temperature response is provided in Fig. 3.3. Interchangeable flanges are designed to fit any desired test section onto the rig.

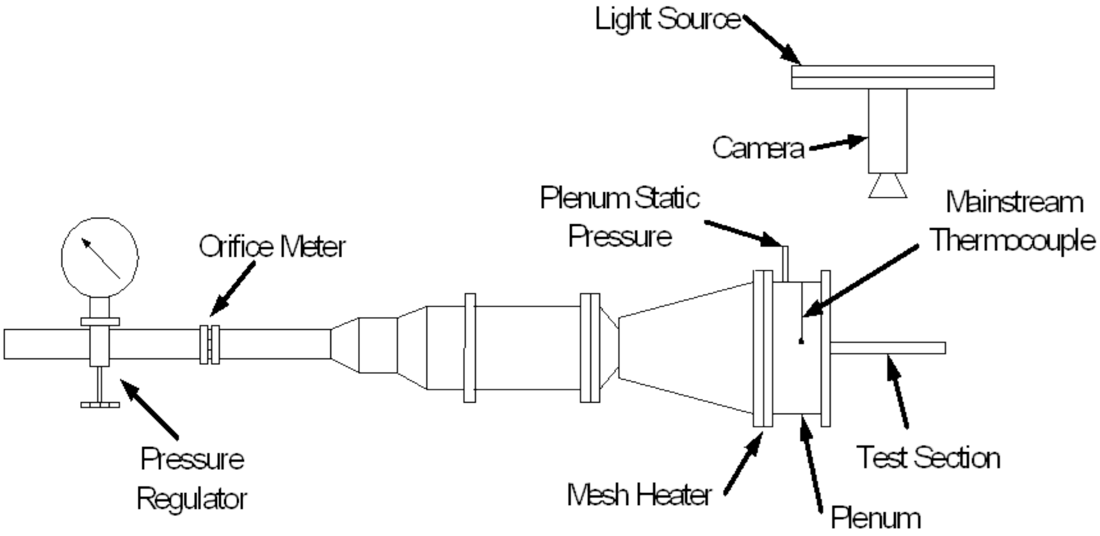

Figure 3.1: Experimental set up.

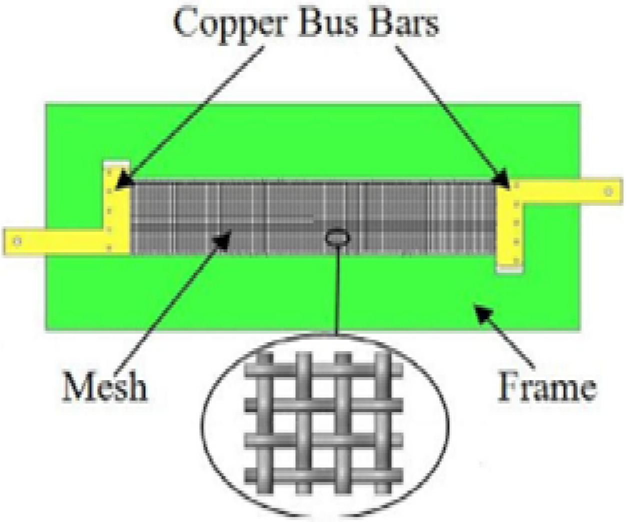

Figure 3.2: Mesh heater from [39].

### 3.1.1 Mesh Heater Transient Technique

The experimental method uses a transient liquid crystal technique. This requires a sudden injection of hot or cold fluid to cause a reaction in the liquid crystals. A mesh heater, as

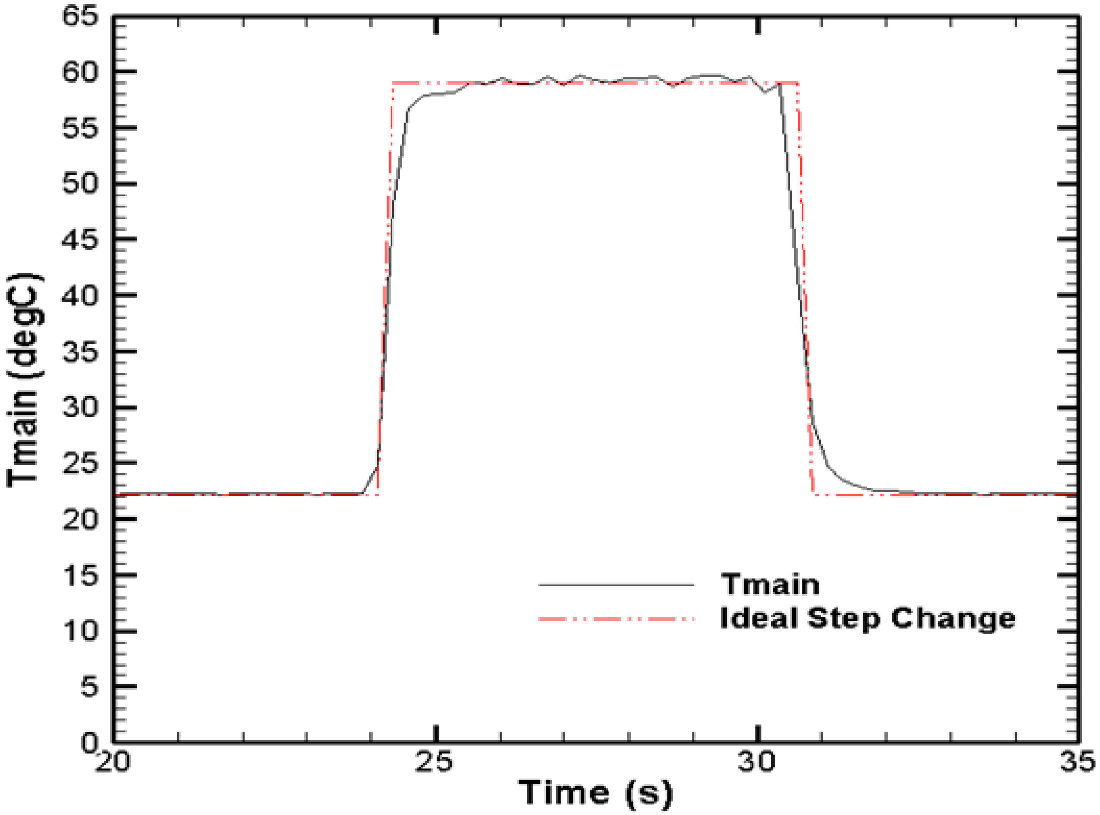

Figure 3.3: Step change in mainstream temperature obtained from mesh heater response from [39].

shown in Fig. 3.2 provided by Dhungel [39], and arc welder combination caters to this need. To perform a test, the desired flow rate of air is set. After setting the flow rate, the arc welder is turned on. Through resistive heating, the mesh almost instantaneously heats up, heating up the air as a result. This generates, for all intents and purposes, a sudden increase in mainstream temperature, as shown in Fig. 3.3.

## 3.2 Rotating Rig

The rotating rig allows the same test to be performed as seen in the stationary tests, but in a rotating frame. Figure 3.4 shows a computer aided draft (CAD) model of the rotating rig. Rig dimensions are 80in x 80in x 30in. Each beam is 3in x 4in steel welded at the joints, with a beam thickness of 1/8 in. The beams form the frame of the test rig. Ball bearing housings are located at the top and bottom of the frame. Deep groove ball bearings have a speed rating of 20,000 rpm, well above the maximum possible rotation speed. A driveshaft is mounted between the bearings. The driveshaft is made of ASTM 4130 steel with a 2 in diameter. The ends of the driveshaft are bored out 8 in axially to allow fluid to pass through the center. At the termination of the bore, a hole was tapped radially inward to reach the hollowed portion of the driveshaft. A hose may fasten into the tap, allowing coolant to continue to the test section. Figure 3.5 shows how the test section is mounted to the rotating rig. To mount the test section, two aluminum pieces were designed and machined to act as the mounting hub. The aluminum pieces are flanged to clamp around the driveshaft. A shaft key passes through the two hubs and the driveshaft, to keep the hub in place. One hub has a 2 in diameter cylindrical protrusion which allows standard weight lifting plates to be mounted, acting as the counter balance to the test section is use. Opposite of the counter balance hub is the test section hub. The test section hub has two channels drilled out to allow coolant to pass through. The coolant enters from the outside curved surface, turns $90^o$, then exits the flat end surface.

A camera is directly mounted to the test section, via a camera mount, as shown in Fig. 3.5. The weight of the camera and the weight of the mounting arm generate tensile and bending stresses in the mounting arm. The cross sectional size of the camera mount was designed accordingly to prevent failure.

The rotational speed is limited by the camera. As the camera experiences 50-60 g's during rotation, the image whites out. The components in the camera housing may shift due to the large g forces: the lens and electronics board. The camera continued to record just white, indicating the inner lens is shifting and going out of focus. To reach higher rotational speeds (thus higher Ro), a smaller, more compact camera is used. This CMOS (complimentary metal-oxide semiconductor) camera has fixed focus, reducing the sensitivity to high g forces. An epoxy potting resin was injected into the camera housing to further ensure continued operation. The non-conductive resin hardens, which minimizes shifting of internal components in the camera housing.

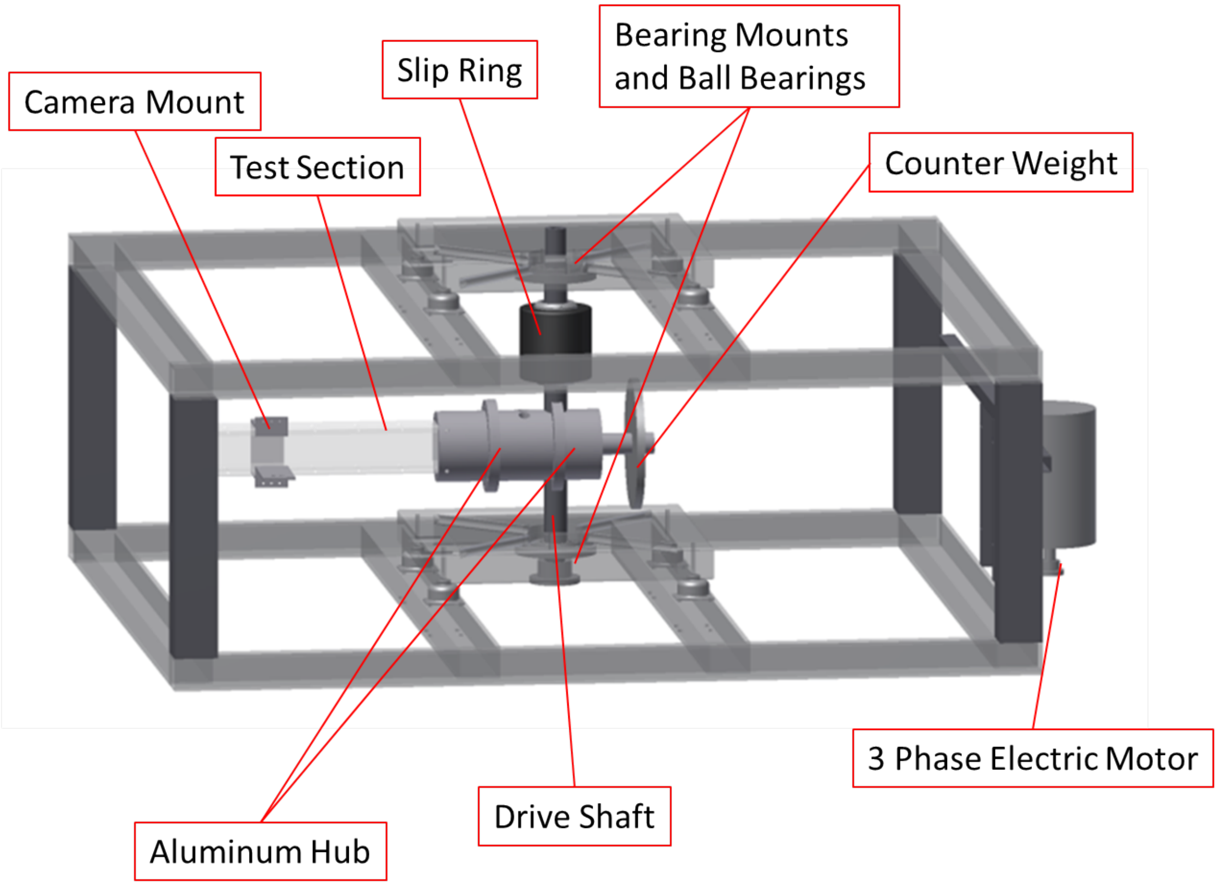

Figure 3.4: Computer aided drafting (CAD) model of the test rig.

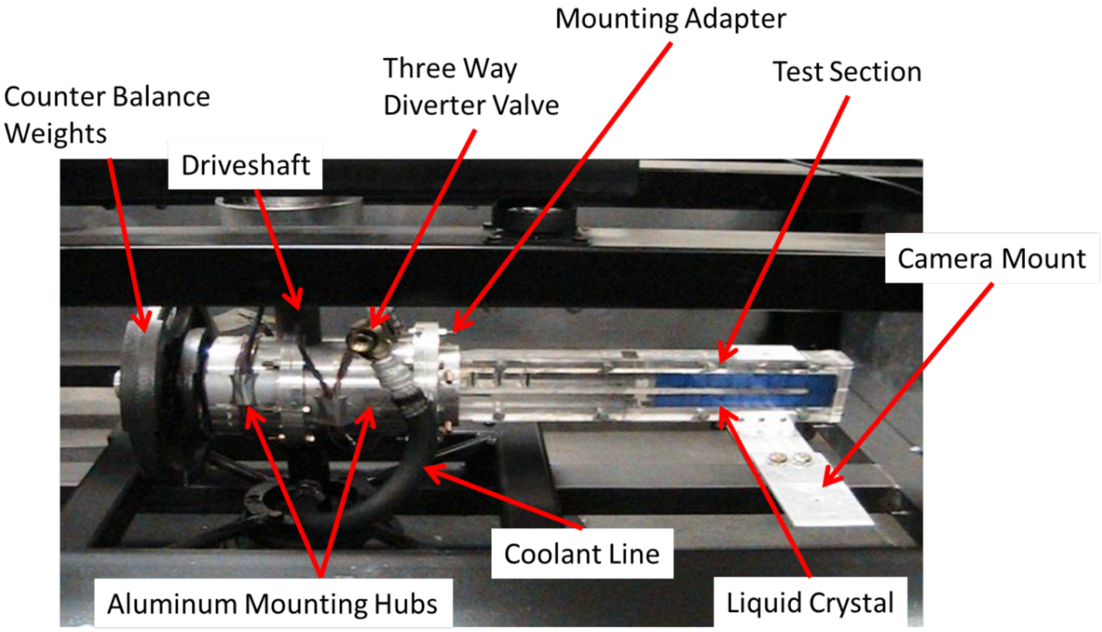

Figure 3.5: Photograph the rotating rig and labels.

### 3.2.1 Coolant Injection Method

Cool air is injected into the rotating test sections, instead of hot air to cause a reaction in the liquid crystal. To reach cold air injection, nitrogen gas is vented into the coolant path. Referring to Fig. 3.6, the coolant inlet, rotary union, and drive shaft get cooled down. The vented nitrogen exhausts to atmosphere at a three way diverter valve, shown in Fig. 3.5. A thermocouple placed at the exhaust, reads the venting temperature. Through trial and error, reaching a certain nitrogen exhaust temperature (different exhaust temperatures depending on test section type and expected flow rate of gas), a repeatable inlet temperature of air is reached. During the actual test, the nitrogen is turned off, the diverter switched to allow air to enter the test section and air is run through. The chilled coolant line becomes a heat sink, causing a step decrease in air temperature. Air is metered by an orifice meter, monitored by two digital manometers (one measuring pressure drop across the orifice plate and the other measuring upstream pressure). The flow rate calculator uses the pressure readings to

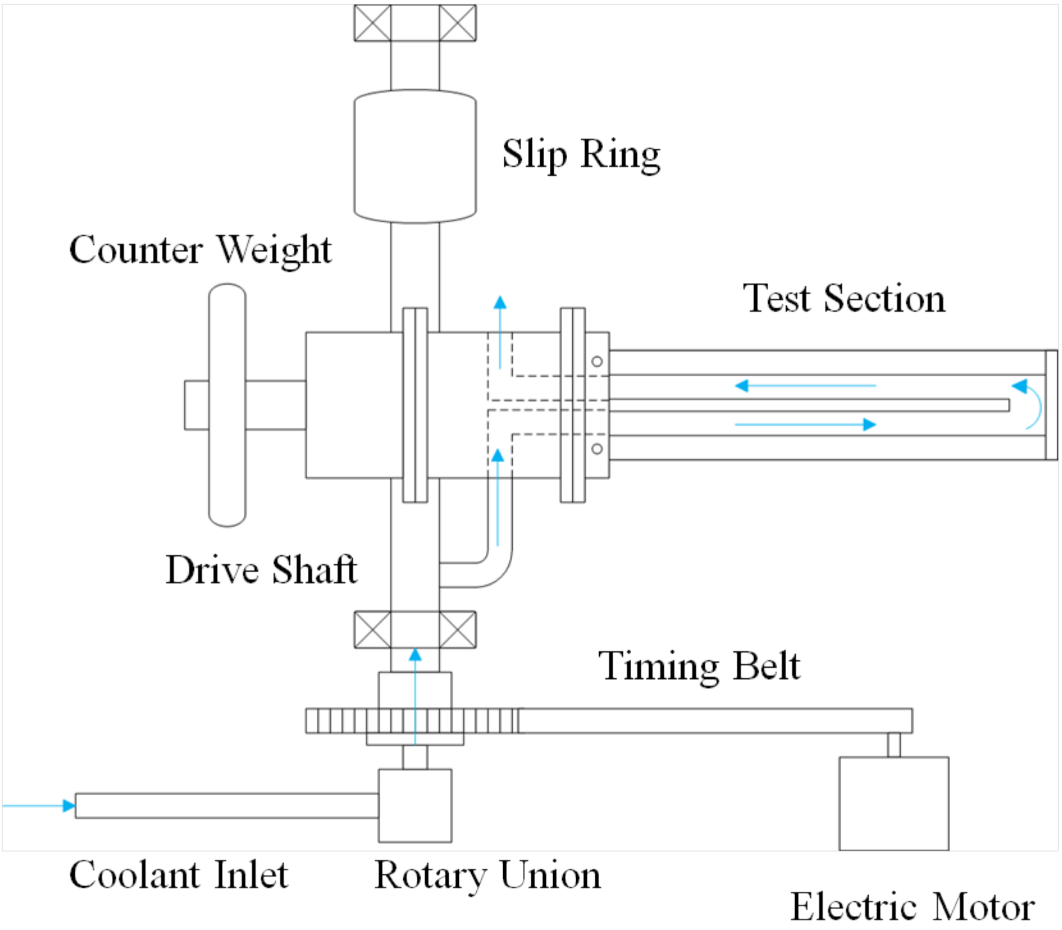

Figure 3.6: Schematic of the rotating rig.

determine the mass flow rate of air through the line. The method of measuring the flow is provided in Munson et al. [40].

### 3.2.2 Loading Calculations for Rotating Test Sections

Any given test section produces a centrifugal force during rotation. This section outlines the load calculations and accompanying stress analysis of load bearing members. Load calculation of a given test section is critical in the design of a support system, preventing catastrophic failure. A test section is rotated at speeds between 300 and 750 rpm, reaching significant centrifugal forces. Survival of the test and the safety of the test facility and personnel is vital, therefore, load bearing members are robustly designed to prevent failure. As a trade-off, excessive member size is avoided, as balancing will become more difficult.

The rotating test sections are sizeable, resulting in considerable loads. Sizeable loads must be distributed safely. The design process proceeds as follows: determine loading due to test section, determine most convenient and safe means to handle the resulting load, load due to the support itself, existing aluminum hub considerations, load due to camera and camera support, required balancing in the X and Y directions.

#### 3.2.2.1 Loading Calculations

The pieces to the test section are distributed masses, not lumped. The resulting force due to each component is calculated with a differential element approach, where the differential force is defined as

$$dF = \frac{dm * r * \omega^2}{g_c} \tag{3.1}$$

$$dm = \rho A_c dr \tag{3.2}$$

$$F = \int_{R_i}^{R_o} \frac{\rho A_c \omega^2 r}{g_c}\,\mathrm{d}r \tag{3.3}$$

$$F = \frac{\rho A_c \omega^2}{g_c} \frac{r^2}{2}\Bigg|_{R_i}^{R_o} \tag{3.4}$$

$$F = \frac{\rho A_c \omega^2}{g_c} \frac{(R_o^2 - R_i^2)}{2} \tag{3.5}$$

where dm is the differential mass, r is the distance to the center of rotation, $\omega$ is the rotational speed, $g_c$ is the gravitational constant for the English system, $A_c$ is the cross sectional area,

$\rho$ is the density of the material, $R_o$ is the outer most radius to the center of rotation, and $R_i$ is the inner most radius to the center of rotation. For all distributed masses of the test section (and entire test setup for that matter), Eqn. (3.5) is used to calculate the individual force contribution due to distributed masses.

#### 3.2.2.2 Sample Test Section

A sample test section is used to illustrate how the load is calculated. This sample is the rotor test section which models six radially outward coolant channels fed from a common plenum, as shown in Fig. 3.7. The radial cooling channels dimensions are given in Tab. 3.1. The modular test section is composed of individual components, whose individual forces combine for the total load.

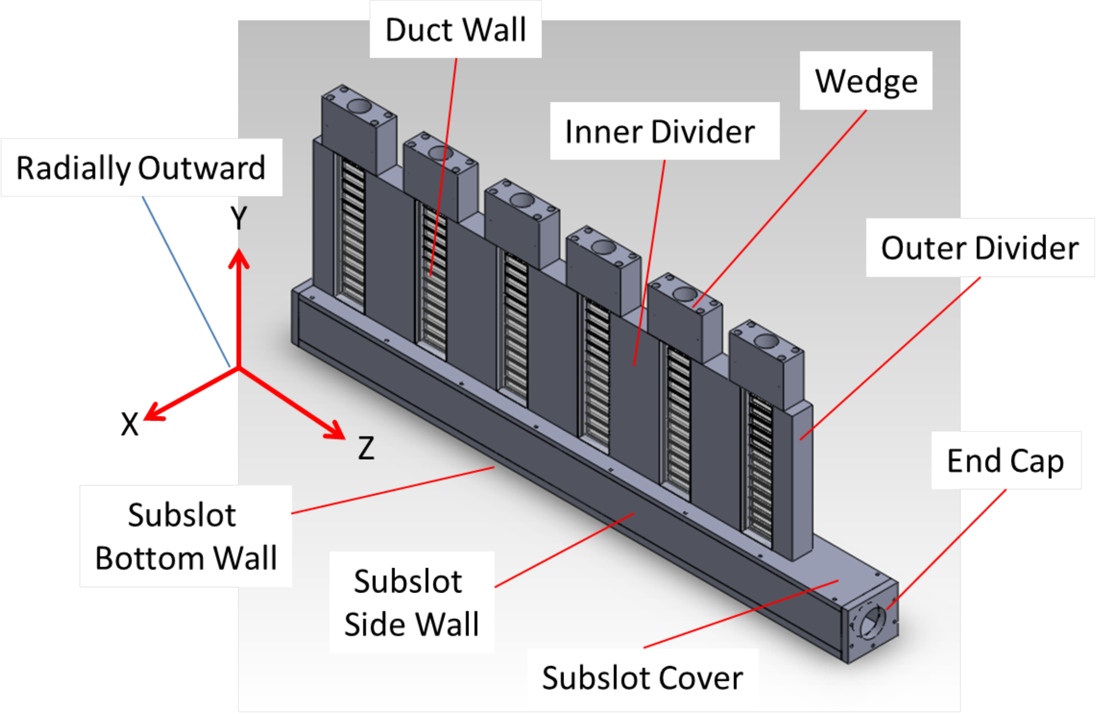

Figure 3.7: Rotor test section CAD model with cartesian coordinates.

#### 3.2.2.3 Test Section Loading Calculations

Equation (3.5) is applied to the individual pieces that the test section is comprised of, summing the forces creates the total force due to the test section. Loads of the individual pieces given in Fig. 3.7 are given in Tab. 3.1. The support must withstand at least 588.7 $lb_f$. The typical material used in these tests are acrylics or other plastics. The ultimate tensile strength of acrylic itself is approximately 8000 psi, making the test section capable of supporting its own force with the aid of bolts (for example, SAE grade 5 and grade 8 bolts), however, acrylic is very brittle. Being brittle poses a problem on the load distribution, as deflections are small (compared to ductile materials). It is not guaranteed the load is supported evenly (as bolt holes aren't in perfect alignment). leaving room for the potential of sudden catastrophic failure. Ductile hanging rods may be used instead, allowing more even load distribution.

Table 3.1: Pieces of the test section with cross-sectional areas, outer and inner radius (w.r.t center of rotation), and force contribution

| **Piece Name** | **Area** ($in^2$) | $R_o$ **(in)** | $R_i$ **(in)** | **F** ($lb_f$) |
|---|---|---|---|---|
| Inner Divider (x5) | 1.364 | 12.321 | 7.690 | 189.7 |
| Duct Wall (x12) | 0.382 | 12.321 | 7.690 | 145.0 |
| Outer Divider (x2) | 0.551 | 12.321 | 7.690 | 30.64 |
| Wedge (x6) | 1.193 | 13.871 | 12.321 | 87.23 |
| Subslot Side Wall (x2) | 5.00 | 7.52 | 6.25 | 59.78 |
| Subslot End Caps (x2) | 0.458 | 7.690 | 6.00 | 7.236 |
| Subslot Cover | 34.875 | 7.690 | 7.520 | 30.82 |
| Subslot Bottom Wall | 36.6 | 6.25 | 6.00 | 38.31 |
| | | | **Total Force** ($lb_f$) | **588.7** |

#### 3.2.2.4 Load Bearing Elements

Hanging rods are the same as bolts, but are much longer in length. They are primarily used to connect end caps of pressure vessels and hold them tight together. They are capable to sustaining high tensile loads, making them ideal for this particular situation. SAE grade 8 material hanging rods are available at $\frac{3}{8}$ in diameter and have a proof strength, $S_p = 120,000psi$. The failure mode on the hanging rods is from tensile yielding at the smallest cross section. The normal stress in the bolt is calculated by

$$\sigma = \frac{F}{A_c} \tag{3.6}$$

where F is the force due to the test section and $A_c$ is the cross sectional area of the hanging rod. The factor of safety (FOS) from tensile yielding is calculated by

$$FOS = \frac{S_p}{\sigma} \tag{3.7}$$

where $S_p$ is the proof strength of the rod. Four rods are used to handle the load. Characteristics of the rods are in Tab. 3.2.

Table 3.2: Characteristics of the hanging rods.

| | |
|---|---|
| $S_p$ (ksi) | 120 |
| $D_{rod}$ (in) | $\frac{3}{8}$ |
| $A_c$ $(in^2)$ | 0.078 |

Forces will be generated by the rods themselves, as well as the end plates, which hold the test section in place. Before stresses are calculated on the rod, these two additional forces must be added to the test section load.

#### 3.2.2.5 Force due to load Bearing Elements

The force due to the rods is calculated with the differential element method, as they have a distributed mass. Table 3.3 shows the force contribution of the individual rods.

End plates at the end of the handing rids hold the test section in place. Bending stresses

Table 3.3: Force contribution due to rod weight

| | |
|---|---|
| $\rho_{steel}\left(\frac{lb_m}{in^3}\right)$ | 0.28 |
| $A_c(in^2)$ | 0.110 |
| $R_o$ (in) | 6.75 |
| $R_i$ (in) | 4.5 |
| $F_{rod}(lb_f)$ | 32.47 |

occur in the end plates, which is the primary mode of failure. Therefore, the cross section of the end plate is designed to withstand the bending stresses. Bending stress is defined as

$$\sigma_b = \frac{My}{I} \tag{3.8}$$

where M is the bending moment, y is the distance from the outside edge to the centroidal axis, and I is the second moment of area, where for a rectangular bar

$$y = \frac{1}{2}c \tag{3.9}$$

$$I = \frac{1}{12}bc^3 \tag{3.10}$$

where c is the height of the cross section of the bar and b is the base length of the cross section of the bar. The base of the end plate can not be larger than 0.8 in, as it will obstruct the coolant exiting the radial channel. Cross section dimensions are designed to achieve an acceptable factor of safety in bending. Centrifugal loads due to the end plates are calculated, as shown in Tab. 3.4. According to Tab. 3.4, a robust factor of safety is reached with the specified dimensions and the load due to the plates themselves are calculated. The forces from the rods and the end plates are added into the total stress analysis of the rods.

Table 3.4: Material characteristics, dimensions, loading, factor of safety, and load contribution for the end plate support

| | |
|---|---|
| $S_y(Al-2024T3)(ksi)$ | 50 |
| Bolt-to-Bolt distance, L (in) | 2.625 |
| Bending Moment, M (in-$lb_f$) | 437 |
| Base, b (in) | 1.00 |
| Height, c (in) | 0.75 |
| I ($in^4$) | 0.063 |
| y (in) | 0.50 |
| $\sigma_b$ (psi) | 3505 |
| $FOS_{bending}$ | 14.3 |
| $\rho_{Al}(\frac{lb_m}{in^3})$ | 0.0979 |
| $A_c(in^2)$ | 1.97 |
| $R_o(in)$ | 13.321 |
| $R_i(in)$ | 12.321 |
| $F_{plate}(lb_f)$ | 39.5 |

#### 3.2.2.6 Combined Loading

The loads due to the test section, rods, and end plates are summed to calculate the integrity of the hanging rods. The resultant force acts on the rods and two considerations must be made. First, rods are threaded into the aluminum hub. Calculations are made to ensure threads are not stripped out of the aluminum. Second, the bolts themselves cannot not yield under these loads. Table 3.5 shows the final results of these calculations. The large factors of safety indicate the threads and rods are strong enough to hold the required loads.

#### 3.2.2.7 Aluminum Hub Loading

Two aluminum hubs wrap around the drive shaft. One side is the mount for the test section and the loading structures, the other side is the counter balance hub, as shown in the schematic of Fig. 3.6. Force balance calculations, in both the X and Y directions, determine how much counter weight is required. The cumulative force analysis on the test section is

Table 3.5: Thread shearing and rod yielding calculations for the combined loading

| | |
|---|---|
| **Thread Shear** | |
| $S_{y,Al}(ksi)$ | 10 |
| $D_{rod}(in)$ | $\frac{3}{8}$ |
| Thread Depth (in) | 1.5 |
| $A_{shear}(in^2)$ | 1.353 |
| $T_{shear}$ (psi) | 147.4 |
| $FOS_{shear}$ | 39.16 |
| **Rod Yield** | |
| $A_c(in^2)$ | 0.078 |
| $\sigma_{yield}(psi)$ | 2573 |
| $FOS_{yield}$ | 46.6 |

also used on the aluminum hubs, to determine specific loading. Table 3.6 shows the results of this analysis. The loads of the aluminum hubs combine with the test section, hanging rod, and end plate loads. The camera is mounted onto the test section, loads are included in the final force balance calculation.

Table 3.6: Force contributions of the aluminum mount and counter weight hubs.

| | |
|---|---|
| Testing Mount Hub | 881.85 $lb_f$ |
| Counter Weight Hub | 564.28 $lb_f$ |

#### 3.2.2.8 Camera Mounting

The camera used is a $VeHo^{TM}$ MUVI microcamcorder, which has a CMOS (complimentary metal oxide semiconductor) chip for creating digital images. It is chosen because of its compact size and small mass. The camera is fixed focus. As previously discussed, with a variable focus camera, the inner lens shifts under high g-forces. By injecting the camera with electronics potting epoxy, the contents in the camera casing do not shift (as the resin hardens locking electronics in place). There is theoretically no rotational speed limit on the camera. The mass of the camera is approximately 0.06 *kg*. A series of tests on a a 1 in x 1 in grid system, determined the distance the camera must be from the test section. The camera is placed at three distances away from the grid, capturing the width and height dimensions. The resulting equations for capturing the width and height of the test surface are

$$W_{TS} = 0.9386\Delta x - 0.9737 \tag{3.11}$$

$$H_{TS} = 0.6623\Delta x - 0.8553 \tag{3.12}$$

Rearranging and solving Eqns (3.11) and (3.12), to view a channel of dimensions (4.621 in x 1.15 in), a minimum distance of 6.0 in is required between the camera and the test section. The X and Y forces along with the resultant force are calculated in Tab. 3.7. The force in the X-dir is added to the balancing calculations. The force in the Y-direction is added to the Y-dir balancing. The designed camera support provides three degrees-of-freedom for camera placement. T-slotted aluminum struts, as shown in Fig. 3.8, are used as the camera support. Using the same method of determining loading due to centrifugal force, Tab. 3.8 shows the resultant loads caused by the camera mount.

Table 3.7: Mass and resulting load due to the camera in the x and y directions.

| | |
|---|---|
| Mass (kg) | 0.06 |
| $F_x(lb_f)$ | 5.1883 |
| $F_y(lb_f)$ | 7.98 |
| F $(lb_f)$ | 9.52 |

#### 3.2.2.9 Final Balance Calculations

Table 3.8 lists all of the components and their loading contributions. The counter balance hub force must be subtracted because it's force opposes that of the test section, testing mount hub, rods and plates, and the camera and camera mount. The required counter weight in the X-dir is shown in Tab. 3.9. The required counter weight in the Y-dir is shown in Tab. 3.10.

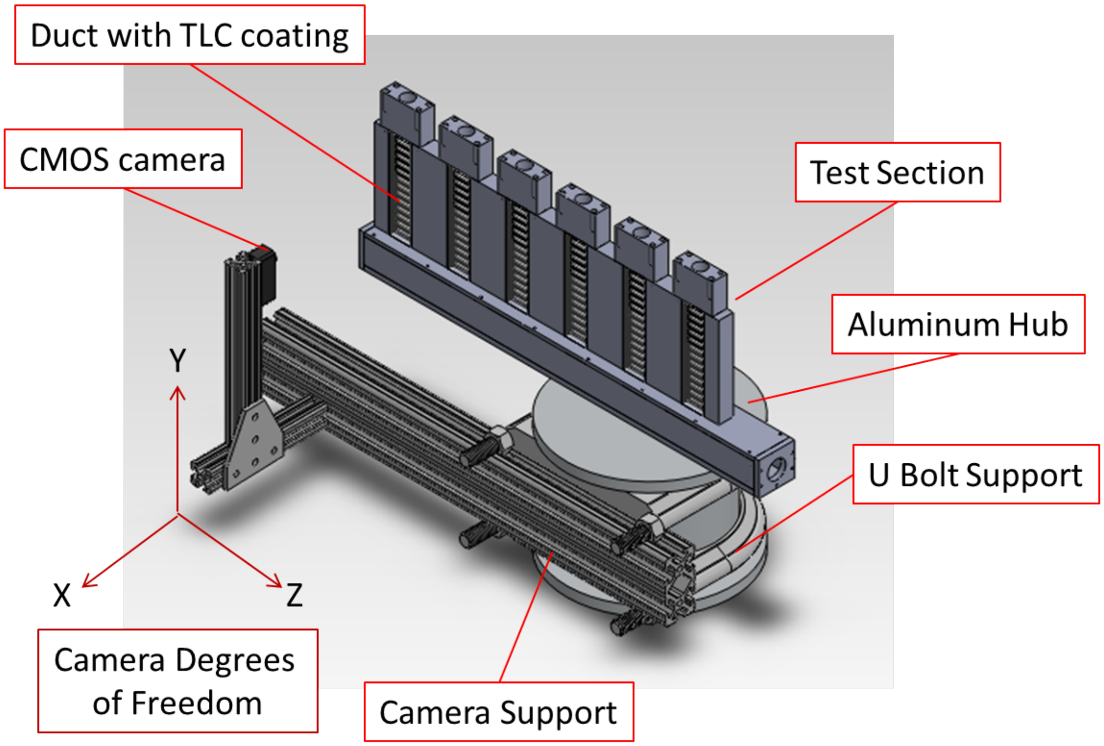

Figure 3.8: Camera support mount and camera degrees of freedom.

Table 3.8: Individual loads from components and the total unbalance force and unbalance moment.

| | Force ($lb_f$) |
|---|---|
| Hanging Rods (x4) | 129.9 |
| Load Plates (x2) | 78.9 |
| Test Section | 588.7 |
| Testing Mount Hub | 881.9 |
| Counter Balance Hub | 564.3 |
| Camera and Camera Mount | 517.8 |
| Total Unbalance Force | 1404 |
| Total Unbalance moment ($lb_m in$) | 87.9 |

#### 3.2.2.10 Stresses on Counter Weight Hub

With the required force balance, it is critical to determine if the counter weight hub can sustain the stresses. Three modes of failure on the hub are: tensile yield, Edge Shearing,

Table 3.9: Balancing masses and locations required to balance the rig in the x-direction.

| Mass ($lb_m$) | Center of Mass (in) |
|---|---|
| 10 | 8.79 |
| 20 | 4.40 |
| 30 | 2.93 |
| 40 | 2.20 |
| 50 | 1.76 |

Table 3.10: Balancing masses and locations required to balance the rig in the y-direction.

| Mass ($lb_m$) | Center of Mass (in) |
|---|---|
| 1 | 24.4 |
| 2 | 12.2 |
| 3 | 8.13 |
| 4 | 6.10 |
| 5 | 4.88 |
| 6 | 4.07 |

and bearing stress failure. Two locations have stress concentrations: the filleted shoulder where the hub diameter steps down from 6.5 in to 2 in and where the counter weight arm is drilled through for the locking bolt. Stress concentration factors are estimated based on the round shaft with shoulder fillet model and the bar in tension with a transverse hole.

The counter weight arm is the same diameter of a standard weight lifting bar, 2 in. A 5/8 in bolt is inserted all the way through the counter balance arm, keeping the weights in place. This decreases the cross sectional area of the counter weight arm and introduces a stress concentration. To approximate the stress concentration factor, the arm is modelled as a bar with a hole through it. Using Budynas et al. [41], the stress concentration factor is approximately 2.35. Where the diameter of the counter weight hub steps down from 6.5 in to 2 in is another area of concern is where. There is a 0.125 in fillet at this shoulder. To approximate the stress concentration factor, the arm is modelled as shaft shoulder with a fillet in tension. Using, again, Budynas et al. [41], the stress concentration factor is approximately

2.33. Table 3.11 shows the resulting stresses and factor of safety of the counter weight arm with the stress concentration factors.

Table 3.11: Factor of safety calculations for the counter weight arm with two stress concentration considerations.

| Bar with hole in tension | |
|---|---|
| $D_{bolt}/D_{arm}$ | 0.3125 |
| $K_t$ | 2.35 |
| $A_c$ | 1.892 |
| $\sigma_{nominal}$ | 742 |
| $\sigma_t$ | 1744 |
| $FOS$ | 5.735 |
| Shaft shoulder with fillet | |
| $r_{fillet}/D_{arm}$ | 0.0625 |
| $D_{hub}/D_{arm}$ | 3.25 |
| $K_t$ | 2.33 |
| $A_c$ | 3.142 |
| $\sigma_{nominal}$ | 447 |
| $\sigma_t$ | 1041 |
| $FOS$ | 9.61 |

### 3.2.3 Lighting Method

Liquid crystal thermography requires a light source to view the changing colors of the liquid crystal. liquid crystal data may be processes in two ways: a green start method or hue calibration method. The first method is based on the RGB (Red, Green, Blue) color classification system that is the default for many cameras and programs (i.e. MATLAB). The RGB classification gives a value from 1-255 depending on how much red, green, or blue is present in a particular pixel. The green start method notes when a particular pixel has reached a fixed value of green, then calculate the appropriate heat transfer coefficient. This assumes all pixels begin at the same value of green (theoretically zero when TLC is black) and that the test area is evenly lit. Having even lighting is crucial, as the value of green changes depending on the intensity of the light. The hue calibration technique uses a different classification of colors. The RGB color system can be converted into a HSV (Hue, Saturation, and Value) system. The advantage of this is that color purity is seperated from the intensity of the light source. This relaxes the strict need of even lighting over a test surface. This is convenient, as there is limited space on the test section to mount lights. Lights must be placed in such a way that they do not give a glare in the video. Bulky lighting systems cannot be used, as the lights, support structure, and power source would add too much needless mass to the rotating system. Instead, small high powered LEDs are used to illuminate the test section.

# 4. Liquid Crystal Thermography

Liquid crystal thermography is a testing method to determine convective heat transfer coefficient distributions on a surface of interest for cooling applications. The heat transfer coefficient appears in Newton's law of convective cooling:

$$q" = h(T_m - T_w) \tag{4.1}$$

where q" is the heat flux from a solid surface, h is the heat transfer coefficient, $T_m$ is the bulk fluid temperature, and $T_w$ is the solid surface temperature. The heat transfer coefficient, h, describes how well heat is exchanged from the solid surface to the bulk fluid. For complex flow conditions, liquid crystal thermography reveals the detailed heat transfer coefficient distributions which may not be represented in theoretical and empirical formulae. The proceeding sections describe the history of and how liquid crystal thermography is performed and analysed.

## 4.1 What are Thermochromic Liquid Crystals?

Cooper et al. [42] provides an excellent background on the initial discovery and description of thermochromic liquid crystals (TLCs). Discovered by an Austrian botanist, Friedrich Reinitzer, in 1888, liquid crystals exhibit the fluidity of a liquid while at the same time maintaining a degree of anisotropic, ordered structure of a crystalline solid. There are three main catagories of liquid crystals: smectic, nematic, and cholesteric; the particular category being determined by the molecular structure of the liquid crystal. Of particular interest to heat transfer studies is the optical properties exhibited when presented with certain fields, such as: electrical, magnetic, shear, pressure, and thermal. For heat transfer studies, changes in the thermal field produces changes in the light transmitting and scattering properties of the crystals of thin films of liquid crystal materials. The changes in optical properties produces different perceived colors. These property changes allow for qualitative and quantitative heat transfer information. Liquid crystals may be applied to surfaces by simply using an airbrush.

For heat transfer applications, crystals that respond to temperature are desired. Over a reproducible range of temperatures, the light reflected from the crystals progress through all colors of the visible spectrum, as the crystal folds and unfolds in response to the thermal changes. The early applications of liquid crystals were unencapsulated (or unprotected), which exhibit brilliant colors. However with exposure to ultraviolet (UV) radiation and atmospheric contamination, deterioration is rapid, allowing only a few hours of experimentation. Now, liquid crystals are encapsulated in a polyvinyl alcohol binder, greatly extending their workable life from hours to years. The drawback is that the variation and brilliance of color is greatly reduced due to viewing angle. The following sections describe how the optical properties of liquid crystals are used to measure heat transfer.

## 4.2 Derivation of Working Equation

Liquid Crystal Thermography determines the convective heat transfer coefficient on a surface exposed to a fluid. The one-dimensional heat equation is used to create a model

$$\frac{\partial T}{\partial t} = \alpha \frac{\partial^2 T}{\partial x^2} \tag{4.2}$$

where T is temperature, t is time, x is the normal distance into the solid, and $\alpha$ is the thermal diffusivity of the solid material. It is assumed that the surface is infinitely thick, so that heat conducts predominantly in one direction. A convection boundary condition is applied to the surface

$$-k_w \frac{\partial T}{\partial x} = h(T_\infty - T_s) \tag{4.3}$$

where $k_w$ is the thermal diffusivity of the solid material. The left hand side of Eqn.(4.3) is Fourier's law of conduction and the right hand side is Newton's law of convective cooling. The boundary conditions shows the coupling of conduction within the solid material and convection due to a fluid passing over the surface. Applying (4.3) to (4.2) generates the solution

$$\frac{T(x,t) - T_i}{T_m - T_i} = erfc\left(\frac{x}{2\sqrt{\alpha t}}\right) - exp\left(\frac{hx}{k_w} + \frac{h^2 \alpha t}{k_w^2}\right)\left[erfc\left(\frac{x}{2\sqrt{\alpha t}} + \frac{h\sqrt{\alpha t}}{k_w}\right)\right] \tag{4.4}$$

which describes the temperature on the surface and into the solid as a function of x for a given bulk fluid temperature, $T_m$. Liquid crystals are applied to the surface of a solid (x=0), therefore (4.4) reduces to

$$\frac{T(0,t) - T_i}{T_m - T_i} = 1 - exp\left(\frac{h^2 \alpha t}{k_w^2}\right)\left[erfc\left(\frac{h\sqrt{\alpha t}}{k_w}\right)\right] \tag{4.5}$$

which becomes the mathematical model for liquid crystal thermography. Only T(0,t) varies with time, so if a constant bulk fluid temperature is introduced at time t=0 s, the heat transfer coefficient, h, can be solved for iteratively (as an explicit solution is not possible). Liquid Crystal Thermography relates the color reflected off of the liquid crystals to a wall temperature. When this relation is determined, h can be solved.

## 4.3 Experimental Setup

The following section describes the experimental process. The process begins with the application of liquid crystals on the surface of interest. As, the two test setups were described in the *Experimental Heat Transfer Rigs* chapter, the testing equipment is described along with the testing conditions.

### 4.3.1 Solid Material Choice and Liquid Crystal Application

As described in Cooper et al. [42], liquid crystals are applied to a test surface with an air brush. The type of surface chosen for application depends on the situation of testing. For closed channel studies, the liquid crystal layer must be viewed through the material, therefore optically clear materials are desired. Clear acrylics such as plexiglass or lexan are chosen due to their optical clarity. Liquid crystals are applied first, then a black backing on top. An illustration of this is in Fig. 4.1.

Typically, the thickness of the liquid crystal layer is 60 $\mu$m, according to [42]. In this research, the thickness is not directly measured, the coating is considered sufficient when the view through the clear acrylic test piece is cloudy (before applying black backing). The thickness of the black backing in similar to that of the liquid crystals. The thickness of the black backing is considered sufficient when no visible light penetrates through.

Acrylics are ideal for this testing method because of their low thermal diffusivity, $\alpha$ from Eqn. (4.3). The tests are transient, lasting between 15-40 s, therefore the low thermal diffusivity reduces the conduction losses of the experiment, generating pure convective heat transfer results.

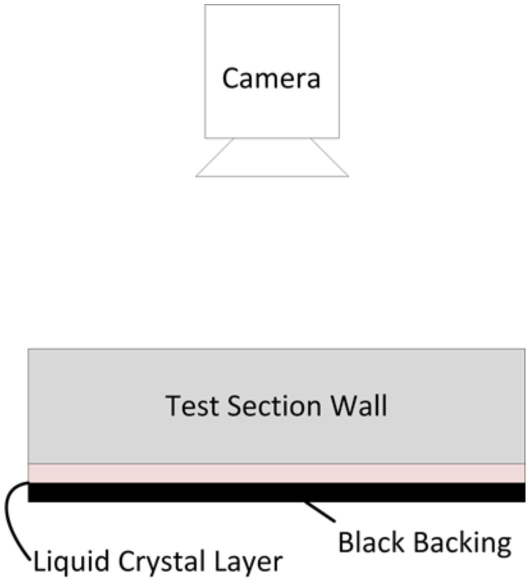

Figure 4.1: Illustraion of how TLC and black backing are applied to a surface for color capture.

### 4.3.2 Testing Equipment

Liquid Crystal Thermography uses changes in colors reflected by the liquid crystal to infer surface temperatures. A video camera is used to capture the light reflected over time, as shown in Fig. 4.1. Thermocouples are used to capture the bulk fluid temperatures over time. For cooling channel studies, the bulk inlet and outlet mainstream temperatures are measured and the local fluid temperature is interpolated between the inlet and outlet. An illustration of this is shown in Fig. 4.2. Depending on how long the test section is, multiple bulk fluid temperatures may need to be measured, as the fluid temperature will drop with distance. Another thermocouple is used to calibrate the liquid crystal color with temperature; this will be further discussed in the *Data Reduction Procedure* section. As discussed in the Experimental setup, either a mesh heater of nitrogen cooled method is used to introduce a step change in temperature into the test section.

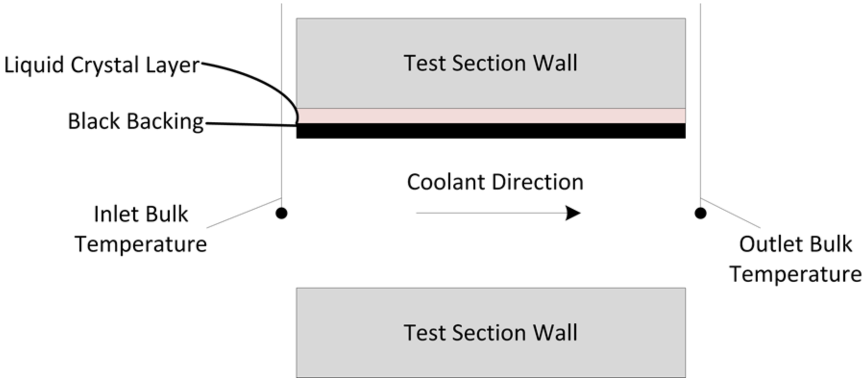

Figure 4.2: Cooling channel with TLC coating and inlet/outlet bulk fluid temperature thermocouples.

### 4.3.3 Testing Conditions

Once the test section is constructed and applied with liquid crystal, a transient test is performed. Recalling Eqn. (4.5), T(0,t) changes with time given a *constant* $T_m$. This is applied in practice by having the test section and mainstream at thermal equilibrium. At time, t=0 s, a step increase (or decrease) in $T_m$ is introduced, as shown in Fig. 4.3. An example of the heated temperature response is illustrated in Fig. 4.3. The video camera then records the response in the liquid crystals.

An important consideration is to use an appropriate mainstream temperature to induce a steady color change in the liquid crystals. In stationary situations, it does not matter what temperature the bulk fluid temperature is, as long as it induces a color change in the liquid crystal. The limit on the bulk fluid temperature is that it should not be high (or low) enough to cause buoyancy, if buoyancy effects are not desired. Further considerations and limitations on the transient liquid crystal technique are discussed in the *Experimental Uncertainty* section.

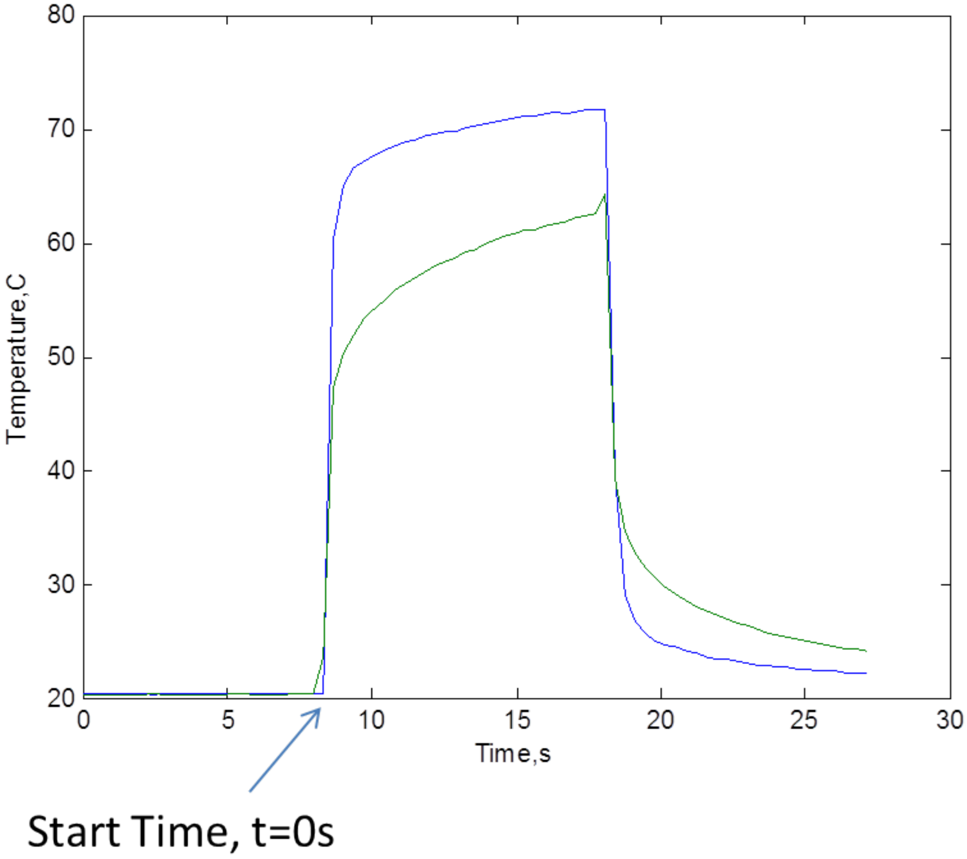

Start Time, t=0s

Figure 4.3: Step decrease in mainstream temperature.

### 4.3.4 Liquid Crystal Calibration

The purpose of liquid crystal thermography is to equate a color reflected off the TLC layer to a temperature. A thermocouple is placed on the surface with the liquid crystal coating to measure wall temperature over time. Care is taken so that the bead of the thermocouple is on the surface and not bent upwards into the mainstream. From the video, the thermocouple can be clearly viewed, as pointed out by the red arrow in Fig. 4.4. A small group of pixels are selected next to the thermocouple bead to relate color and wall temperature. The camera records data in terms of RGB (red, green, and blue) in values of 0-255. If R=0, G=0, and

B=255; then the pixel is blue. If R=255, G=0, and B=0; the pixel is red. Mixtures of RGB values produced different colors and shades. The RGB values are converted to HSV (Hue, Saturation, and Value). Both systems describe the perception of color, but in different ways. HSV is described in more detail in the following section. The HSV method allows a direct correlation between hue and temperature to be developed over a range of temperatures. Another advantage of hue to temperature calibration, is that a full range of colors may be used in the calculation of h, making the solution more robust to random uncertainty.

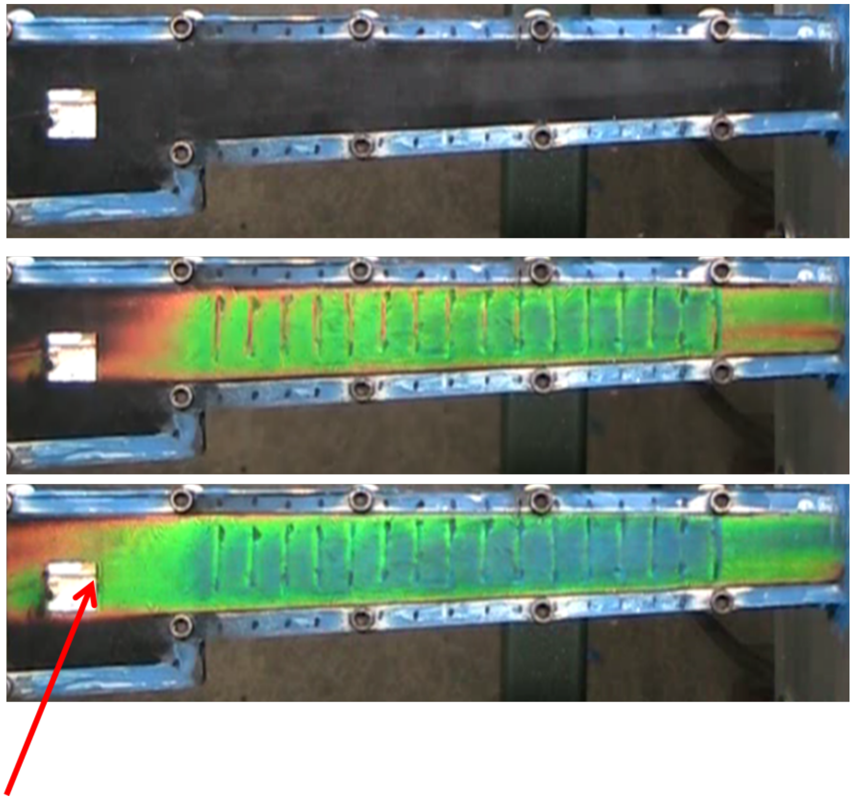

Figure 4.4: Location of wall temperature thermocouple and color progression during a test.

After synchronizing the thermocouple and video data, Fig. 4.5 shows the wall temperature and hue curves. The calibration region starts when the hue changes from red (hue=0.05) to green (hue=0.3). The resulting curve is shown in Fig. 4.5. The curve fit equation relates hue to temperature and, therefore, is applied to all pixels and all frames of the video. This

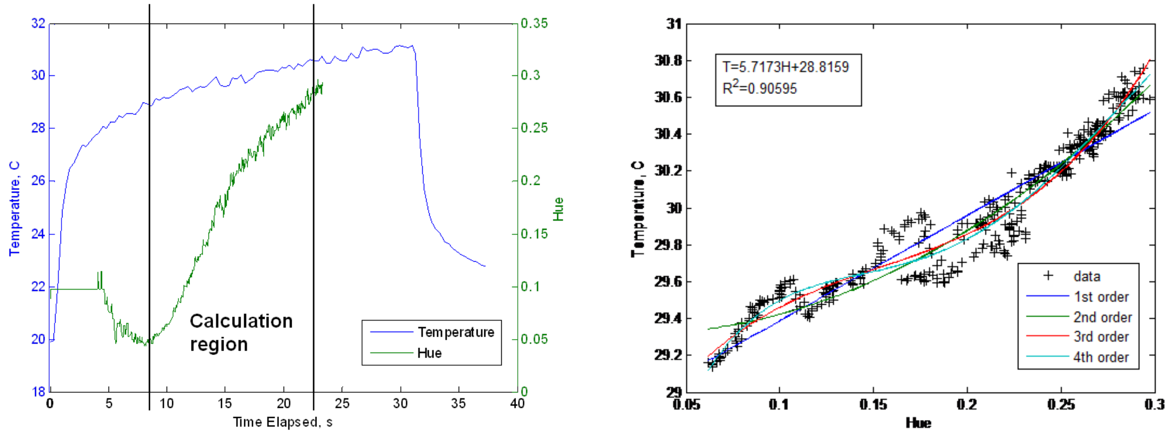

(a) Temperature and hue coupling.

(b) Calibration

Figure 4.5: Coupling of the wall temperature and the hue of the liquid crystal. Hue values of 0.05 is red and 0.3 is green.

builds a temperature history for each pixel which can be used in Eqn. (4.5).

The location for calibration is chosen carefully. If the thermocouple is placed in a region of high heat transfer, thus rapid color change, some issues arise. The thermal diffusivity of the liquid crystal, black backing, acrylic wall, and thermocouple bead are different. If heated too quickly, all the materials heat up at a different pace, throwing off the calibration. When steadily heated, the true temperatures of the materials increase (or decrease) in temperature more uniformly, giving a truer calibration of hue and temperature.

### 4.3.5 Hue Saturation and Value

Both CCD (charge coupled device) and CMOS (complimentary metal oxide semiconductor) chips are used in digital video cameras to convert light into digital signals. Light passes through red, green, and blue filters before hitting a photocell, which then converts photons into electrons and then into a voltage. Digital cameras save this voltage information in terms of how much red, green, and blue is present in the light at a particular pixel. Hue, Saturation, and Value (HSV) is another means of light classification. The HSV model is a cylindrical coordinate system, where Hue is the angular dimension describing pure color with red at $0^o$, green at $120^o$ and blue at $240^o$; saturation is the amount of white added to a pure color, and value describes the color as neutral, achromatic, or gray colors, as shown in Fig. 4.6. The reason for this conversion is to describe the color in one parameter, hue. One main issue arises after being converted to HSV. The liquid crystal is initially black, changes color from red to blue, then returns to black. In the HSV model, as Value approaches 0, the image appears black, as shown in Fig. 4.6. The issue that arises with this model is that any value of Hue can be assigned if the color is close to black because the Value is so low. This causes random jumping in the Hue value when plotted over time, as shown in Fig. 4.7. Figure 4.7 shows the hue history of a single pixel for each frame of the video. Initially, the image is black, shown by the large variation in Hue assignment. When the color change occurs, the hue changes in a smooth, predictable manner. A filter must be added to the code to prevent the random jumping into the data reduction, as false data points are added into the h calculation. This point will be explored in the *Data Reduction Procedure* section.

## 4.4 Data Reduction Procedure

Both the video of the liquid crystal color change and bulk and wall temperature thermocouple recordings are imported into the data reduction software, after the experiment is complete. The following section outlines the steps in the data reductions process: preprocessing, processing, and post-processing. Also, issues that arise in the data reduction procedure are discussed and solutions are explored.

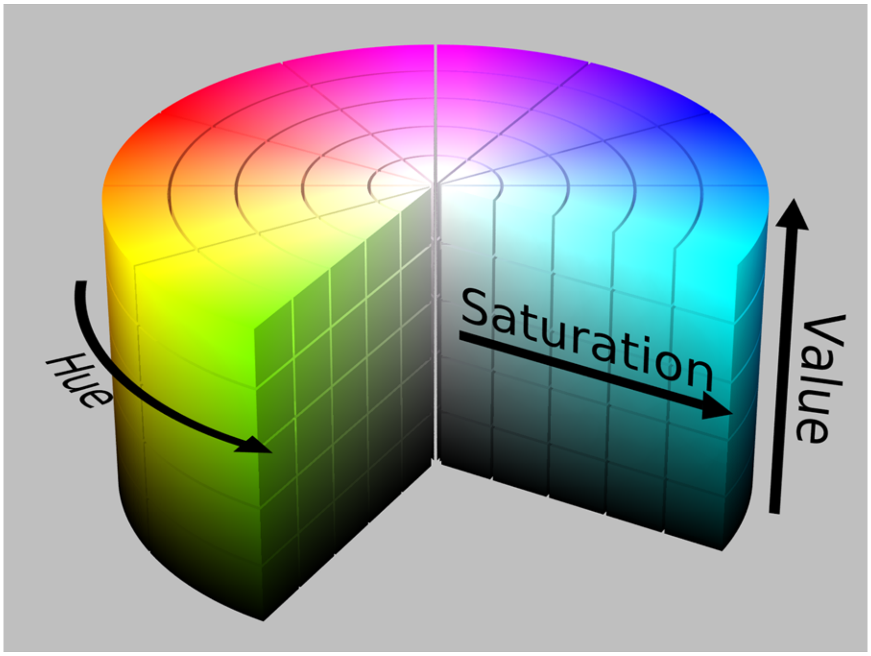

Figure 4.6: Hue, Saturation, and Value color classification system.

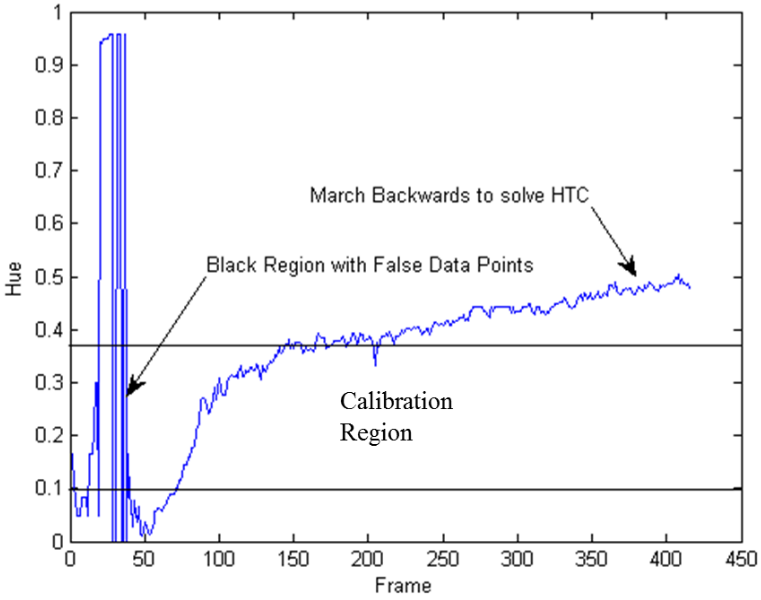

Figure 4.7: Hue history of a single pixel. The color is initially black, then steadily changes color from red to blue.

### 4.4.1 Preprocessing

The video is trimmed spatially and temporally. The video frames are trimmed to when the step input of hot (or cold) fluid is introduced. For each test, an audible or visual que is created to indicate when the temperature step occurs in the video (if the camera system is untethered, such as in the rotating rig). When the video is trimmed, this que becomes time, t=0 s. For the rotating rig, when the camera is spinning at speeds in excess of 500 rpm, audio ques can be heard over the rush of air over the microphone. A visual que is given instead. A light is placed inside the rig which is connected to a National Instruments relay module (single pole single throw). When the test is initiated, both the solenoid valves and light signals are switched. The instant the coolant is allowed to enter the test section, the light is turned off. The camera is able to see the light turn off, indicating the beginning of the test.

The video is trimmed spatially and rotated accordingly so that only the region of interest is left. Trimming reduces extraneous pixels that would otherwise be used in the h calculations, reducing the overall time to solution. The thermocouple data is cut so that the first time step is when the hot/cold fluid is introduced into the test section, which then becomes time, t=0 s. A sample temperature response with start time of the test noted is given in Fig. 4.3.

### 4.4.2 Processing

With matching of hue surface temperature, a temperature history for each pixel is created. This history is read into a FORTRAN solver program along with the bulk fluid temperature history (or histories if interpolating). The program solves pixel by pixel. A bisection method is used to calculate the heat transfer coefficient at each individual pixel. This iterative method creates three arbitrary guesses of h. These guesses are plugged into a modified form of Eqn.(4.5)

$$T_{w,est} = (T_m - T_i)\left(1 - exp\left(\frac{h^2 \alpha t}{k_w^2}\right)\left[erfc\left(\frac{h\sqrt{\alpha t}}{k_w}\right)\right]\right) + T_i \tag{4.6}$$

where $T_{w,est}$ is the estimated wall temperature based on the the bulk fluid temperature, time, and the guessed value of h. This value is compared to the measured wall temperature from the hue to wall temperature calibration

$$Err = abs\left(T(0,t) - T_{w,est}\right) \tag{4.7}$$

where Err is the error between the guessed value and actual wall temperatures. The heat transfer coefficient, h, can be solved in each moment of time for a series of wall and mainstream temperatures. The three initial broad guesses of h generate three Err values. When a minimum value of Err is found in a broad sense, an iterative process refines the h guesses until a minimum Err is reached. The final reported solution is the final minimum value.

As noted earlier in Hue, Saturation, and Value; when the liquid crystals appear black, the resulting hue value jumps around. These jumps can land within the calibration region, contaminating the calculation with false temperature values. Figure 4.7 illustrates this by plotting the hue history of a single pixel over time. The pixel is originally black, up until the $50^{th}$ frame. The hue jumps to the extremes, but also lands within the calibration region. Once the color begins to change, hue follows a steady curve from red to blue.

Some ways around the black contamination is available. One is to work backwards. As shown in Fig. 4.7, as the video progresses, the color change is on a predictable curve. If the mainstream temperature is set to induce a steady color change, but does not allow the liquid crystals to re-enter the black region, then working backwards is possible. Calculations follow this predictable curve backwards, but just before experiencing the black region at the beginning of the video. Calculations at the pixel cease just before the black region, thus eliminating the contamination.

In some instances, the color change progresses through the entire band in some areas, but in others the color change is much slower. This results in some locations returning to black, while others are still changing color. So by simply working backwards, some areas may be contaminated. One alternative is to cut the video up into segments and assign different ending times (so that working backwards may be adequate). However, there is still loss of data, as parabolic temperature profiles are common. This means color progression in the center of a channel is still quicker than near the edges. Using the method of cutting the video work with minimal loss of data becomes very tedious when presented with complex heat transfer distributions. The other alternative is to make a robust data reduction program that examines the entire hue history of all the pixels and uniquely sets start and end calculation conditions, instead of fixed start and end conditions for all pixels.

#### 4.4.2.1 Robust Analysis Procedure

A robust program individually examines each pixel and its hue history and decides where to begin and where to terminate calculations. The result of including the black contamination in the calculations is shown in Fig. 4.8. The color at high heat transfer locations will go black, change color, then back to black. The results are skewed at these regions, resulting in loss of data.

To fix this issue, the hue history of each pixel is examined, as shown in Fig. 4.9. When examining Fig. 4.9, the black regions have a lot of variance compared to the relatively smooth

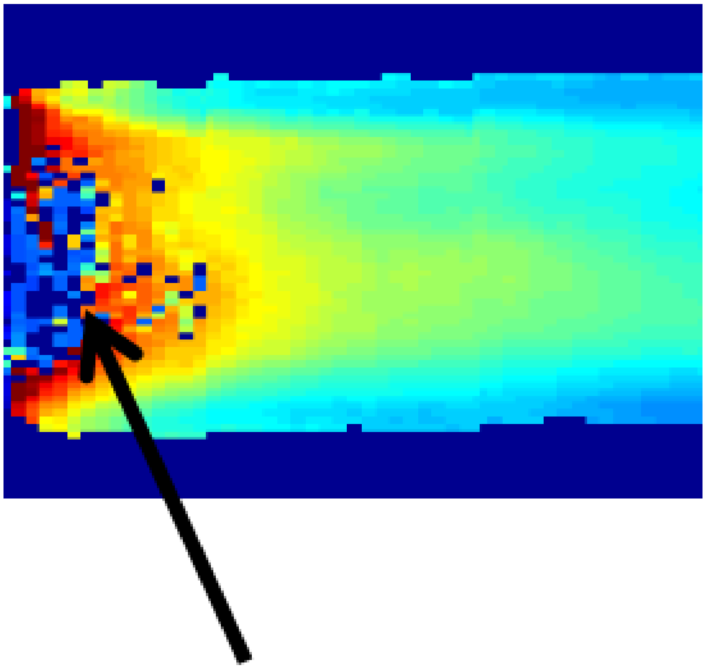

Figure 4.8: Result of allowing false temperature readings due to black contamination in the heat transfer coefficient calculation.

change in hue during color change. For each time step, the variance of hue of the current time step is compared to previous and upcoming time steps. When this is performed, Fig. 4.9 is the result. The variance is lowest during the color change (from about frame number 150-500). The start and end conditions for calculations are based on these results, thus filtering out the black contamination.

Some instances where the variance tracking filter does not catch all of the contamination. To add a second level of filtering, the FORTRAN code calculates a solution at each time step. If there is a lot of variation in the results, outliers can be left out. This is performed by averaging the raw results and calculating the standard deviation. All results that are outside three standard deviations of the average is excluded from the second round of averaging. A sample wall history over time is given in Fig. 4.10 (left). This shows the addition of black contamination in the wall temperature history. This impacts the results as shown in Fig. 4.10

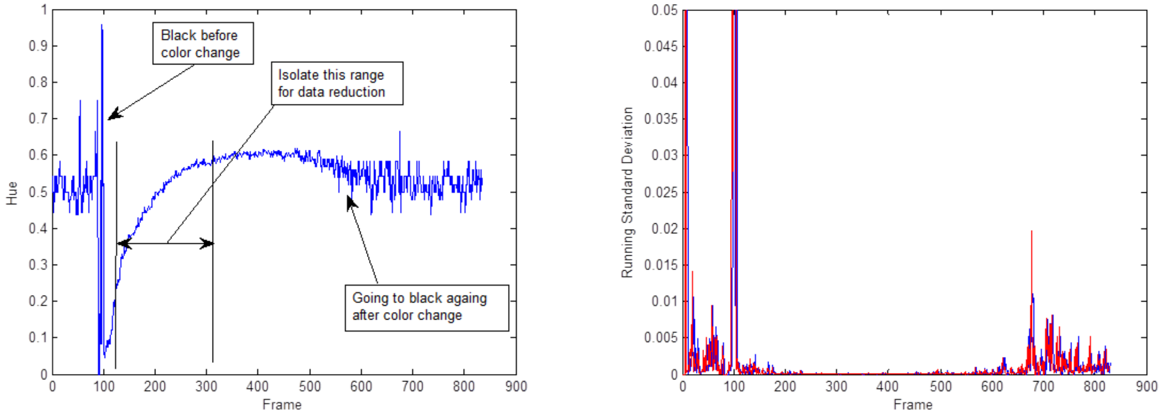

(a) Hue history of single pixel.

(b) Hue variance for each pixel.

Figure 4.9: Hue history and hue variance example for a single pixel.

(right). The outlying calculation is left out of the final result.

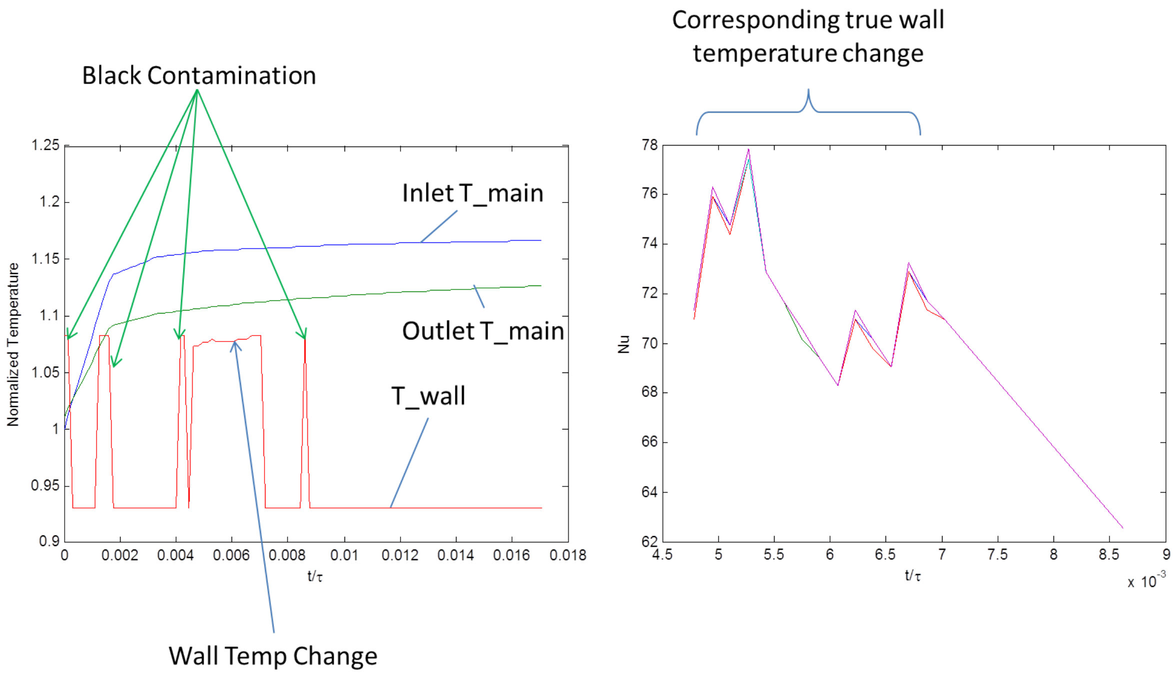

Figure 4.10: Mainstream and Wall temperature histories with black contamination.

### 4.4.3 Post Processing

Every pixel in the region of interest of the video is converted from a temperature history to heat transfer coefficient, h. Results are read in for each pixel to a MATLAB$^{TM}$ program, which displays the detailed results as shown in Fig. 4.11. Additions to the codes can be made to calculate average, mean, max/min values.

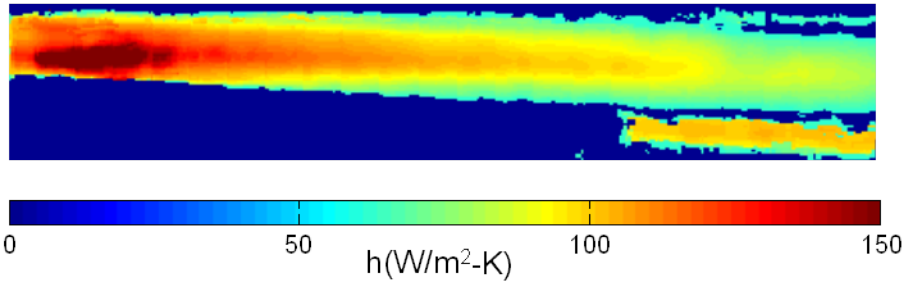

Figure 4.11: Final result of the data reduction procedure. This is a sample result of a diverging cooling channel.

The following section discusses how uncertainty in h values are calculated.

## 4.5 Uncertainty

To quantify the amount of uncertainty in the final h calculation, all sources of uncertainty must be identified and understood: T(0,t), $T_i$, $T_m$, $\alpha$, $k_w$, and t. There are many sources of uncertainty in the test setup and some sources may be difficult to quantify. The following section methodically identifies all sources of uncertainty and how they combine to determine the overall uncertainty in the h calculation.

### 4.5.1 Instrument Uncertainties

From Eqn. (4.5), $T_i$, $T_m$, and t are all directly measured. $T_i$ and $T_m$, are both directly measured using type k thermocouples. An Omega Instruments OMB-564 USB power/data transfer data acquisition (DAQ) system is used to record temperatures during the test. According to the specifications manual, the uncertainty in the thermocouple readings is ±1.2°C. The physical properties of $\alpha$ and $k_w$ are for the solid body. The temperature of the body ranges from $T_i$ to some final surface temperature. Because of the range in temperatures inside the solid, average values are used. Typically, low-conduction solids are used for transient tests. Typical materials used are clear acrylics. Thermal properties of the materials vary with temperature, therefore their uncertainty it tied to he uncertainty of the temperature measurements.

### 4.5.2 Calibration Uncertainties

T(0,t) is the surface temperature. This temperature is determined by relating the liquid crystal hue reflected to temperature from a thermocouple placed on the surface. There are several potential sources of uncertainty: instrument uncertainty from the thermocouple, instrument uncertainty of the camera for determining RGB (red, green, blue) values, uncertainty from time matching hue and temperature, uncertainty due to liquid crystal and black backing thermal conductivities. Like $T_i$ and $T_m$, the surface temperature has an instrument uncertainty of ±1.2°C. The camera records RGB values at each pixel. RGB values are integers in steps from 0 to 255. Published uncertainty in the value of RGB cannot be found for the specific camera used, so zero-order uncertainty is used (as explained in Figliola et al. [43]), therefore, uncertainty is approximately ±1/2 the resolution. RGB are integers, so they cannot be given in terms of fractions, so an uncertainty of ±1 is used. The time step for the thermocouple and the frame rate of the camera also have a degree of instrument uncertainty. Again, the zero-order uncertainty principle is assigned to these values. The time step the of the data acquisition is 0.25 s, therefore the uncertainty is 0.125 s. The camera takes a frame approximately every 0.03 s, to the uncertainty is 0.015 s. The purpose of calibration is to match the change in hue and change in temperature of the surface over time. To estimate the uncertainty due to time matching, the temperature time step is set to a minimum/maximum when the camera time is set to a maximum/minimum.

## 4.6 Overall Uncertainty and Design of Liquid Crystal Experiments

When designing and analysing transient liquid crystal experiments, uncertainty is an important concept to keep in mind. Liquid crystals may be created to change color in temperature ranges from -40 to 200 °F. Choosing a temperature range of liquid crystals is very important to not only reduce the uncertainty in h, but to capture as much detail in the region of interest as possible. To understand the limitations in a general sense, it is convenient to non-dimensionalize Eqn. (4.5)

$$\begin{aligned} t^* &= \frac{t}{\tau} && (4.8) \\ \tau &= \frac{D^2}{\alpha} && (4.9) \\ h &= \frac{Nu * k_f}{D} && (4.10) \\ T_w^* &= \frac{T(0,t)}{T_i} && (4.11) \\ T_m^* &= \frac{T_m}{T_i} && (4.12) \\ exp(Nu^2(\frac{k_f}{k_w})^2 t^*) erfc(Nu(\frac{k_f}{k_w})t^*) &= 1 - \frac{T_w^* - 1}{T_m^* - 1} && (4.13) \end{aligned}$$

where t is time, D is the hydraulic diameter of the channel, $k_f$ is thermal conductivity of the fluid, $k_w$ is the thermal conductivity of the solid plate, T(0,t) is the wall temperature, $T_m$ is the mainstream temperature, $T_i$ is the initial temperature. The left-hand-side of Eqn.(4.13) is plotted against the right-hand-side to generate a curve.

Figure 4.12 shows an asymptotic curve. In a liquid crystal experiment, the wall and mainstream temperatures are measured, as well as the time at which the color change occurs. With these pieces of information, Nu is solved. As the wall temperature approaches the mainstream temperature, $(1 - \frac{T_w^* - 1}{T_m^* - 1})$ approaches zero. Due to the asymptotic nature of the solution, as $(1 - \frac{T_w^* - 1}{T_m^* - 1})$ approaches zero, $(Nu(k_f/k_w)t*^{1/2})$ approaches infinity. This becomes a large issue when uncertainty in the temperature and time is taken into consideration. This point is illustrated in Fig. 4.13. For the same level of measurement uncertainty, the uncertainty in the Nu solution increases significantly.

As stated before, the liquid crystals are manufactured to change color in different temperature ranges. It is common to test multiple Re conditions for the same setup. It is also common to investigate turbulence enhancers such as ribs, dimples, pin fins to increase the heat transfer.

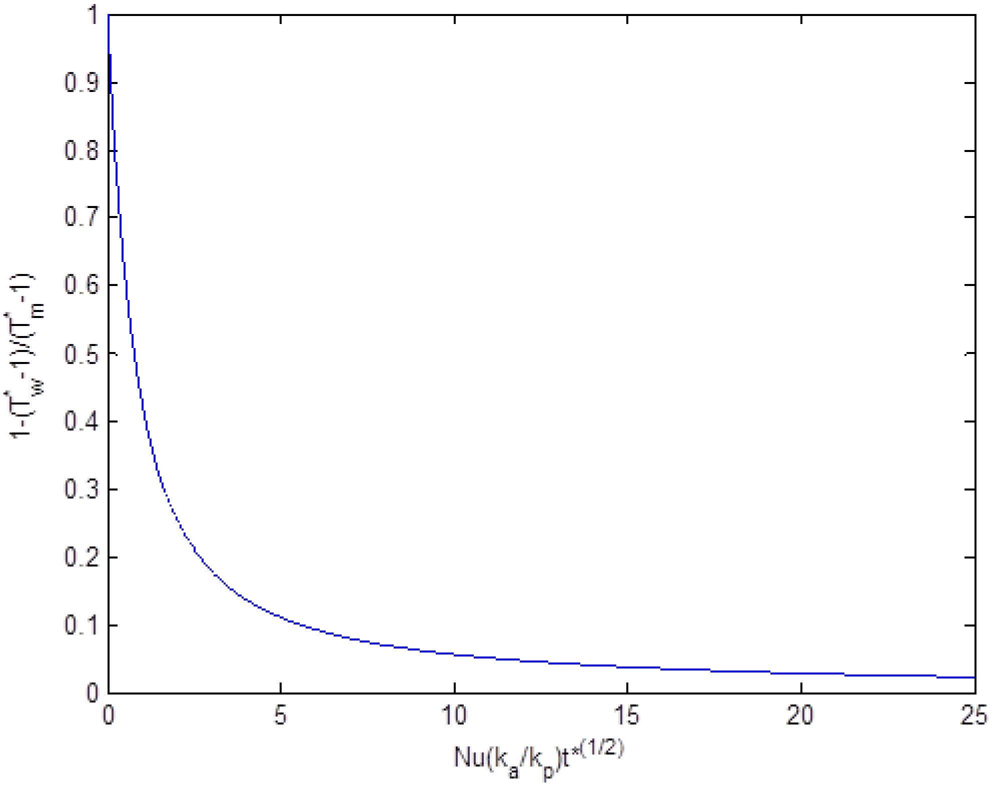

Figure 4.12: Non-dimensionalized curve representing solutions for Eqn.(4.13)

.

With varying Re and turbulence enhancers, the user will experience a wide range of heat transfer distributions. There are regions of slow color change and regions of fast color change. When the user has access to an arc welder or DC power supply to generate heat in a mesh screen, there is much flexibility in the mainstream temperature control. Therefore, the mainstream temperature should be set so that the slowest color change region has a corresponding mainstream temperature high enough to avoid the asymptote from Fig. 4.13. In many test conditions, a considerable drop in mainstream temperature is encountered from the inlet to the outlet. Because the slow color change region is accommodated by a reasonably high mainstream temperature (which would occur at the exit of the channel), the inlet temperature will be considerably higher. This causes an even more rapid color

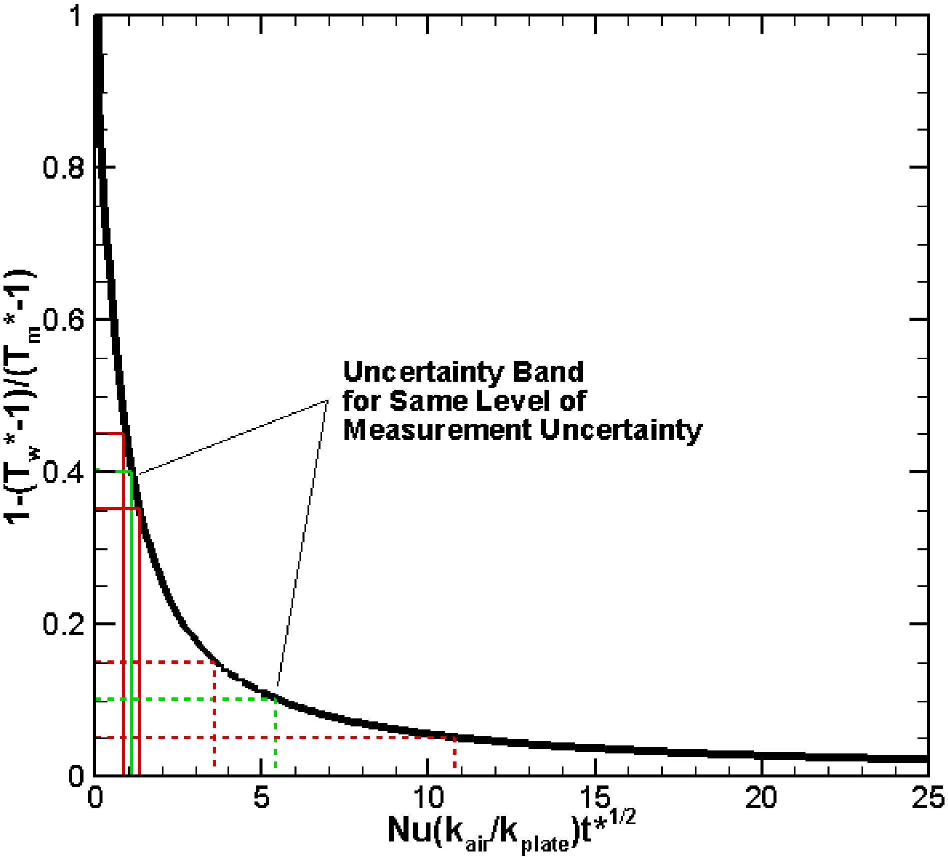

Figure 4.13: For same level of measurement uncertainty, when $T_w$ approaches $T_m$ measurement uncertainties become amplified.

change. The color change in the high heat transfer region can occur when the mainstream temperature is ramping up. During this ramp up, the mainstream and wall temperatures may be very close in value, therefore the $1 - \frac{T_w^*-1}{T_m^*-1}$ parameter may be approaching zero, causing high uncertainty in the solution.

### 4.6.1 Selection of TLC Temperature Band

Before beginning a series of experiments, the Re range is known. This allows the user to guess the average heat transfer coefficient inside the channel (assuming internal cooling). This is possible by estimating Nu by the Dittus-Boelter equation.

$$Nu_{db} = 0.023Re^{(4/5)}Pr^{(1/3)} \tag{4.14}$$

where Re and Pr are known before the test is performed. $T_w^*$ can be plotted over time for different steps of $T_m^*$. The maximum time of the test is restricted to $t = 0.1\frac{B^2}{\alpha}$, where B is the thickness of the plate the liquid crystals are applied, as described in Yan and Owen [44]. The minimum time of the test is bounded by the step change of the mainstream temperature. In heated tests, mesh heaters may be used. The ramp up time will vary depending on the mass flow rate of gas flowing through the mesh and the power setting of the DC power supply. Knowledge of the heater response is recommended at expected flow and power settings, so Nu calculations during ramp up time are excluded. Limitations of the data acquisition system must be known beforehand. This tells the user what measurement uncertainty is associated with the thermocouples (used for both mainstream temperature acquisition and wall temperature for calibration).

# 5. Rotating 2-Pass Channel With and Without Ribs

The present study models a simple square channel, similar to the channels in Fig. 1.2, with both radially outward and inward flow, as seen in Fig. 5.1. A camera is mounted to the test section to take measurements, so the entire section cannot be measured all at once. The focus of this study is at the 180$^o$ turn and the channels immediately leading up to the turn. Figure 5.1 is an idealized model, but will provide great insight into the nature of flow in an actual turbine blade.

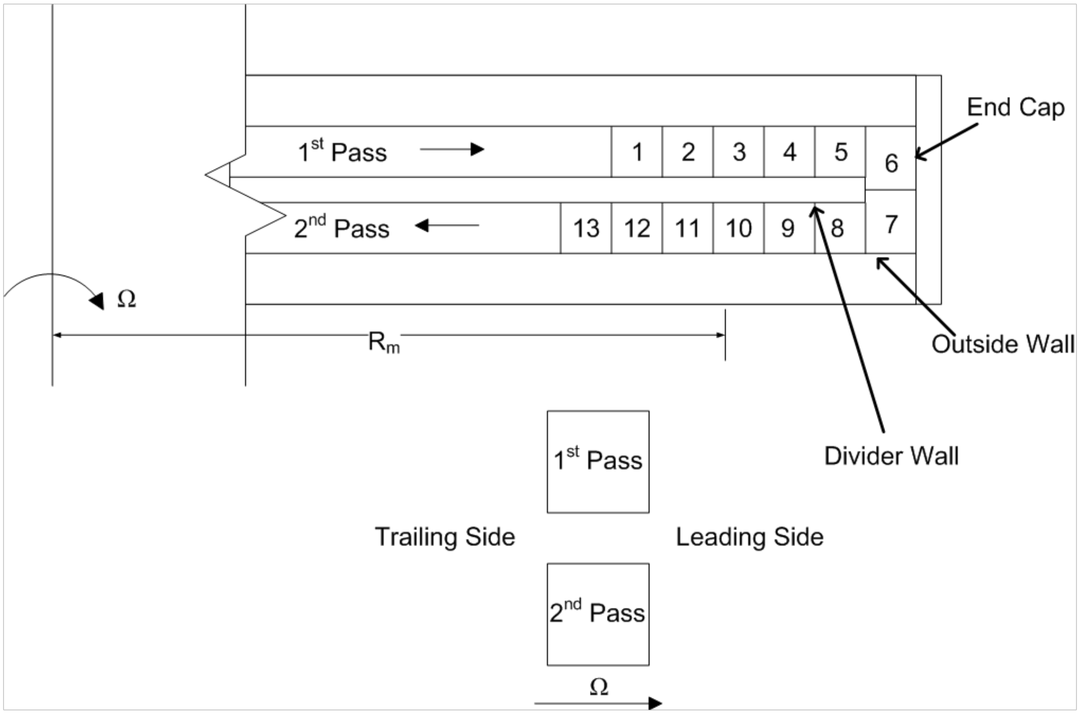

Figure 5.1: (Top) Schematic of the test section. First-pass is where the coolant air enters. Second-pass is where the coolant air exits. Average heat transfer calculations are made in regions 1-12. Region 13 is for calibration. (Bottom) View of the test section looking down the channels.

This study examines the effect of rotation on smooth walls, 90$^o$ ribbed walls, and W-shaped ribbed walls for a two-pass channel. A transient liquid crystal technique is used to measure local heat transfer. All cases are performed at Re=16,000. Rotational cases are performed at 250 rpm, to reach a Rotation number (Ro) of 0.08. The inlet density ratio, $\Delta\rho/\rho$, is set to 0.1.

Three parameters are controlled in the study: $\Delta\rho/\rho$, Re, and Ro. The Reynolds number was controlled by setting the mass flow rate of air with a regulator and orifice meter. The Rotation number is set by selecting a motor speed on the motor frequency controller. When the thermocouple at the vent reaches approximately $-30°$C, the coolant air temperature drops and remains at $-10°$C (air is initially at 20°C) during testing. A sample response of the inlet, turn, and outlet mainstream temperatures are shown in Fig. 5.2.

## 5.1 Test Section

The test section is a two pass channel with a 2.54 cm (1 in) square cross section, 180° bend, and 1.27 cm (0.5 in) divider wall with a .635 cm (0.25 in) rounded edge at the 180° turn. The divider wall has a length of 18.5D$_h$. The gap at the end of the divider wall and end cap (180° turn) is 1.5D$_h$ from the center of the rounded edge of the divider wall. The material used for the test section is a clear acrylic, which is a preferred material because of the optical access due to a low refraction index, which allows a clear view of the color change in the liquid crystals. The thermal conductivity of acrylic is low, which is ideal for transient modelling, as 2-D conduction is minimized for the time it takes to perform the test. Figure 5.3 shows the test sections used for the experiments. The air enters the top channel and exits the bottom. The air travels through bored channels within the aluminum hub before entering the test section. The channel changes from a 2.54 cm (1 in) diameter circular cross section to a 2.54 x 2.54 cm square cross section. The air travels 10.5D$_h$ down the smooth test section

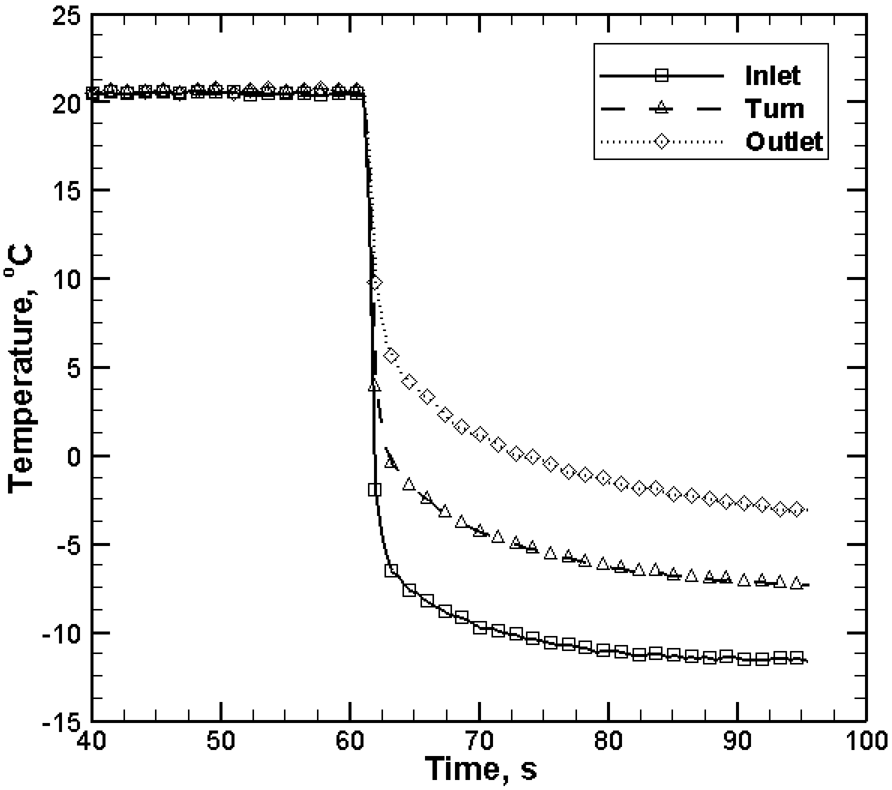

Figure 5.2: Typical temperature step response of the air in the test section when the flow direction is switched.

before encountering the first rib (for ribbed cases). The 90° ribs are 0.3175 cm (1/8th in) square cross section and span the width of the channel. Ribs are only placed on the leading and trailing sides of the channel and are in-line. The pitch of the ribs is 2.54 cm (1 in), giving the ribs a pitch-to-rib height ratio (P/e)=8. A side view of the 90° ribs are shown in Fig. 5.4, which shows the rib pitch, rib height, and channel height. The W-shaped ribs are 0.3175 cm (1/8th in) square cross section and also span the width of the channel. W-shaped ribs are oriented at 45° as shown in Fig. 5.5. Figure 5.5 also shows the direction at which the coolant passes over the W-shaped rib. W-shaped ribs are also only placed on the leading and trailing sides of the channel and in-line. The pitch-to-rib height ratio (P/e)=8. Each pass has a length of 5D that is recorded in the video. This is illustrated in Fig. 5.1, as the first pass consists of regions 1-5 (each region is 1D in length) and the second pass consists of regions 8-12. Region 13 in Fig. 5.1 is used for calibration. The ratio of the mean rotating arm radius-to-channel hydraulic diameter ratio ($R_m/D$)=22. $R_m$, as shown in Fig. 5.1, is the distance from the center of the recorded area of the test section to the center of rotation. The blockage ratio remained constant, $e/D$=0.125. Figure 5.1 defines the divider wall, outside wall, and end cap which is referred to in the results.

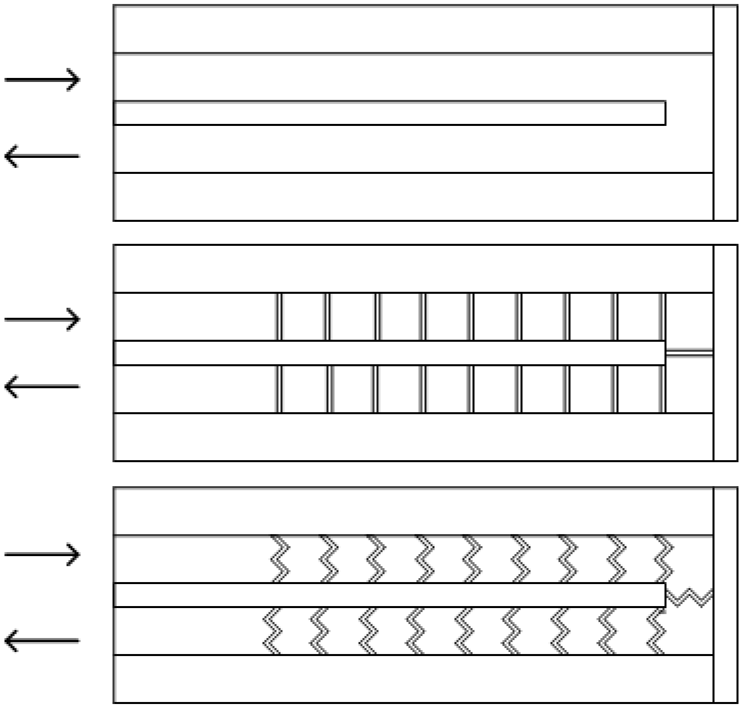

Figure 5.3: The test sections used for two-pass channel study. Schematic of the test section with: (top) smooth wall, (middle) 90° ribbed walls, and (bottom) w-shaped ribbed walls.

## 5.2 Results and Discussion

Three channel configurations are tested in rotation: smooth walls, 90° ribbed walls, and W-shape ribbed walls. Each configuration ran at Re=16,000 and two rotational speeds: 0

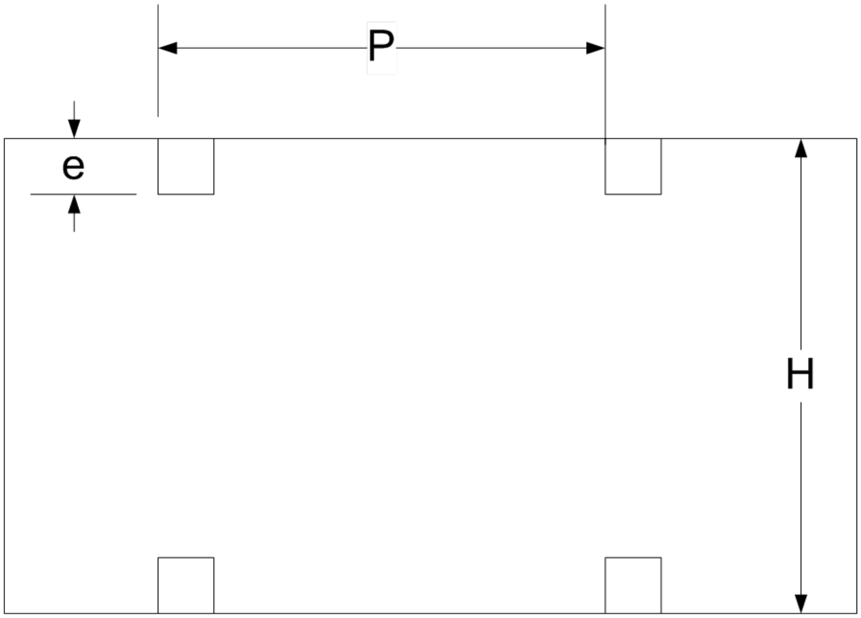

Figure 5.4: Side view of the ribs. 'P' is the pitch of the ribs, 'e' is the height of the ribs, and 'H' is the height of the channel.

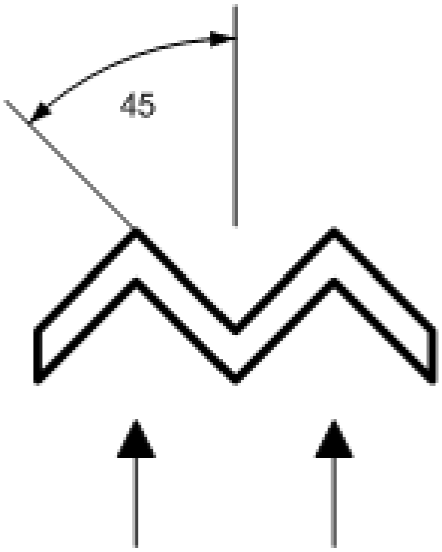

Figure 5.5: W-shaped rib geometry. The flow path is from bottom to top of the rib.

and 250 rpm. For this flow rate, Ro=0.08. The inlet $\Delta\rho/\rho$=0.1. For all rotational cases, the buoyancy parameter is 0.014. As the buoyancy parameter is much less than 1, the Coriolis force is the main influence on the flow pattern and heat transfer distribution. The following separately discusses the results for each rib case during rotation. For each rib case, the trailing side and leading side results are compared to the stationary case. The ribbed cases are compared to the smooth walls separately for the stationary, trailing, and leading cases. Average heat transfer values are calculated in the regions labelled 1-12 in Fig. 5.1. The heat transfer over the ribs are not calculated, therefore not included in the average calculations.

### 5.2.1 Effects of Rotation on Smooth Walls

Figure 5.6 shows detailed results of the smooth wall test section for stationary and rotating cases. The heat transfer ratio of the first-pass, stationary case is expected to be approximately one. The channel length is more than $10D$ leading up to the beginning of the frame, indicated the flow is or is close to being fully developed. The normalization parameter is the Dittus-Boelter equation which estimates the average wall heat transfer in a straight, smooth channel. Although the present study uses square channels, the results are similar to the empirical results. Figure 5.7 is the area average heat transfer along the length of the channel, showing that the stationary test results of the first-pass correlates well with the fully developed expectation. High heat transfer in the 180° turn is developed due to the geometry of the turn. The sharp corners do not guide the flow, so the incoming flow from the first pass impinges on the end cap. The turbulence created in the turn creates high heat transfer at the beginning of the second-pass then begins to decrease and stabilize as the flow develops. These results are consistent with the previous study by Ekkad and Han [45] for stationary channels and similar geometry.

#### 5.2.1.1 First-Pass

The trailing side shows an overall augmentation in heat transfer. This is in direct agreement to results from Wagner et al. [4]. As stated in [4, 5, 7] the Coriolis force is normal and into the trailing side, which thins the boundary layer and augments heat transfer. The leading side heat transfer decreases compared to the stationary case. The boundary layer thickness of the leading side increases, reducing heat transfer. The Coriolis force acts normal and away from the leading side. The heat transfer suddenly increases at the end of the first-pass leading side. Liou et al. [46] found the same phenomena for similar flow conditions, Re=10,000 and Ro=0.10. Although a different mainstream temperatures are for [46], the buoyancy parameter is low enough for buoyant flows to have minimal effects on the overall flow pattern. The average heat transfer from [46] shows approximately the same magnitude increase at the end of the first-pass leading side.

#### 5.2.1.2 Turn Region

The turn region experiences high heat transfer for both the trailing and leading sides due to flow impingement on the end cap, however noticeably less than on the stationary case. There is a low heat transfer region in the center of the turn, as shown by Fig. 5.8. This may be caused by flow impingement on the end wall, decreasing the velocity. With decreased velocity, rotational forces dominate. The slower flow begins to swirl with the increased presence of rotation. Incoming coolant from the first-pass impacts the swirling flow in the turn, decreasing the velocity and imparting swirl on the incoming flow. The coolant rotates in opposite directions causing a slight reduction in heat transfer where they meet. As the reduction happens in the center of the turn for the leading side, the trailing side shows high heat transfer in the middle of the channel, with slight reduction on the edges. This heat transfer distribution is also evident in [46].

#### 5.2.1.3 Second-Pass

The flow hugs the edge of the divider on the trailing side, as opposed to the leading side where the flow hugs the outside wall. [46] observes this distribution, as well. Higher heat transfer is present in the stationary case compared to both the trailing and leading sides. The turn causes the flow entering the second pass to become more complex. Complex flow coupled with the Coriolis force causes the flow to impinge on the outside and dividing walls, more than the trailing and leading walls themselves. With flow development after the turn, the trailing side heat transfer steadily decreases below that of the stationary case, as expected predicted. The Coriolis force acts away from the trailing side and into to the leading side. As the flow develops, the leading side heat transfer drops below that of the stationary case, but appears to settle at a value above the stationary case at higher x/D. Turn effects dominate heat transfer in the second pass, before the boundary layers begins to stabilize. Table 5.1 shows the average percent change in heat transfer between the rotating and stationary cases for the two passes.

Table 5.1: Summary of the average percent changes in heat transfer due to rotation for each rib type.

| | | Smooth Wall | 90° | W-shape Ribs |
|---|---|---|---|---|
| Trailing Side | $1^{st}$ Pass | 25 | 5 | 0 |
| | $2^{nd}$ Pass | -16 | -4 | -7 |
| Leading Side | $1^{st}$ Pass | -16 | -11 | -1 |
| | $2^{nd}$ Pass | -8 | 20 | 15 |

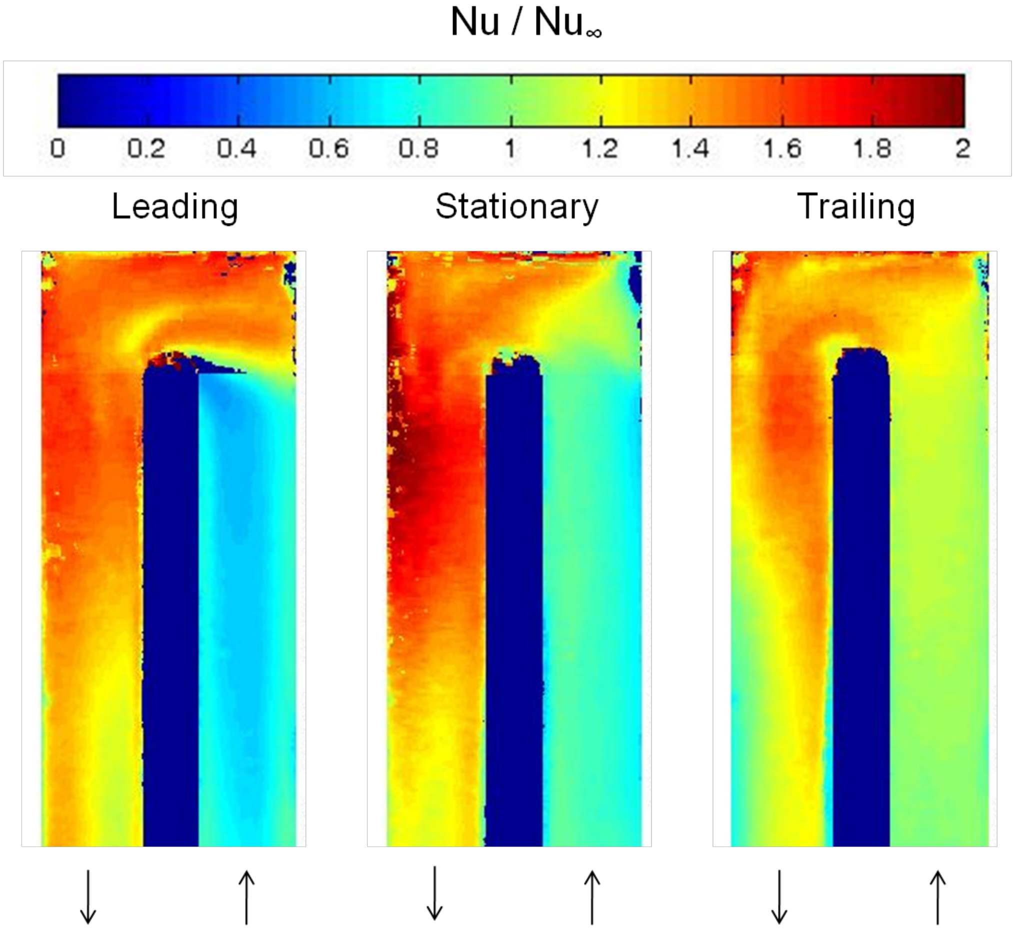

Figure 5.6: Leading side, stationary, and trailing side heat transfer results due to rotation.

### 5.2.2 Effects of Rotation on 90° Ribbed Walls

Figure 5.9 shows the detailed results of the 90° ribbed wall case. The distribution of the stationary case shows similar distributions compared to [45, 47]. Figure 5.10 shows area average results along the length of the channel. The magnitude of the results are similar to [45, 47], however slightly lower.

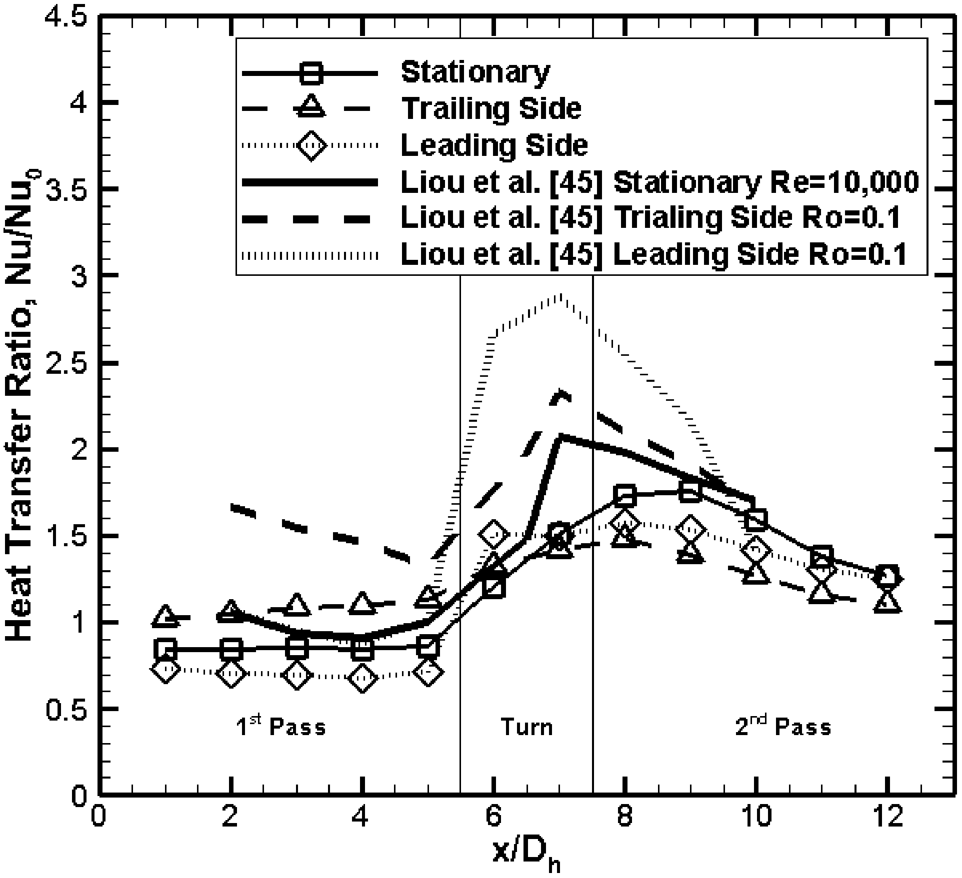

Figure 5.7: Area average heat transfer along the flow path of the smooth wall channel.

#### 5.2.2.1 First-Pass

Heat transfer increases are present on the trailing side and decreases in the leading side, as expected. Opposed to the smooth wall results, the 90° rib results show a steady increase in heat transfer leading up to the turn region. Rising heat transfer could be due to the turn effects encroaching in the first-pass. Parsons et al. [7] also observes this behavior. The augmentation in heat transfer for the 90° ribs is similar invprevious studies, however, slightly lower. This could be due to the different pitch-to-height ratio for the ribs. The present study

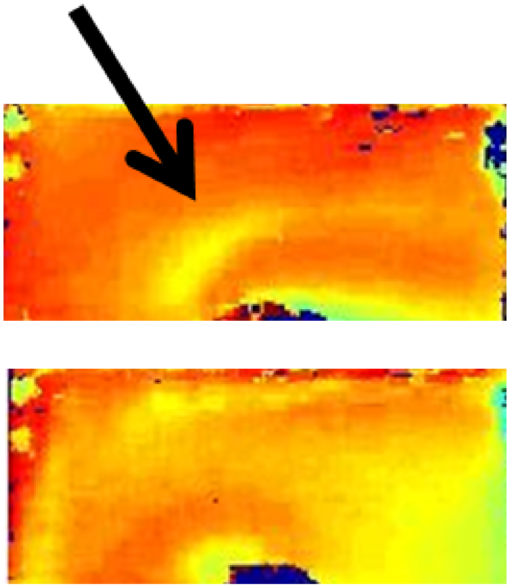

Figure 5.8: Turn effects in smooth channel.

uses a pitch-to-height ratio of 8, while [4, 5, 7, 6, 45, 47] use a ratio of 10. The maximum changes in heat transfer are lower than the smooth wall cases.

#### 5.2.2.2 Turn Region

The entrance region of the turn shows the same heat transfer distribution for the stationary and trailing side cases. However, the trailing side has higher heat transfer. This may be due to the Coriolis force reducing the reattachment length after the rib. The leading side distribution is more spread out and does not show a low heat transfer band between high heat transfer regions as the stationary and trailing side cases do. The Coriolis force may act to increase the reattachment length after the rib. The latter half of the turn, region 7 in Fig. 5.1, shows the same distribution for all cases. Because the flow is in the same direction as the rotational velocity, the Coriolis force is reduced. The rib in the center acts to break down the asymmetrical flow just before the rib.

#### 5.2.2.3 Second-Pass

The trailing side heat transfer decreases while the leading side increases. The presence of the ribs break down the turn effects in the second-pass quickly as evidenced by the higher heat transfer on the leading side than the stationary case. Also, the trailing side heat transfer quickly drops off and stabilizes quicker than the smooth wall case. Immediately after the turn, a high heat transfer region off-center of the first rib is formed. The off-center region disappears by the next rib, as the heat transfer is evenly distributed along the rib, showing the effectiveness of the 90° ribs to break down uneven flow patterns. The ribs increase overall heat transfer compared to the smooth wall case. The second-pass has higher heat transfer than the first-pass because of the complex flow that exits the turn, resulting in increased mixing across the channel width. Local turbulence is enhanced and can create higher heat transfer than seen in the fully developed region of the first-pass. Although ribs help to redistribute the flow in the channel width, high turbulence is still present from the turn.

Table 5.1 shows the average percent change in heat transfer between the rotating and stationary cases for the two passes. Increases in heat transfer due to rotation are lower than the smooth wall cases. The ribs significantly increase the heat transfer in the channel, and are less sensitive to rotational effects. The flow is less sensitive due to the secondary flows generated by the tripping effect of the ribs. Secondary flows travel in directions different than that of the bulk movement, so the Coriolis force acts in different directions other than purely on the trailing (or leading) side, reducing the overall effect of the Coriolis force.

### 5.2.3 Effect of Rotation on W-shape Ribbed Walls

The heat transfer ratio distribution for the W-shaped ribs shows a dramatic increase compared to both the smooth wall and 90° rib channels. Detailed results are in Fig. 5.11. Area

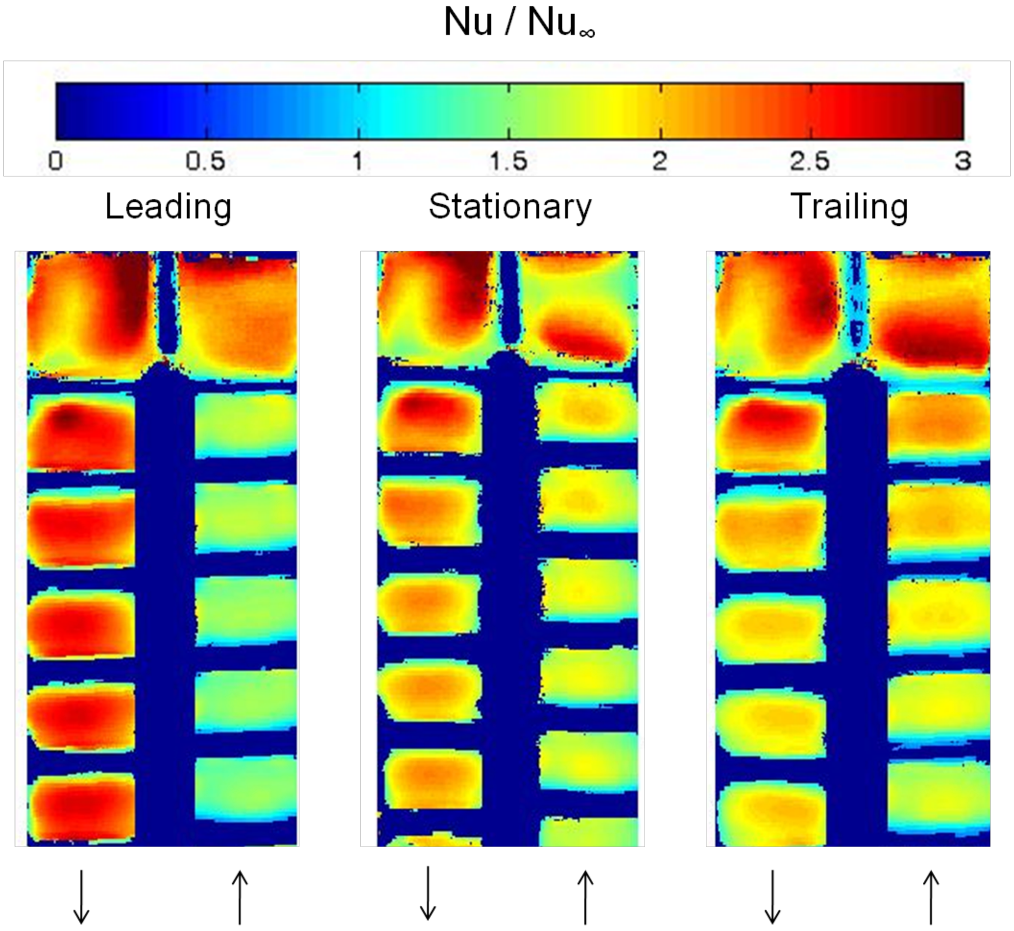

Figure 5.9: Leading side, stationary, and trailing side heat transfer results due to rotation for 90° ribbed channel.

average heat transfer along the flow path is in Fig. 5.12. In this case, the W is oriented so the two tips point in the flow direction, as shown in Fig. 5.13.

#### 5.2.3.1 First-Pass

Between the stationary, trailing, and leading side cases; the first-pass results do not vary by a great amount. The flow separates at the two tips of the W, causing the flow to swirl in four areas as shown in Fig. 5.13. In the center of the channel, vortices 2 and 3 combine at the interface B to impinge on the wall, increasing heat transfer. Between vortices 1 and

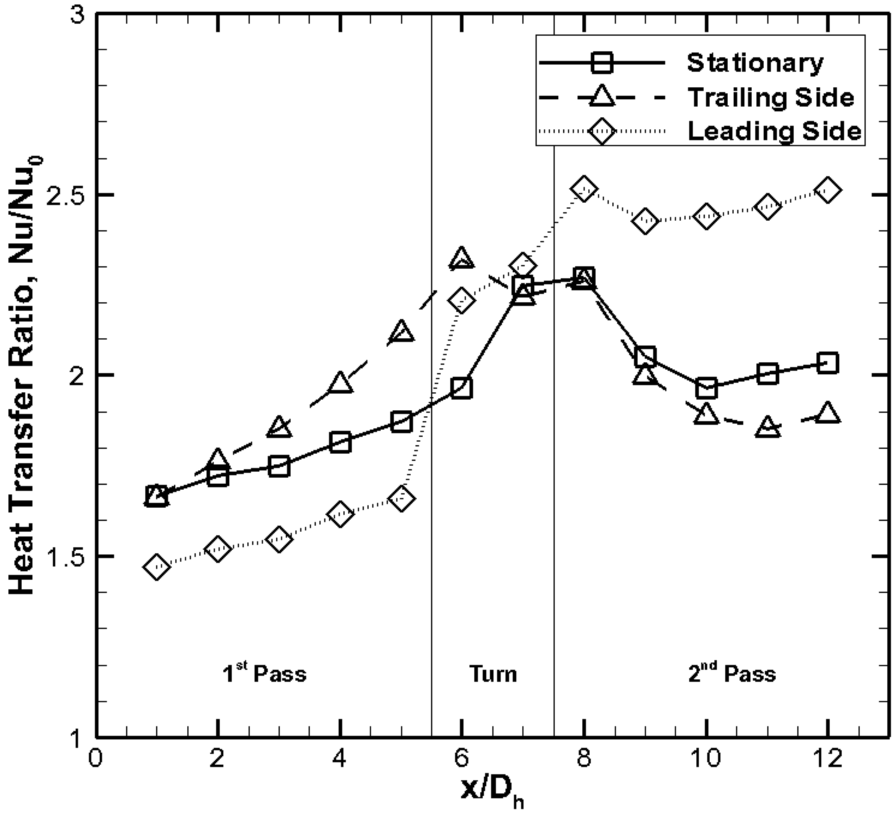

Figure 5.10: Area average heat transfer along the flow path of the 90° ribbed channel.

2 and vortices 3 and 4, the interfaces A and C experience and uplifting flow moving away from the wall, creating a drop in high heat transfer compared to interface B. Similar studies by Wright et al. [12], the stationary case heat transfer ratio increases from approximately 3.0 to 4.25 in 5D. The present study shows a similar increase just before the turn, as shown in Fig. 5.12. The present study shows increases from approximately 3.0 to 3.5. Differences to previous studies are due to test section geometry, orientation with respect to rotation, and differences in rib geometry. Wright et al. [12] used a rectangular geometry (AR=4:1), the section is oriented 45° from the direction of rotation, and flow is radially outward. It appears the presence of the turn significantly contributes to the differences in results.

#### 5.2.3.2 Turn Region

A significant jump in heat transfer is present when the coolant enters the turn. As in the 90° ribs, the trends for the stationary and trailing side cases are similar, while the leading side distribution is more spread out. Unlike the 90° ribs, the average heat transfer on the leading side is higher than the other cases before and after the center rib. The increase seen in the leading side is attributed to the swirling secondary flows shed from the ribs, which are less affected by the Coriolis force. The second half of the turn, region 7 in Fig. 5.1, shows similar distributions between all cases, with the exception of the leading side, shows higher heat transfer. Similar trends are present in the 90° rib case, but the increase is more prevalent for the W-shaped rib.

#### 5.2.3.3 Second-Pass

The highest overall heat transfer is experienced after the first rib of the second-pass for all cases. The flow hugs the outside wall of the second-pass for all cases. Opposed to the smooth wall case, the flow hugs different walls coming out of the turn for the trailing and leading sides. The flow from the turn favors the outside tip of the W instead of both. The W-shaped rib requires more x/D to evenly correct the flow than the turn with 90° ribs. After the initial jump in heat transfer after the turn, there is a sharp decrease at the next rib, accompanying a steady rise. Uneven flow distribution causes the drop, which creates high heat transfer near the outside wall but low heat transfer near the divider wall. The average heat transfer across the width of the channel is low due to the flow imbalance. As the flow develops, the entire width experiences high heat transfer.

Table 5.1 shows the average percent change in heat transfer between the rotating and stationary cases for the two passes. The W-shaped ribs are effective for increasing the overall heat transfer and reducing the influence of the Coriolis force. The secondary swirling flows generated by the W-shaped ribs are 3-D, whereas, the 90° ribs create secondary flows only in a 2-D plane parallel to the direction of flow. The W-shaped ribs are not as effective in evenly distributing the flow after the turn region. Table 5.1 summarizes the maximum changes in heat transfer for each rib type at each rotational case.

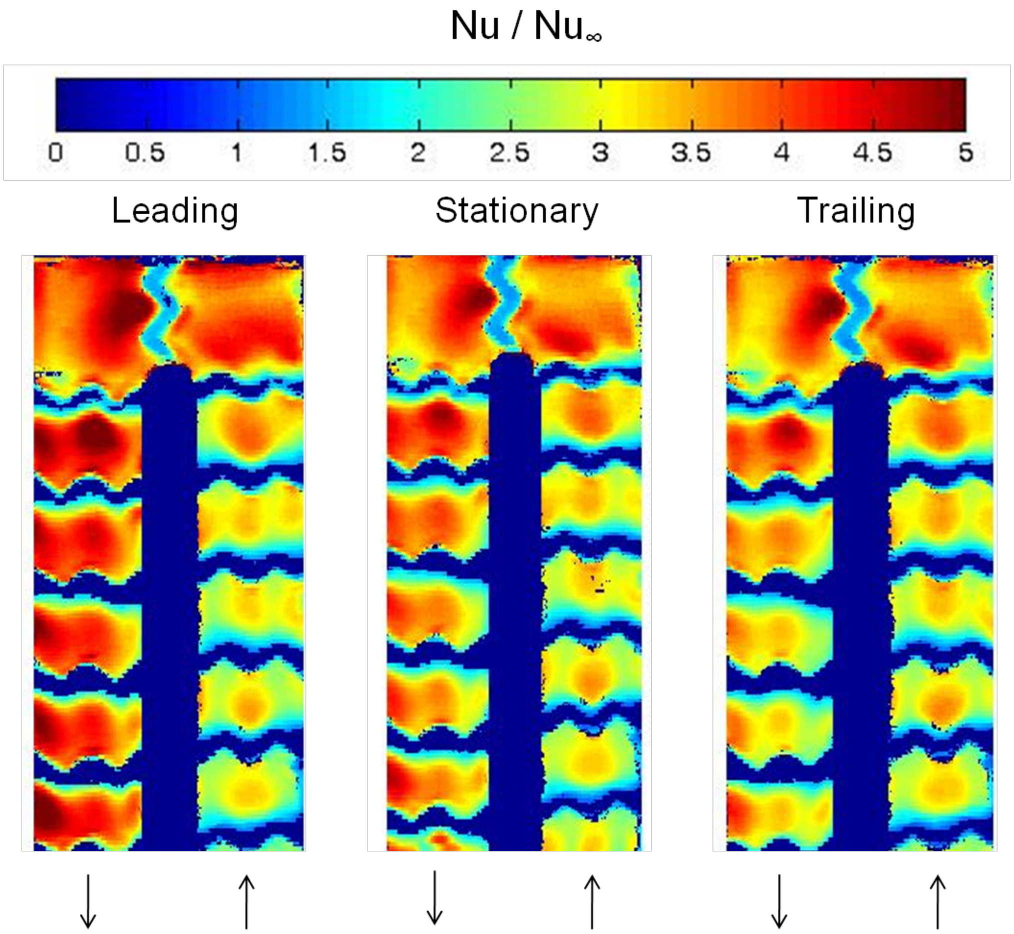

Figure 5.11: Leading side, stationary, and trailing side heat transfer results due to rotation for W-shaped rib channel.

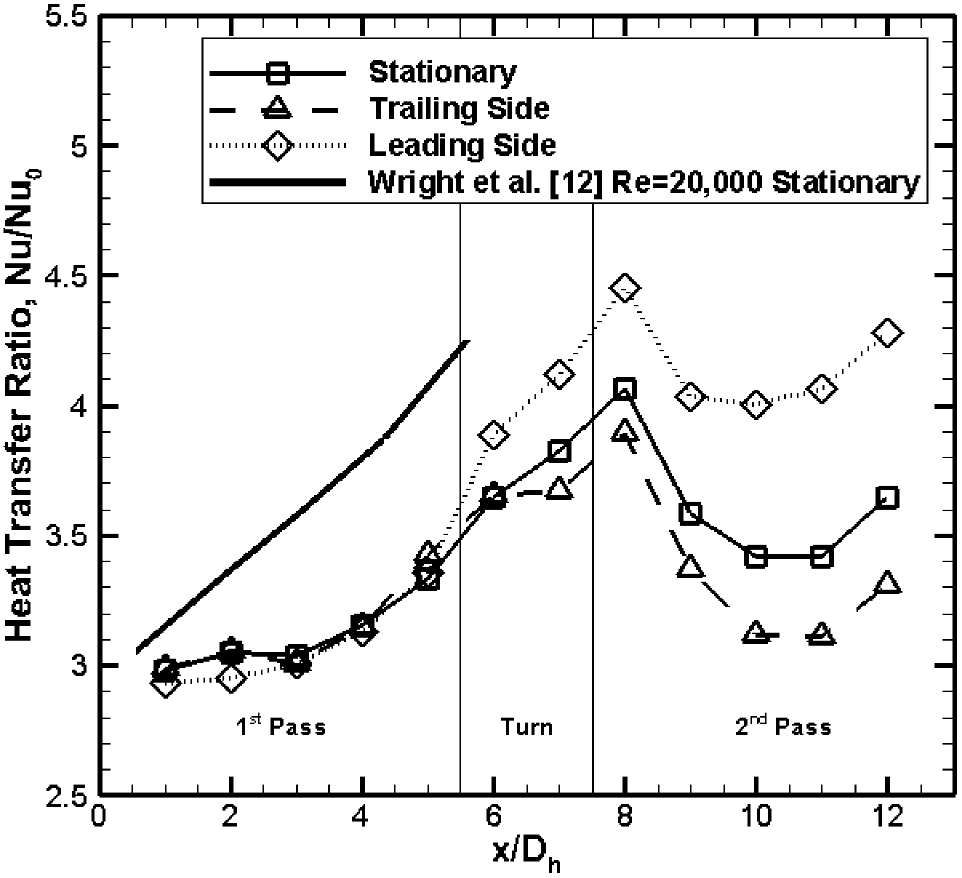

Figure 5.12: Area average heat transfer along the flow path of the W-shaped ribbed channel.

### 5.2.4 Comparison of Rib Types

#### 5.2.4.1 Stationary

Figure 5.14a shows a comparison between the smooth wall, 90° rib, and W-shaped rib wall. Table 5.2 shows the average percent change between the 90° and W-shaped ribs with the smooth wall. The first-pass experiences the largest increase in heat transfer for both rib types. The W-shaped rib is approximately 2.5 times as effective for increasing the heat

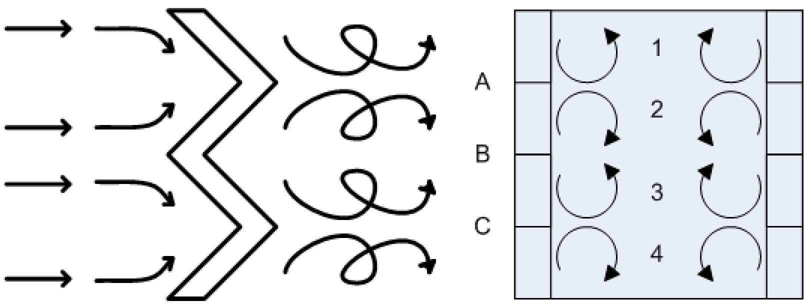

Figure 5.13: (left) How the coolant passes over the W-shaped rib and how the flow is shed. (right) shows a cross sectional view of the vortices generated due to W-shaped ribs. Vortices are labeled 1, 2, 3, and 4. This helps explain the heat transfer pattern seen at locations A, B, and C.

transfer in the first-pass and 4.4 times for the second-pass. Higher increases are present in the first-pass, as turn effects are not as prevalent as in the second-pass. The turn effects create highly turbulent flow for all cases. Because the turn creates more turbulence, the effectiveness of the ribs are slightly reduced.

#### 5.2.4.2 Trailing Side

Figure 5.14b shows a comparison between the smooth wall, 90° rib, and W-shaped rib wall. Table 5.2 shows the average percent change between the 90° and W-shaped ribs with the smooth wall. The W-shaped rib is approximately 2.7 times as effective for increasing heat transfer in the first-pass and 3.0 times in the second-pass.

#### 5.2.4.3 Leading Side

Figure 5.14c shows a comparison between the smooth wall, 90° rib, and W-shaped rib wall. Table 5.2 shows the average percent change between the 90° and W-shaped ribs with the smooth wall. The W-shaped ribs are approximately 2.9 times as effective for increasing heat transfer compared to the 90° ribs in the first-pass and 2.6 times greater in the second-pass.

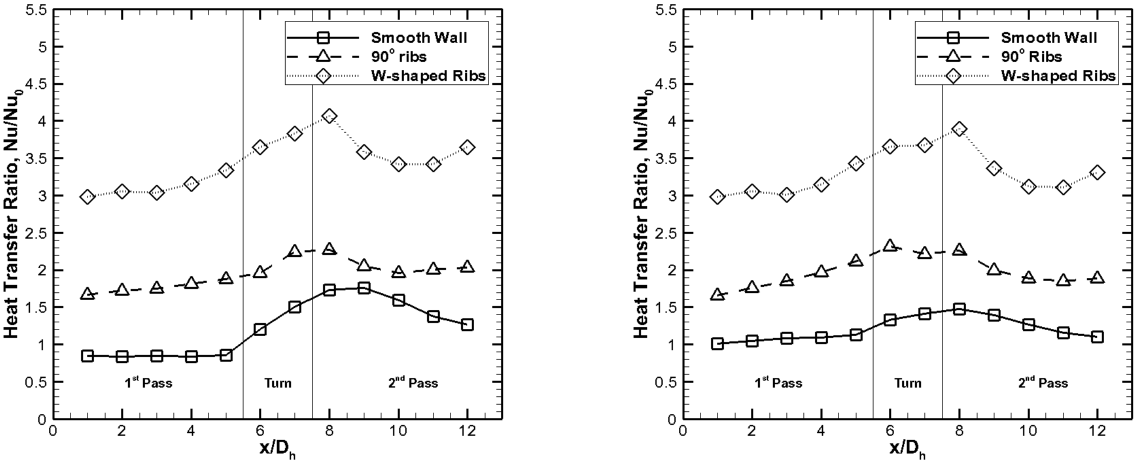

(a) Stationary comparison.

(b) Trailing side comparison.

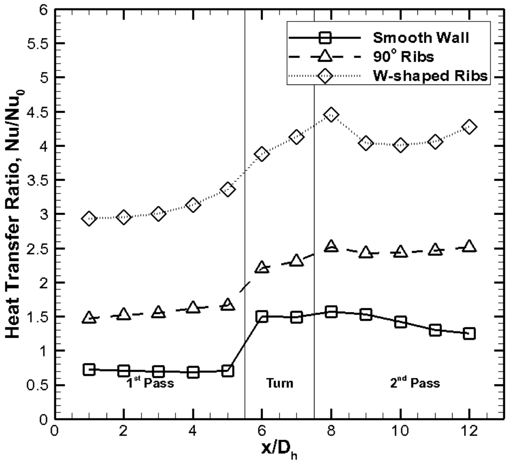

(c) Leading side comparison.

Figure 5.14: Stationary, trailing side, and leading side results comparison.

The leading side has the highest overall increase in heat transfer for both rib types and for both passes. The trailing side has the lowest overall increase in heat transfer for both rib types for only the first pass. The stationary case has the lowest overall increase for both rib types for only the second pass. The smooth, leading side, first-pass case experiences a sharp drop in heat transfer due to the Coriolis force. The addition of the ribs break down this effect and causes the largest gains in heat transfer. The smooth, trailing side, first-pass experiences an augmentation in heat transfer, however, the ribs break down the influence of the Coriolis force. There is still an increase in heat transfer with the ribs in place, but gains are not as high as seen in the leading side case. The stationary gains are between that of the leading and trailing side gains due to the ribs. The largest gains in the second-pass are on the leading side. Using the same argument in the first-pass, it is expected that the trailing side experiences the largest gains. However, the turn effects are significant in the second-pass, decreasing the effect of the Coriolis force compared to the first-pass. The gains in the stationary, trailing, and leading side second-pass heat transfer are similar compared to the large disparity in gains for the first-pass, due to the dominating presence of the turn effects.

Table 5.2: Summary of the average percent changes in heat transfer for each rib type compared to the smooth wall.

| | | Stationary | Trailing Side | Leading Side |
|---|---|---|---|---|
| $1^{st}$ Pass | 90° Ribs | 104 | 71 | 116 |
| | W Ribs | 260 | 190 | 325 |
| $2^{nd}$ Pass | 90° Ribs | 35 | 55 | 76 |
| | W Ribs | 138 | 164 | 197 |

### 5.2.5 Thermal-Hydraulic Performance

The W-shaped ribs produced the highest heat transfer results of the three cases studied. However, with the promotion of higher mixing, the pressure drop across the channel increases. The trade-off of increases heat transfer to pressure losses is calculated the thermal-hydraulic performance, Eqn. (1.6. Using a similar method as Wright et al. [12], the thermal-hydraulic performance is calculated as the ratio of the Nusselt number to the pressure drop. Pressure measurements are taken only when the test section is stationary, so it is approximated that the pressure drop during rotation does not deviate much from the stationary case. The pressure drop is measured from region 1 to region 12. Table 5.3 shows the thermal-hydraulic performance of the 90° and W-shaped ribs for the stationary and rotating cases. Despite the higher pressure loss of the W-shaped ribs, the gains in heat transfer are warranted.

Wright et al. [12] studied W-shaped ribs on a AR=4:1, radially outward, 45° oriented channel. The thermal-hydraulic performance was examined at increasing Re values. At Re=16,000, similar to the present study, the thermal-hydraulic performance was 1.701. This is similar to the results from Tab. 5.3 of the present study on W-shaped ribs.

Table 5.3: Average heat transfer ratio, pressure drop, pressure drop ratio, and thermal performance of the two rib types explored. Despite higher pressure losses, the thermal performance of the W-shaped ribs is higher than the $90^o$ ribs. The pressure drop across the smooth channel is 10.4 mm $H_2O$.

| | | $Nu/Nu_o$ | $\Delta p(mmH_2O)$ | $(\Delta p/\Delta p_o)^{(1/3)}$ | $\eta$ |
|---|---|---|---|---|---|
| $90^o$ | Stationary | 1.92 | 42.4 | 1.60 | 1.20 |
| | Trailing | 2.01 | 42.4 | 1.60 | 1.26 |
| | Leading | 1.95 | 42.4 | 1.60 | 1.22 |
| W | Stationary | 3.39 | 70.5 | 1.89 | 1.79 |
| | Trailing | 3.28 | 70.5 | 1.89 | 1.73 |
| | Leading | 3.62 | 70.5 | 1.89 | 1.91 |

## 5.3 Conclusions

Detailed heat transfer distributions in a rotating channel were measured using a novel transient liquid crystal technique. The camera was mounted on the test section and images were captured with the cameras on-board memory. The data was measured with cold air and a room temperature test section rotating at a set speed. Smooth walls and 90° and W-shaped ribbed walls were studied for a two-pass square channel under stationary and rotating conditions. Of all cases studied, the smooth wall channel is most affected by the Coriolis force. This may be because the presence of ribs break down the developing flow, reducing the effect of the Coriolis force. The W-shaped ribs may be less affected by the Coriolis force than the 90° ribs because the W-shape imparts 3-D swirl to the flow, increasing the turbulence. The 90° ribs create secondary flows only in a 2-D plane parallel to the direction of the flow. As the Coriolis force is dependent on the flow direction, the swirl in the fluid may reduce the effect because the velocity has more components than just radially outward (or inward). The turn greatly affects the heat transfer in the second-pass for all cases. The presence of the ribs break down the influence of the turn in the second-pass compared to the smooth wall case. Of the rib types studied, the 90° ribs are most effective after the turn in redistributing the flow evenly across the width of the channel. This prevents a considerable dip in heat transfer, as seen in the W-shaped rib case. The W-shaped ribs produce a complex 3-D set of vortices which aid in mixing, increasing the heat transfer. However, this complex flow pattern leads to higher pressure losses. Even with the higher pressure losses, the gains in heat transfer warrant their use, as seen in the thermal-hydraulic performance calculation. At the rotation number studied in this present study, the effect of buoyancy was minimal. This is evident by the very low Buoyancy Parameter and by the similarity in results compared to [46, 47].

# 6. Radially Outwards at High Rotation Numbers

The present study focuses on the effects of high rotation numbers on the heat transfer distribution on the leading and trailing side walls, as these walls experience the greatest effects due to rotation (for rectangular channels with faces normal to the Coriolis force). Three rib types are examined under rotation: 90° are common simple ribs and W and M-shaped ribs are high performance ribs. Rotation is examined in developing flow conditions. Results are normalized to the stationary smooth wall. Commonly, the Dittus-Boelter equation is used for normalization, however, the equation only applies to fully developed flow (L/D > 10).

## 6.1 Test Section

The test section is a radially outward square channel. The channel height, H, is 7.62 cm (3 in) and the viewable length, L, is 15.24 cm (6 in). The mean rotating radius, $R_m$, is 60.96 cm (24 in). The material is made of a clear acrylic. Figure 6.1 shows the test section and the nomenclature used for the rib properties. P is the pitch, e is the rib height, and H is the channel height. The P/e ratio is held at 8. The e/H ratio (blockage ratio) was held at 0.125. In Fig. 6.1, the box with a dashed line shows where measurements taken. The measurement regions begins 5D from the entrance to the test section and has a length of 2D. The flow is developing because the region of interest is less than 10D from the entrance. As shown in Fig. 6.1, ribs at P/e=8 lead up to the viewable area. The cross-hatching in Fig. 6.1 are honeycomb laminators, with 0.635 cm diameter holes, which help break down inlet asymmetries. Two circular holes supply the coolant from the aluminum hub to the test section causing a sudden jet expansion. The holes are 2.54 cm in diameter and spaced 2.54 cm from the center of the channel. The 90°, W, and M-shaped ribs are used to roughen the leading and trailing sides. All ribs are directly opposed as shown in Fig. 6.1. The W and M-shaped ribs come in two types, 45° and 30°, as shown in Fig. 6.2. Figure 6.3 shows how W and M-shaped ribs are defined with respect to the direction of flow.

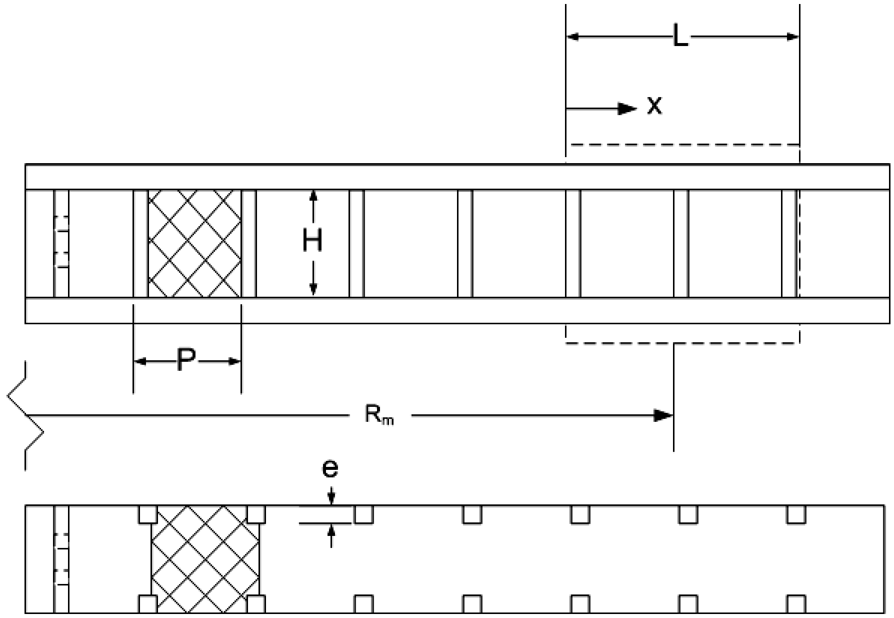

Figure 6.1: Test section used for large diameter study. This has a large cross-section to achieve high Rotation numbers at relatively low rotational speeds. The crosshatching indicates the honeycomb laminators to break down entrance asymmetries.

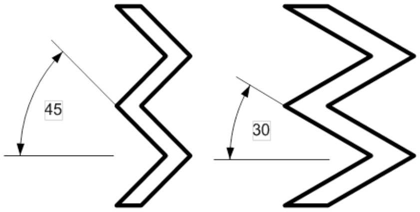

Figure 6.2: The two types of W/M shaped ribs used in the present study.

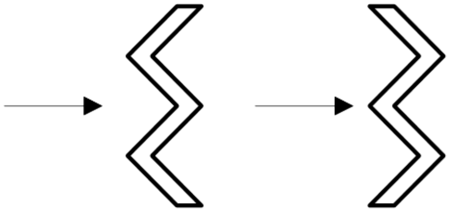

Figure 6.3: Definition of W/M shaped ribs. (Left) W-shaped ribs. (Right) M-shaped ribs.

## 6.2 Results and Discussion

Tests are run at an average Re=12,000 and at two rotational speeds causing Ro=0.3 and 0.5. Buoyancy is not of concern due to low BP and transient tests do not allow sufficient time to develop buoyancy (Liou et al. [46, 47]). The calculated BP=0.137, showing low buoyancy effects. The following results demonstrate the effects of the Coriolis force alone. For the ribbed cases, average results are taken before and after the center rib. Recirculating regions, indicated by exceptionally low heat transfer are not included in the average, as too few data points are present to generate a result.

### 6.2.1 Smooth Wall Baseline

The stationary smooth wall is used to normalize the ribbed wall results. Relative gains and losses are calculated for the various rib configurations during rotation. Ribbed cases are normalized to the spanwise average along the length of the smooth channel. Figure 6.4 shows the heat transfer distribution of the smooth, stationary baseline has relatively good symmetry along the length of the channel. The addition of the honeycomb laminators break down the expanding jets entering the test section. Fig. 6.5 (left) shows the spanwise average results used for normalization. Fig. 6.5 (right) shows the stationary results normalized to the Dittus-Boelter equation, illustrating the developing nature of the flow.

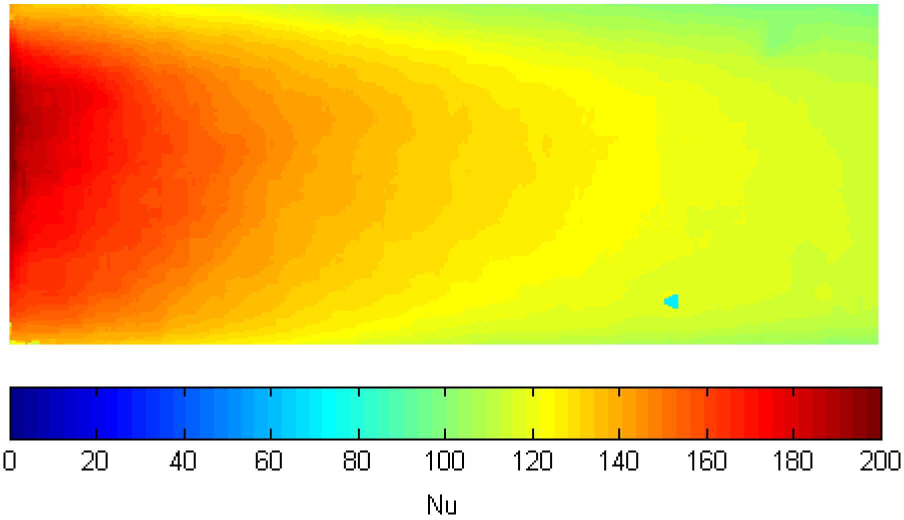

Figure 6.4: Heat transfer distribution for the smooth, stationary baseline case.

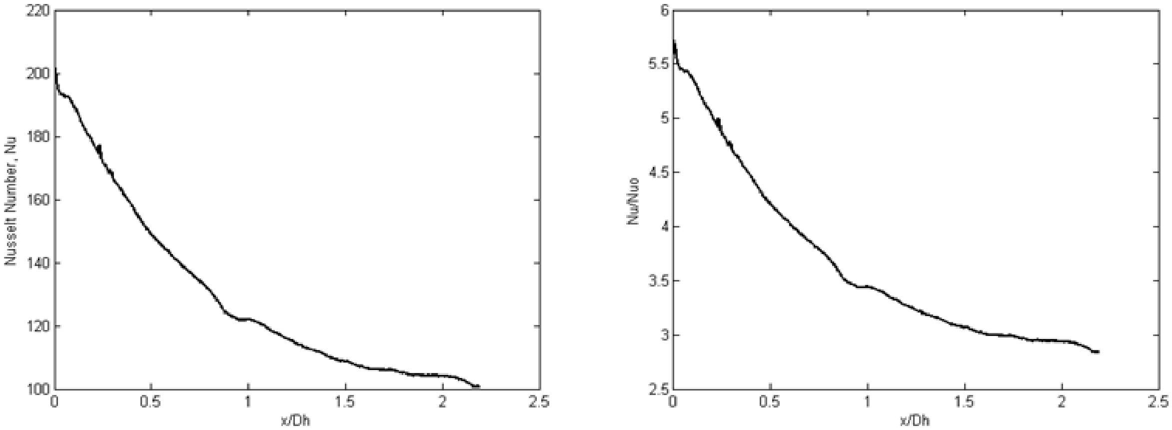

Figure 6.5: (Left) Spanwise Nusselt number average along the length of the channel. (Right) Spanwise Nusselt number average normalized to the Dittus-Boelter equation along the length of the channel.

### 6.2.2 90° Ribs

Figure 6.6a shows the results for the 90° rib configuration. Figure 6.7a shows the spanwise average distribution of heat transfer over the length. Stationary results show a relatively uniform distribution of heat transfer along the span of the channel. The enhancements are approximately 1.17 for the stationary case. In a fully developed condition, the addition of the 90° ribs can cause increases of over 2-3 times (Wagner et al. [4], Liou et al. [47], Parsons et al. [7], Taslim and Wadsworth [48]) compared to the smooth wall case.

The trailing side cases experience an overall increase in heat transfer, while the leading side shows an overall decrease. Due to the direction of the Coriolis force, this is expected for a radially outward channel. The Coriolis force is directed normally into the trailing side and normally away from the leading side. Thinning the boundary layer on the trailing side, creating higher shear, which increases mixing and subsequently increases heat transfer. The leading side experiences a thickening of the boundary layer, reducing shear and heat transfer. Table 6.1a shows the percent change in average heat transfer for the rotating cases compared to the stationary 90° rib case.

### 6.2.3 45° W-shaped Ribs

Figure 6.6b shows the results for the W-shaped 45° rib configuration. The heat transfer distribution is not even along the span of the channel. The incoming flow is split up due to the sharp points of the rib and creates 3-D swirling flow downstream. Figure 6.8 illustrates how the heat transfer distribution is created. The stationary case shows two regions of high heat transfer, which are approximately symmetric. The trailing side shows enhancements in heat transfer, while the leading side shows decreases. During rotation the two high heat transfer regions from the stationary case are present, but not symmetric. The trailing side shows the bottom high heat transfer region to be much larger than the top. The opposite is true on the leading side, where the top region is larger. The leading side does not show the same heat transfer distribution as the trailing and stationary cases, one high heat transfer region is present, not two. The heat transfer smooths out on the leading side, reducing the effectiveness of the ribs.

Recirculating regions are identified by low Nu. After the ribs, recirculating zones are present for all cases. The zones for the stationary and leading sides are much larger than the trailing sides. The Coriolis acceleration forces the boundary layer to reattach to the surface for the trailing side, reducing the size of the recirculation zone.

### 6.2.4 45° M-shaped Ribs

Figure 6.6c shows the results for the 45° M-shaped rib configuration. Figure 6.7c Swirling flow shed from the ribs creates the patterns shown in Fig. 6.8, which explains the three heat transfer region distribution. The trailing side shows enhancements in heat transfer, while the leading side shows decreases. For the trailing side, the three high heat transfer regions are present, but are not symmetric like in the stationary case. The lower part of the channel is more dominant, creating uneven heat transfer distribution. The three high heat transfer regions on the leading side are much less distinct, similar to the W-shaped configuration. The top portion of the leading side is dominated by the flow, as opposed to the bottom on the trailing side. For the leading side Ro=0.3, only two high heat transfer regions are present. At Ro=0.5, the distinct heat transfer regions are not present. The ribs do not appear to be aiding in heat transfer. Table 6.1 shows the relative gains and losses in heat transfer compared to the respective stationary case.

Similar to the 45° W-shaped ribs, the recirculation zones for the trailing side cases are much smaller than the stationary and leading side cases. The Coriolis force presses the flow back to the surface after the rib, reducing the reattachment length.

### 6.2.5 30° W-shaped Ribs

Figure 6.6d shows the results for the W-shaped 30° rib configuration. Figure 6.7d show the spanwise average plot. Similar to the W-shaped 45° ribs, two high heat transfer regions are present. The 30° ribs show slightly higher results compared to the 45° ribs. Like the 45° W-shaped ribs, swirling flow is shed. The angle is sharper for the 30° configuration, so the ribs guide the incoming flow more efficiently. The 45° ribs divert the flow at a greater angle, so more energy is taken out of the flow compared to the 30° angle. The remaining energy of the flow after the 30° angles translates to more intense swirling, causing the increased heat transfer at the surface between the ribs.

As with the 45° W-shaped ribs, the trailing side experiences increases in heat transfer, while the leading side experiences decreases. The differences between the leading side cases are minimal.

### 6.2.6 30° M-shaped Ribs

Figure 6.6e shows the results for the M-shaped 30° rib configuration. Figure 6.7e show the spanwise average results along the length. The sharper 30° angle induced higher heat transfer results for all cases, stationary and rotating. The sizes of the recirculation zones appear to be much smaller than the 45° M-shaped cases. This is especially true in the leading side cases. The 45° M-shaped ribs leading side cases show a crescent shape after the ribs of low heat transfer, showing a large recirculation zone. The leading side cases do not show this for

30° M-shaped ribs.

Results show a strong effect of the Coriolis force on the heat transfer distribution for both the leading and trailing sides. As the Coriolis force is increased, the trailing side results continue to increase, however, the leading side is reduced so much and no further. The Coriolis force cannot induce a flow reversal, it only drives the flow to zero.

### 6.2.7 Average Results

Figure 6.9 shows the average results for all cases with averages before (1) and after (2) the rib. All cases, rotating and stationary, show significant changes for both trailing side cases. However, following the initial drop in heat transfer for the leading side, there is little change between the two leading side cases. This is because the velocity gradient in the boundary layer is reduced, but does not induce a flow reversal. A limit is reached for a reduction in heat transfer on the leading side between Ro=0.3 and 0.5. The sharper 30° ribs generate slightly higher average heat transfer results than the 45° cases. All rib cases show similar lower limits for the leading side, while the trailing side maximum values have variation from rib to rib.

## 6.3 Conclusions

Simple 90° and high performance W and M shaped ribs, both of 45° and 30°, were investigated under high rotation numbers at the entrance of a cooling channel. The Dittus-Boelter equation does not apply to developing flow, therefore results of the 90°, W and M-shaped ribs were compared to the stationary smooth wall condition. Comparing the simple and high performance ribs, the 30° M-shaped ribs performed slightly better than the 90° ribs. Wright

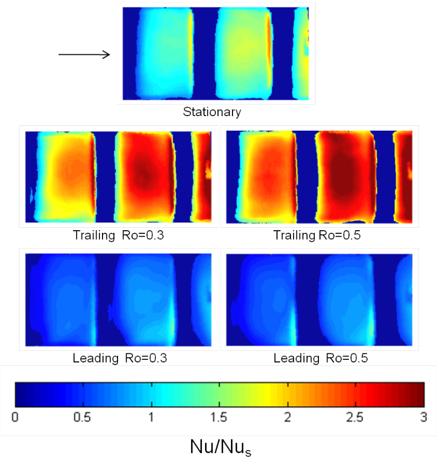

(a) 90° ribs.

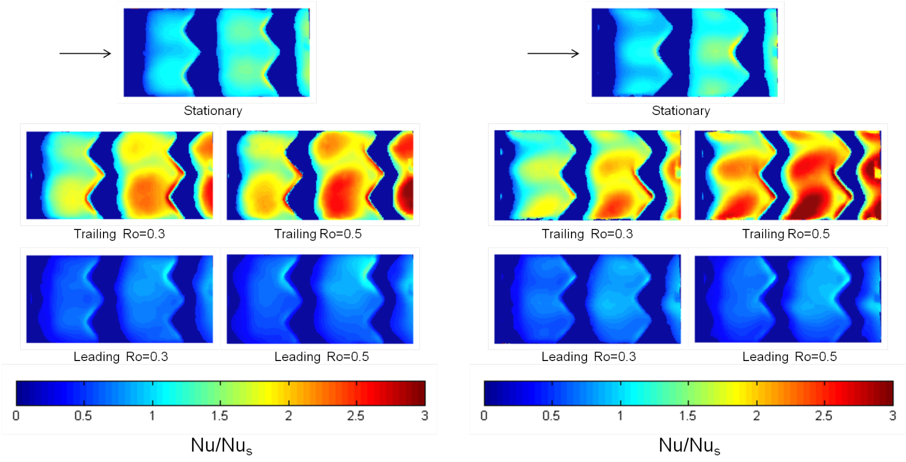

(b) 45° W ribs. (c) 45° M ribs.

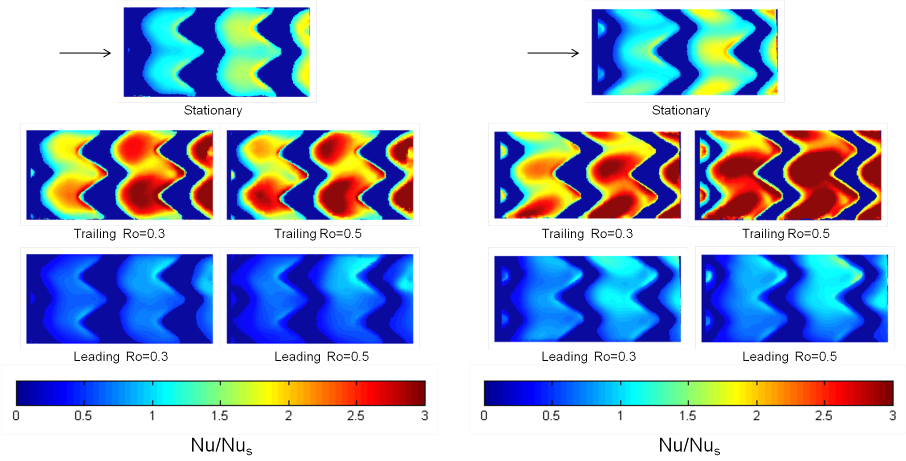

(d) 30° W ribs. (e) 30° M ribs.

Figure 6.6: Detailed results for all rib types.

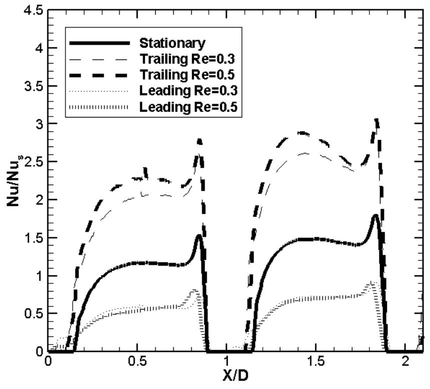

(a) 90° ribs.

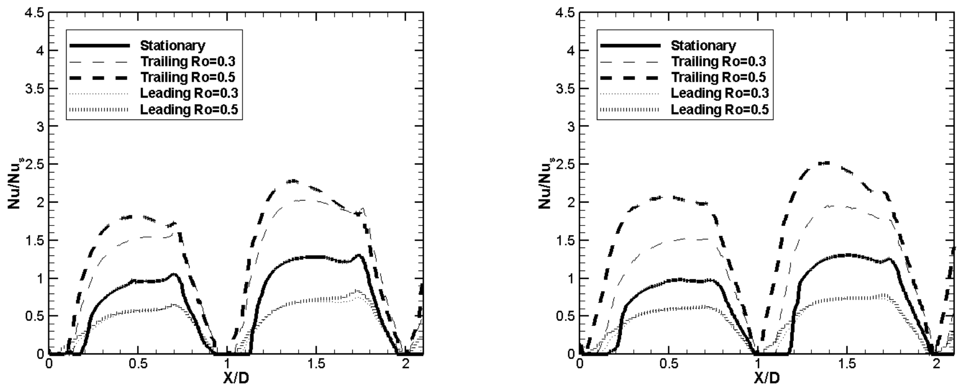

(b) 45° W ribs.

(c) 45° M ribs.

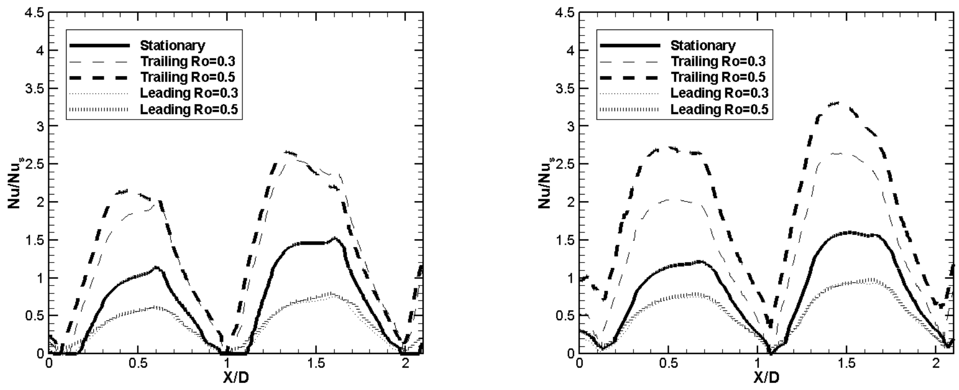

(d) 30° W ribs.

(e) 30° M ribs.

Figure 6.7: Spanwise average plots for each rib case.

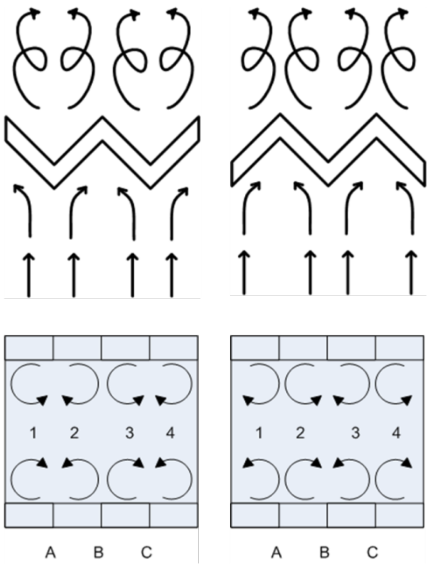

Figure 6.8: Swirling flow shed from the W/M-shaped ribs. This is speculative, but may explain the heat transfer distribution.

et al. [12] showed heat transfer due to 45° W-shaped ribs reached levels over 3 times that experienced by smooth walls in fully developed conditions. This gain is different inside the developing region. When the W and M-shaped ribs used 30° angles instead of 45°, sharper angles produced slightly higher heat transfer between the ribs. At higher rotation numbers, the trailing sides experience higher gains which as a result of the thinning boundary layer. The leading side cases show significant reductions in heat transfer compared to the stationary cases. Relative to Ro=0.3 and 0.5, the leading side cases show little change. The velocity gradient of the boundary layer can only be reduced so much. The Coriolis force does not induce a flow reversal, it only drives the gradient to zero, not negative values.

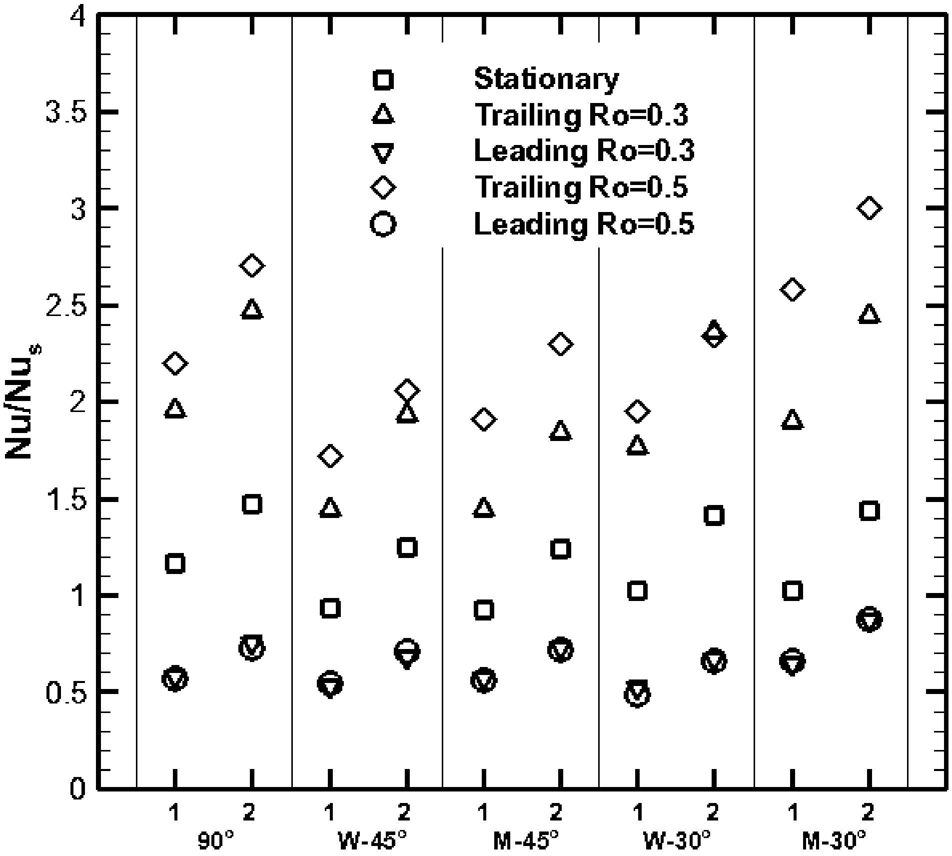

Figure 6.9: Average $Nu/Nu_s$ for each case before (1) and after (2) the center rib of the detailed plots.

Table 6.1: Average percent difference between the rotational and stationary cases before (1) and after (2) the center rib.

| Ro | %change | |
|---|---|---|
| 90 deg | 1 | 2 |
| Trailing-0.3 | 67.92 | 68.02 |
| Leading-0.3 | -50.51 | -48.81 |
| Trailing-0.5 | 88.85 | 83.64 |
| Leading-0.5 | -51.03 | -50.58 |

(a) 90° Ribs

| Ro | %change | |
|---|---|---|
| W-45 | 1 | 2 |
| Trailing-0.3 | 55.53 | 55.04 |
| Leading-0.3 | -43.18 | -45.84 |
| Trailing-0.5 | 84.32 | 64.96 |
| Leading-0.5 | -41.57 | -43.44 |

(b) 45° W shape Ribs

| Ro | %change | |
|---|---|---|
| M-45 | 1 | 2 |
| Trailing-0.3 | 56.37 | 48.39 |
| Leading-0.3 | -38.01 | -41.40 |
| Trailing-0.5 | 106.16 | 84.97 |
| Leading-0.5 | -39.42 | -42.28 |

(c) 45° M shape Ribs

| Ro | %change | |
|---|---|---|
| W-30 | 1 | 2 |
| Trailing-0.3 | 71.91 | 67.78 |
| Leading-0.3 | -49.27 | -52.41 |
| Trailing-0.5 | 89.99 | 65.58 |
| Leading-0.5 | -52.28 | -53.12 |

(d) 30° W shape Ribs

| Ro | %change | |
|---|---|---|
| M-30 | 1 | 2 |
| Trailing-0.3 | 85.13 | 70.45 |
| Leading-0.3 | -37.41 | -39.71 |
| Trailing-0.5 | 151.12 | 108.55 |
| Leading-0.5 | -35.67 | -39.08 |

(e) 30° M shape Ribs

# 7. Single Row Jet Impingement Array with Crossflow

Many industrial applications use jet impingement cooling, including gas turbine heat transfer. Numerous studies are available for stationary jet impingement systems. Studies have been performed with single jets and arrays of jets both staggered and inline. Florschuetz et al. [49] studied heat transfer distributions with a stationary array of jets and one outlet for the flow, causing spent coolant crossflow effects. Crossflow is spent coolant from upstream jets which can bend downstream jets, reducing their effectiveness. Close to the outlet, heat transfer drops in magnitude for most arrangements due to adverse effects of crossflow. Han et al. [2] provides a comprehensive survey of all jet impingement heat transfer papers prior to 2000. Uysal et al. [50] studied a single row of jets. The impingement configuration varied with non-uniform and uniformly spaced jet holes. Close to the outlet, a study observed a decline in heat transfer. Heat transfer increases linearly with increasing Reynolds number. At high Reynolds numbers, a jet-to-jet spacing of 7.5D performs slightly better than a spacing of 6.5D. At lower Reynolds numbers, the difference appears to be negligible. For a jet-to-jet spacing of 6.5D, a lower jet height-to-target plate distance increases heat transfer.

Very few published studies that have focused on rotational effects on jet impingement. One of the few, by Parsons et al. [17], focused on a complex rotating channel with jet impingement. For both the leading and trailing sides, heat transfer decreases below the stationary case. Contrary to rib roughened channels, heat transfer is augmented greatly if the Coriolis force is favorable (Wagner et al. [4], Parsons et al. [7], Liou et al. [46], Taslim et al. [6]). Also, Parsons et al. [17] measured lower heat transfer on the trailing side than on the leading side. Jet impingement generates a complex flow pattern, changing the influences of the Coriolis force compared to traditional rotating channels. Parsons et al. [17] uses two rows of holes; the interaction between the jets may have a greater effect on the velocity distribution, changing the effects of the Coriolis force.

The present study examines the effect of rotation on a radially outward channel with a single row of impingement holes and a crossflow exit condition, similar to Uysal et al. [50]. A novel transient liquid crystal technique is used to measure local heat transfer coefficients under rotating conditions.

A single row of constant pitch jet holes is used to demonstrate rotational effects on impingement and to validate a novel liquid crystal technique for rotating channels. Previous rotational studies of both serpentine channels and jet impingement have highlighted the importance of the leading and trailing sides of the coolant channel, as the Coriolis force acts normally away from and into the these walls, respectively, as shown in Fig. 5.1. Heat transfer results are presented for both leading and trailing sides under rotation.

## 7.1 Jet Impingement Test Section

The test section consists of a radially outward main channel and an impingement channel. Figure 7.3 shows the square main channel with a cross section of 2.54 cm sides. The inlet to the main channel of the test section is a transition from 2.54 cm circular cross section to the square 2.54 x 2.54 cm$^2$ cross section. The impingement channel has a width of 2.54 cm and the channel height-to-jet diameter ratio (H/$d_j$) varies by 1,2, and 3. The overall channel length-to-jet diameter ratio (L/$d_j$) of the impingement channel is 72. The mean rotating radius-to-jet diameter ratio (R/$d_j$) of the impingement channel is 108. The jet hole diameter ($d_j$) is 0.3175 cm for all tests. The pitch-to-jet diameter ratio (P/$d_j$) of the jet holes and the jet height-to-diameter ratio (b/$d_j$) are 8 and 1, respectively ([49]). A single outlet of the impingement channel creates the crossflow effect. The liquid crystals are applied on the impingement side of the target surface. A black backing coat is applied to allow for the camera to track the color changes. To simulate leading and trailing sides, the motor rotates the test section in opposite directions, as shown in Fig. 7.4.

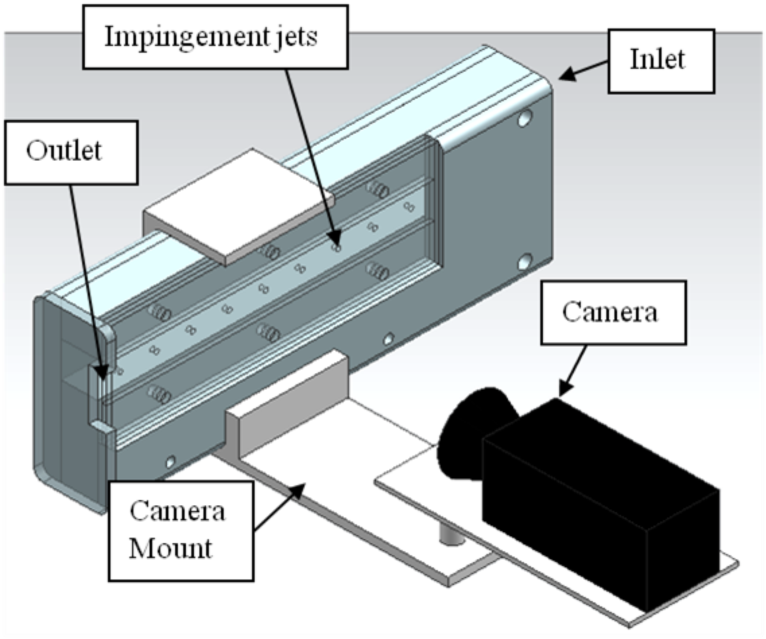

Figure 7.1: Illustration of test section and camera mount.

## 7.2 Results and Discussion

Results show how rotation affects heat transfer on the leading and trailing side walls compared to a stationary wall. The calculated flow distribution is used to verify the stationary cases with previous studies. The flow distribution aids in the explanation of the heat transfer results. Area average heat transfer (also referred to as the mean value) is presented for each jet, the maximum value for each jet, and the midline rake along the length of the impingement channel. The impingement channel size varies with jet surface to the target surface (H) by H/$d_j$=1,2, and 3. Rotational effects are explored for each of the individual H/$d_j$

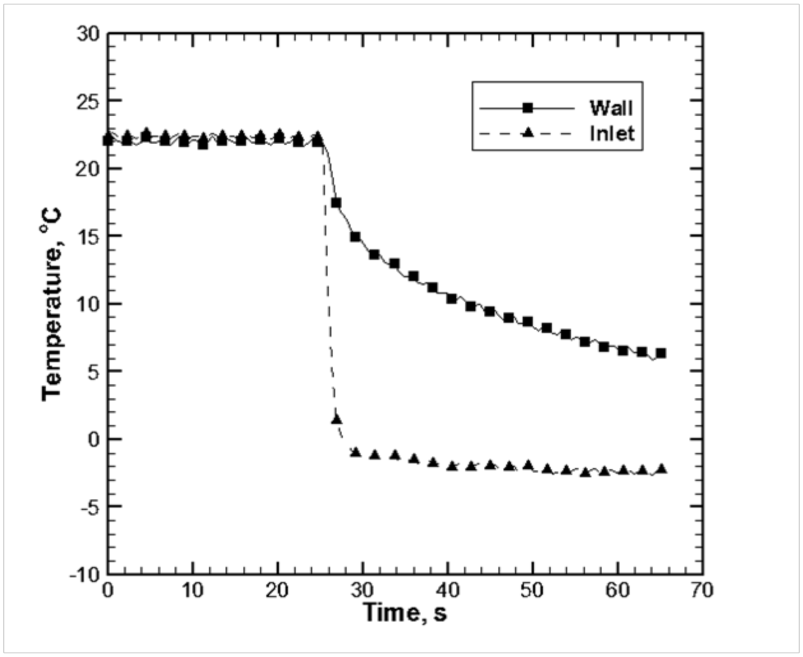

Figure 7.2: Temperature response for the coolant inlet and the wall temperature used for calibration.

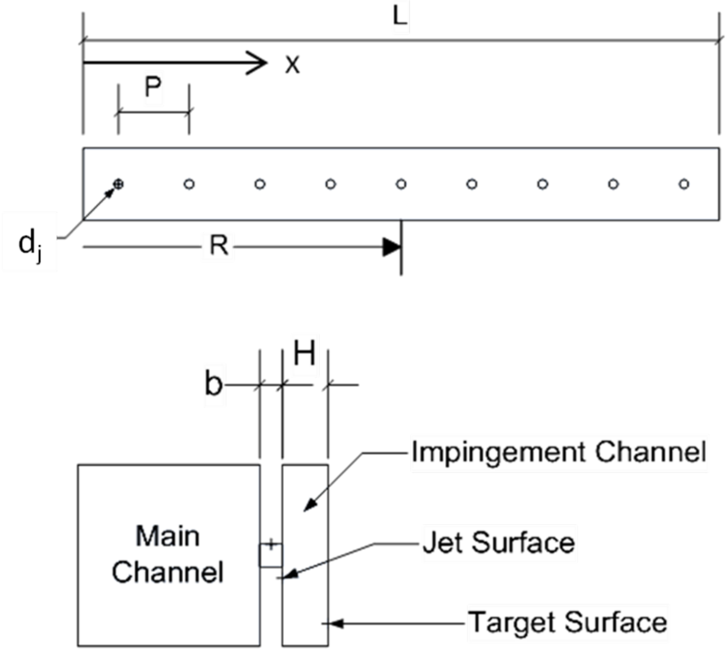

Figure 7.3: (Top) Lengthwise view of the test section. (Bottom) View looking straight down the channel.

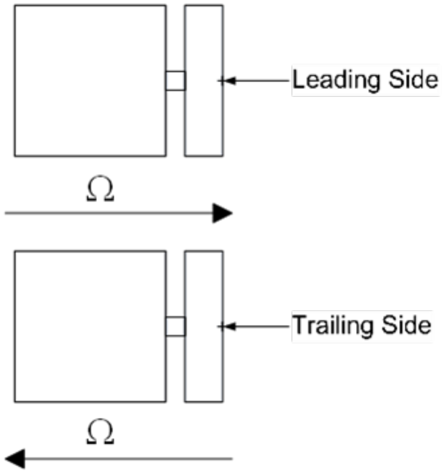

Figure 7.4: Illustration on how the target wall changes when the test section is rotating.

cases, as well as direct comparisons of H/$d_j$ results with each other. Heat transfer analysis includes the first seven jets, whereas the flow distribution is calculated for all nine. The BP for all cases is much less than 1, therefore buoyancy is not a dominating factor for the flow patterns. Flow conditions of $Re_j$=9,000; $\Delta T/T$ = 0.08; and $Ro_j$=0 to 0.0022 are maintained in the study. The effects on rotation on the jet structure is discussed, as well.

### 7.2.1 Flow Distribution

Uysal et al. [50] uses an inlet flow that is normal to the impingement jet faces. The inlet flow of the present study runs parallel to the impingement jet faces. Pressure measurements of the stationary case are used to determine the flow distribution. As evident in Fig. 7.5, the percent mass flow of coolant through each jet rises from jet 1 to jet 7. Mass flow through each jet is determined using the same method discussed in Gritsch et al. [51]. A subtle rise is present in H/$d_j$=2 and 3, whereas, a substantial rise occurs in H/$d_j$=1. Figure 7.6 shows the ratio of the mass flux of coolant crossflow to the mass flux through the individual jets ($G_c/G_j$). The crossflow becomes strong for the downstream jets for all the three cases. The

($G_c/G_j$) ratio for H/$d_j$=1 rises more quickly and reaches the highest overall level, indicating stronger crossflow. The small cross sectional area of the H/$d_j$=1 impingement channel leads to a high mass flux of crossflow. The high mass flux through the impingement channel leads to lower static pressures towards the end of the channel, which may be why more coolant is drawn at later jets.

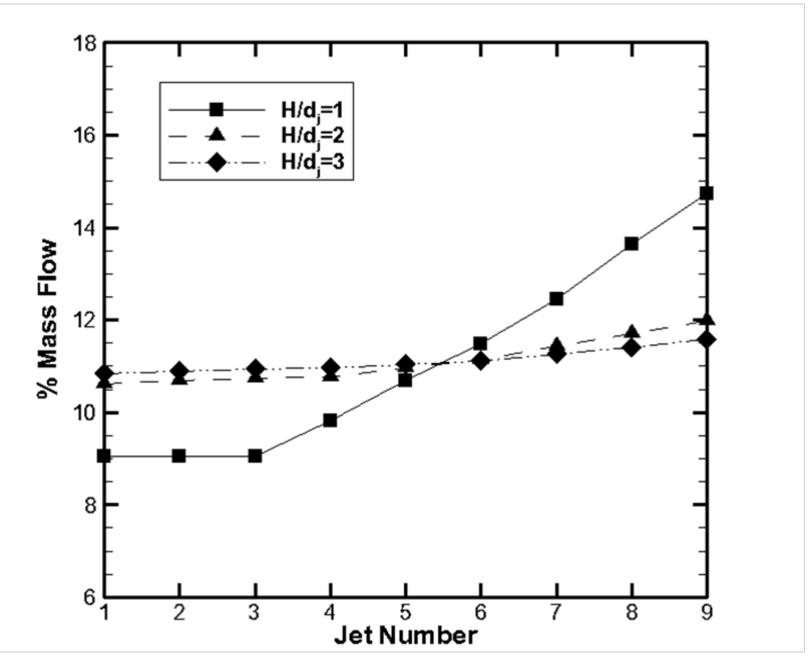

Figure 7.5: Percent mass flow through each impingement jet.

### 7.2.2 Rotational Effects on $H/d_j = 1$

Figure 7.7 shows the detailed results for the heat transfer on the target surface. From a qualitative standpoint, the trailing side heat transfer is consistently higher than the leading side and stationary results. The trailing side heat transfer is expected to be higher than the stationary and leading side, as stated earlier, due to the previous studies on serpentine channels by Wagner et al. [4], Parsons et al. [7], Liou et al. [46], and Taslim et al. [6]. However, this is in disagreement with Parsons et al. [17]. Parsons et al. [17] uses impingement channels

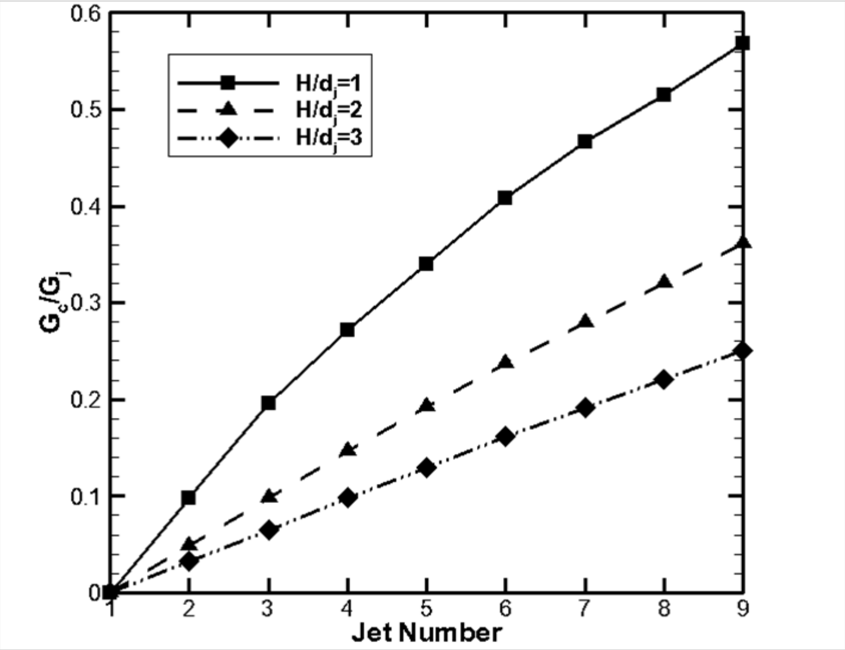

Figure 7.6: Crossflow-to-jet mass flux ratio along the length of the channel.

on both sides at the same time, whereas the present study uses one single impingement channel. Parsons et al. [17] uses two rows of impingement jets at a similar Re, providing more mass flow through the impingement channel. Figure 7.7 shows the mean and maximum values of heat transfer. The mean value rises from jet 1 to jet 7, while the maximum values decrease. Crossflow from previous jets act to bend the later jets away from the target surface, explaining why the maximum values decrease. Detailed results show that by jet 3, the heat transfer distribution under the jet appears to be a crescent instead of circular, a sign of the crossflow bending the jets. However, there is more mass flow towards the end of the channel. The coolant velocity increases with more mass flow. The velocity increase is significant enough to increase the overall heat transfer in the channel. The increased velocity aids the leading side, because it counteracts the detrimental effects of the Coriolis force. The Coriolis force increases the slope of the boundary layer on the trailing side, increasing heat transfer. The leading side experiences a decrease in the slope of the boundary layer, reducing heat transfer. The counteraction of the crossflow is apparent in the midline rake plot of the channel. The minimum values are increasing, while the maximum values are decreasing. This shows the crossflow is becoming more influential on the jets, in terms of heat transfer on the target surface. From Tab. 7.1, the leading side experiences the largest mean gain in heat transfer from jet 1 to jet 7. This is due to the crossflow, which counteracts the detrimental effects of the Coriolis force. The trailing side experiences slight gains, as the Coriolis force is already augmenting the heat transfer. Table 7.1 shows the average percent change in heat transfer between the trailing side and leading side with the stationary case. The trailing side experiences the largest gains due to the combination of crossflow and the Coriolis force augmenting heat transfer. The Coriolis force affects the main channel, causing the trailing side to be the high pressure side and the leading side to be the low pressure side. The high pressure of the trailing side forces the coolant through the jets faster causing the heat transfer on the trailing side to be higher than the leading side.

Table 7.1: H/$d_j$=1. Percent difference in mean and max heat transfer values between jet 1 and jet 7. Average percent difference between rotational cases and the stationary case.

| Jet 1-to-7 | Mean | Max |
|---|---|---|
| Stationary | 1.9 | -14.0 |
| Leading | 12.6 | -3.7 |
| Trailing | 1.3 | -15.0 |
| Rotational Change | Mean | Max |
| Leading | -6.2 | -22.6 |
| Trailing | 26.1 | 14.9 |

### 7.2.3 Rotational Effects on $H/d_j = 2$

Figure 7.8 shows the detailed results for the heat transfer on the target surface. Similar to the $H/d_j = 1$, the trailing side heat transfer is higher than the leading side and stationary results. The heat transfer on the trailing side clearly has higher maximum values at the center of the jets compared to the leading side and stationary cases. Also, in the area

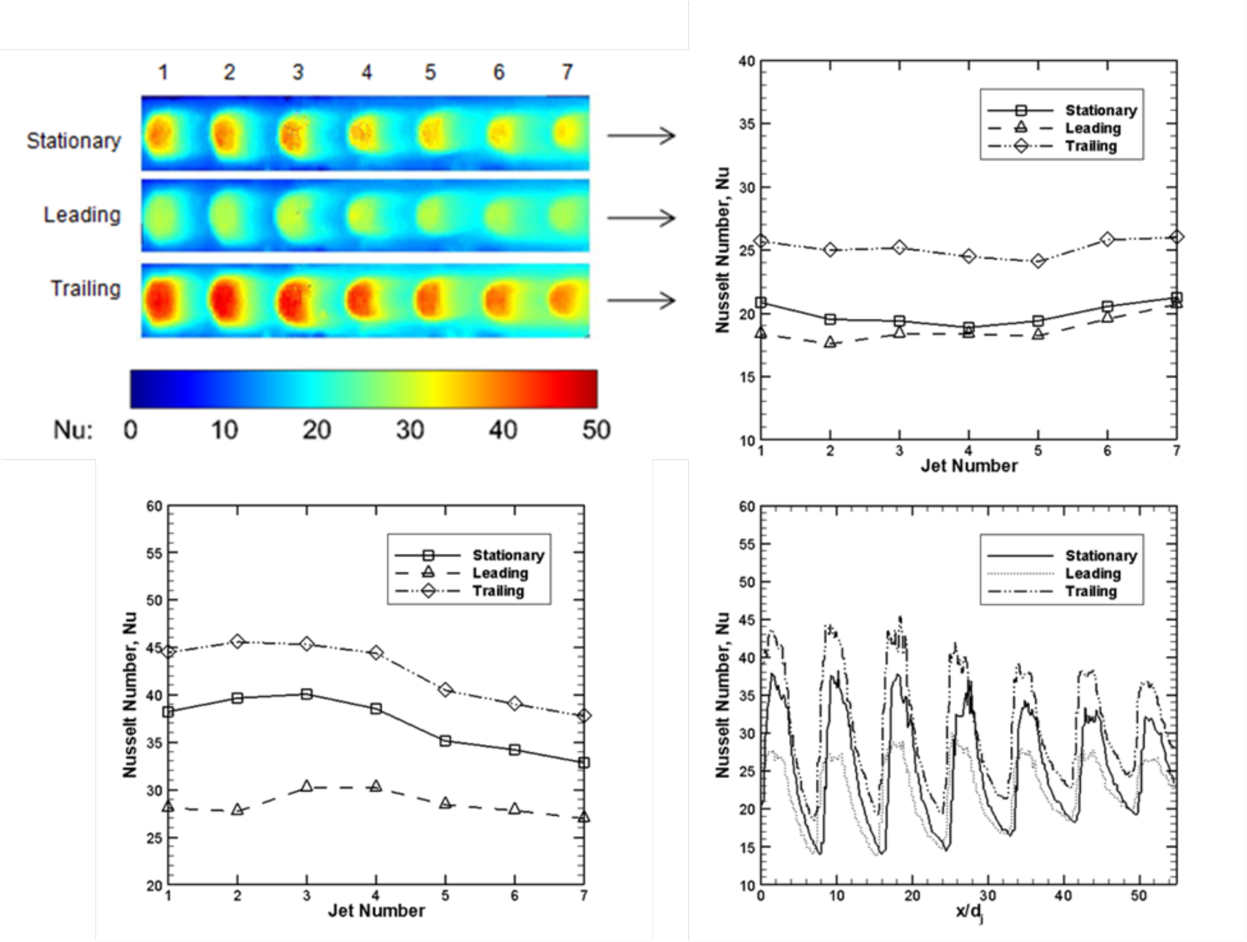

Figure 7.7: $H/d_j$=1. (top left) Detailed measurements along the channel for the first 7 jets. (top right) Average heat transfer around each jet. (bottom left) Maximum heat transfer values for each jet. (bottom right) Midline rake along the channel length.

between the jets, the heat transfer is highest for the trailing side. Figure 7.8 shows that both the mean and maximum heat transfer values drop across the channel. The channel is twice as large compared to the $H/d_j = 1$ case, therefore the crossflow velocity is only half. This would cause a reduction in heat transfer due to the crossflow itself and decrease its influence on the jets. The crossflow effect is still present, as the heat transfer distribution under the jets become crescent shaped around jet 5. The effect is not as pronounced as in $H/d_j = 1$, as shown in the midline rake. The minimum values appear to remain constant, not rise. The maximum values are affected, as they drop from jet 1 to jet 7. Table 7.2 shows the percent drop from jet 1 to jet 7. The largest drop in heat transfer occurs on the trailing side, which is due to the Coriolis force. Although the crossflow has beneficial effects, as seen in $H/d_j = 1$, it has detrimental effects on the jets. The developing boundary layer protects the target surface from the incoming jet, reducing the effectiveness of the jets. The leading side experiences a large increase in the boundary layer on the jet surface, where the coolant jets have the highest velocity. The high velocity of the jet opening allows the jets to resist the crossflow better than at the target surface. Table 7.2 shows the percent change in heat transfer between the leading side and trailing side compared to the stationary case. The Coriolis force may affect the main channel, causing the trailing side to be the high pressure side and the leading side to be the low pressure side. The high pressure of the trailing side forces the coolant through the jets faster causing the heat transfer on the trailing side to be higher than the leading side.

Table 7.2: H/$d_j$=2. Percent difference in mean and max heat transfer values between jet 1 and jet 7. Average percent difference between rotational cases and the stationary case.

| Jet 1-to-7 | Mean | Max |
|---|---|---|
| Stationary | -22.5 | -23.7 |
| Leading | -24.4 | -20.8 |
| Trailing | -31.0 | -31.4 |
| Rotational Change | Mean | Max |
| Leading | -13.3 | -8.91 |
| Trailing | 24.7 | 22.9 |

### 7.2.4 Rotational Effects on $H/d_j = 3$

Much like the $H/d_j = 2$ case, the trailing side experiences an overall increase in heat transfer over the stationary case, while the leading side experiences an overall decrease in heat transfer. Figure 7.9 shows the mean and maximum heat transfer values drop across the channel. Similar to the $H/d_j = 2$ case, the crossflow does not increase the heat transfer in the channel,

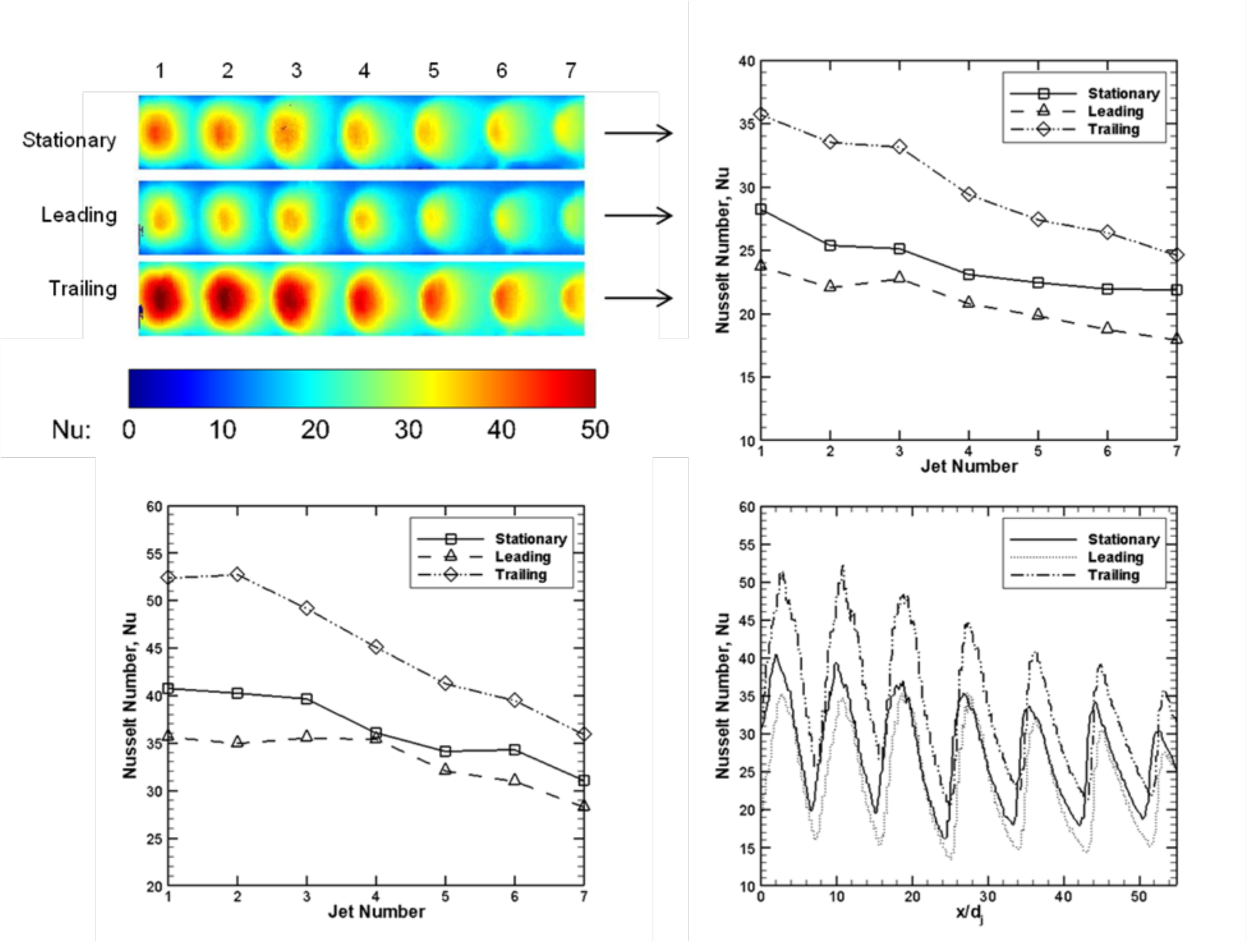

Figure 7.8: $H/d_j = 2$. (top left) Detailed measurements along the channel for the first 7 jets. (top right) Average heat transfer around each jet. (bottom left) Maximum heat transfer values for each jet. (bottom right) Midline rake along the channel length.

but acts to bend the jets away from the target surface, decreasing overall heat transfer. The midline rake plot shows that the minimum values are actually dropping, demonstrating the ineffectiveness of the crossflow to aid in heat transfer. The crossflow velocity is 1/3rd that of the $H/d_j = 1$ case, but is still influential because of the large area it acts over The crossflow effect is evident in the detailed plots by jet 6, where the heat transfer distribution begins to crescent. Comparing $H/d_j = 2$ to 3, less crossflow mass flux bends the jets away from the target surface for case 3. This is why there is less percent change from jet 1 to jet 7 for case 3 than case 2. Table 7.3 shows the percent difference between jets 1 and 7. Table 7.3 shows the percent difference between the stationary and rotating cases.

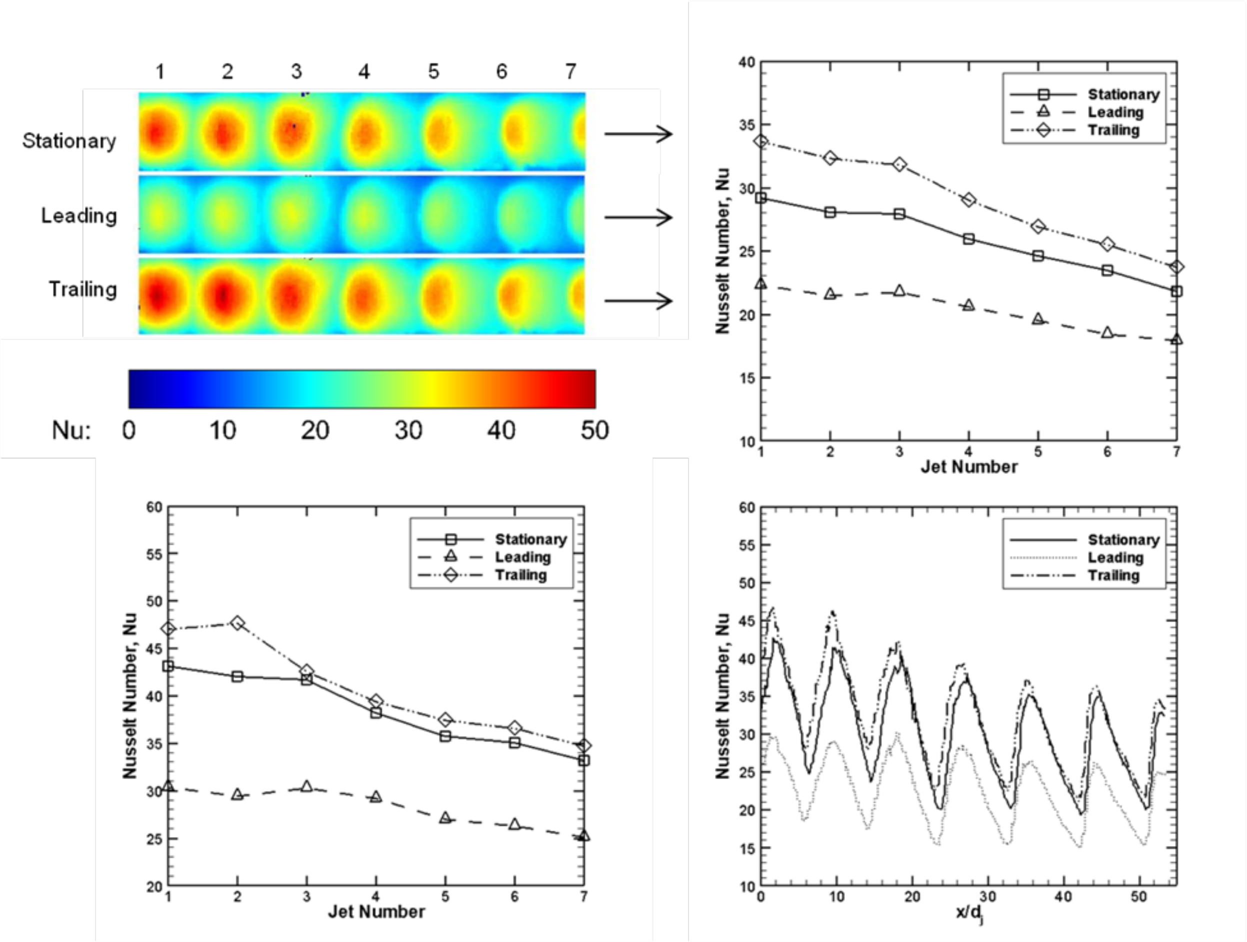

Figure 7.9: $H/d_j$=3. (top left) Detailed measurements along the channel for the first 7 jets. (top right) Average heat transfer around each jet. (bottom left) Maximum heat transfer values for each jet. (bottom right) Midline rake along the channel length.

Table 7.3: H/$d_j$=3. Percent difference in mean and max heat transfer values between jet 1 and jet 7. Average percent difference between rotational cases and the stationary case.

| Jet 1-to-7 | Mean | Max |
|---|---|---|
| Stationary | -25.2 | -23.0 |
| Leading | -19.9 | -17.2 |
| Trailing | -29.6 | -26.1 |
| Rotational Change | Mean | Max |
| Leading | -20.9 | -26.1 |
| Trailing | 12.5 | 6.20 |

### 7.2.5 Comparisons Between $H/d_j$ Cases

#### 7.2.5.1 Stationary

Figure 7.10 shows the mean heat transfer in the impingement channel as $H/d_j$ is varied from 1 to 3. As $H/d_j$ is increased, heat transfer increases for all jets. For the first jet, crossflow is not present. Comparing to single jet studies, as $H/d_j$ increases, the heat transfer increases until a certain threshold is reached. This threshold is where the potential core of the jet becomes fully developed. With a fully developed core, the centerline velocity is at its greatest, causing maximum heat transfer for a particular set-up. In Figure 7.10, a large increase in heat transfer is seen from $H/d_j$=1 to 2, and a small change from $H/d_j$=2 to 3. By examining Fig. 7.5, the percent mass flow through the first jet is considerably less for the $H/d_j$=1 case. The percent mass flow is slightly different for the first jet from $H/d_j$=2 to 3. For the remaining jets, the effect of the crossflow is evident. For $H/d_j$=2 and 3, the mean heat transfer has a steady decline from jet 1 to jet 7. The mass flux of crossflow acts to bend the jets away from the target wall. For $H/d_j$=1, the crossflow is very significant. From Figure 7.6, the ratio of crossflow-to-jet mass flux is considerably larger for $H/d_j$=1 than the other two cases. The mass flux is significant enough that the heat transfer begins to increase towards the end of the channel.

#### 7.2.5.2 Leading Side

Figure 7.10 shows the mean heat transfer in the impingement channel as $H/d_j$ is varied from 1 to 3. All $H/d_j$ results are lower than their corresponding stationary results. Distributions are similar, $H/d_j$=1 shows an increase at the end of the channel, while $H/d_j$=2 and 3 show a steady decline. A major difference is that the $H/d_j$=3 case is lower than $H/d_j$=2. Several factors may account for this. The first jet does not experience crossflow, however, $H/d_j$=2 is greater than $H/d_j$=3. The Coriolis force affects the main channel feeding the impingement jets, altering the distribution of mass flow through the jets. The amount of mass flow through jet 1 must be reduced, altering the local jet Reynolds number causing a reduction in heat transfer. The larger channel of $H/d_j$=3 produces a lower mass flux of crossflow. Due to the lower amount of mass flux, the Coriolis force is more dominant in deflecting the jets away from the target surface.

#### 7.2.5.3 Trailing Side

Figure 7.10 shows the mean heat transfer in the impingement channel as $H/d_j$ is varied from 1 to 3. As discussed earlier, all $H/d_j$ results are higher than their corresponding stationary results. The $H/d_j$=1 case shows the strong effects of crossflow at the end of the channel, which experiences a rise in heat transfer. Similar to the leading side, the $H/d_j$=2 case is slightly higher than $H/d_j$=3. This may be due to the change in mass flow distribution among the jets. Less mass flow may be going through the beginning jets, reducing the heat transfer. Similar to the leading side, the Coriolis force may play a more dominant role as the crossflow mass flux for $H/d_j$=3 is lower than that of the other two cases.

General trends have been validated. To validate the magnitudes of the results, single jet impingement studies are used for comparison. This is valid for jet 1 in the present study, as there is little to no crossflow at that point. Huang and Mohammed [52] studied the effect of Reynolds number and jet-to-plate distance on heat transfer. For a $Re_j$=6000, heat transfer results indicate maximum Nu at the center of the jet is slightly below 40 for $H/d_j = 1$ and slightly above 40 for $H/d_j$=2. This is close to the present study's maximum values for the stationary case, with similar Re.

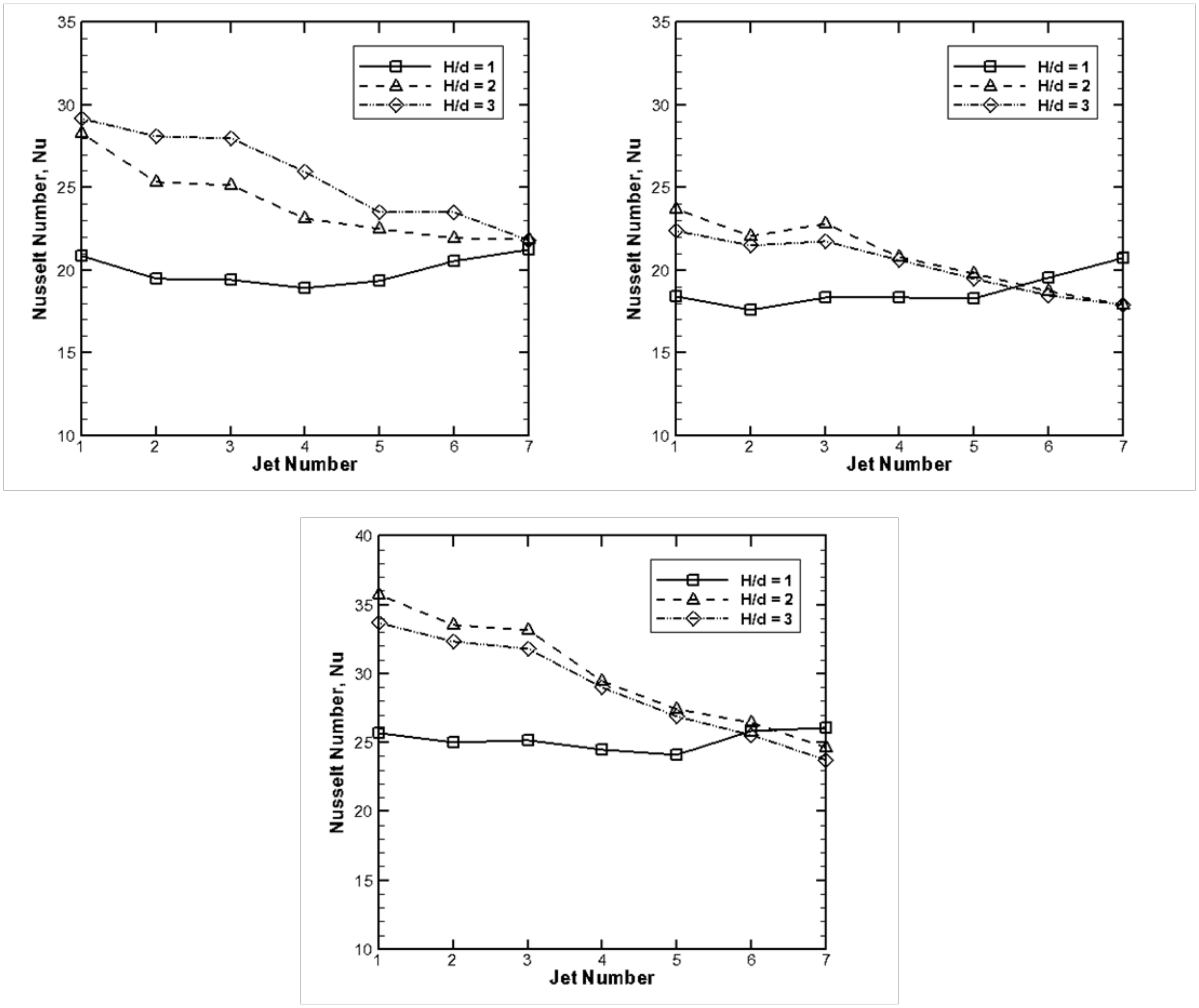

Figure 7.10: . (Top left) Stationary results for all $H/d_j$ cases. (Top right) Leading side results for all $H/d_j$ cases. (Bottom) Trailing side results for all $H/d_j$ cases.

### 7.2.6 Flow Analysis

The following section hypothesizes the effects of rotation on jet impingement and the effects occurring on the heat transfer distribution. Figure 7.11 shows schematics of the jets for the three $H/d_j$ cases and how the potential cores are affected with the Coriolis force and how the $H/d_j$ cases compare to each other. As shown by Striegl and Diller [53], an impinging jet consists of a potential core stemming from the nozzle and orifice, a shear layer, impingement region, and the wall jet region. The potential core tapers down in size from the orifice. When the potential core converges, the centerline velocity is at its greatest (due to continuity). Placing the target surface near the convergence of the potential core, causes the high centerline velocity to impact the target surface, causing high heat transfer. When the potential core has not reached this convergence, the centerline velocity is not as great, generating a smaller value of heat transfer. When the potential core becomes fully developed well before the target plate, the velocity begins to dissipate over the distance, reducing the heat transfer on the target plate.

Hypothetically, under rotational effects, the Coriolis force affects this potential core developing length and the size of the shear layer. For all cases, the leading side experiences a reduction in heat transfer. This may be due to the increased developing length of the potential core. The Coriolis force acts as an adverse pressure against the developing jet. This may flatten out the velocity profile coming from the orifice. With a flatter velocity profile, the developing length increases, reducing the cooling on the target surface compared to the stationary case. The Coriolis force aids the velocity profile on the trailing side. This creates a sharper velocity profile, so the potential core develops much quicker, increasing the heat transfer.

Because the trailing side potential core develops much more quickly, $H/d_j$=3 may become fully developed well before the target plate. This may cause some dissipation in the centerline velocity, which may explain why the heat transfer is slightly less than the $H/d_j$=2 case. On the leading side, the $H/d_j$=3 case experiences higher heat transfer than the $H/d_j$=2 case with the change in potential core length. There may be effects in the shear layer size that contributes to the changes in heat transfer. Figure 7.12 shows the first three jets of the channel under rotation. The first jet acts as an independent jet, as there are no jets upstream providing spent crossflow. The downstream jets get bent or pushed due to the spent crossflow from upstream jets. As the $H/d_j$ decreases, the spent flow velocity is higher due to reduced area for the same flowrate, resulting in stronger spent crossflow effects for smaller $H/d_j$. The velocity profiles in the impingement channel for the trailing and leading sides clearly show the effect of cross-flow on downstream jets. Tables 7.1,7.2,7.3 show that the leading side experiences less change from the 1st jet to the last jet compared to the trailing side cases. This may be because of the velocity profiles in the impingement channels. At the orifice, there is more momentum in the jet compared to the impingement surface, where momentum has been diffused somewhat to the entraining fluid. The higher momentum of the jet is able to withstand the steeper velocity gradient at the orifice (as seen on the leading side) than on the impingement surface (seen on the trailing side).

## 7.3 Conclusions

Detailed heat transfer distributions were measured using a novel transient liquid crystal technique for a rotating impingement channel. A camera was mounted on a rotating test section to film the liquid crystal's color change. The study of a simple rotating coolant channel with single row of impingement jets is used to demonstrate the quality of the measurements using this technique and will also help gain significant insight into the potential of using jet impingement as the dominant mode of convective cooling in rotating blades.

Results indicate that under the prescribed flow conditions in the experiments, there is an ideal $H/d_j$ for rotating channels which is different from an ideal $H/d_j$ for stationary channels. An $H/d_j$ of 3 is clearly the best (of the three cases studied) for the stationary case which is consistent with numerous studies on stationary impingement, while the rotating cases appear to be best at an $H/d_j$ of 2. Results clearly show similarities when compared to 2-pass coolant channels with rib roughened walls. For radially outward flow, the trailing

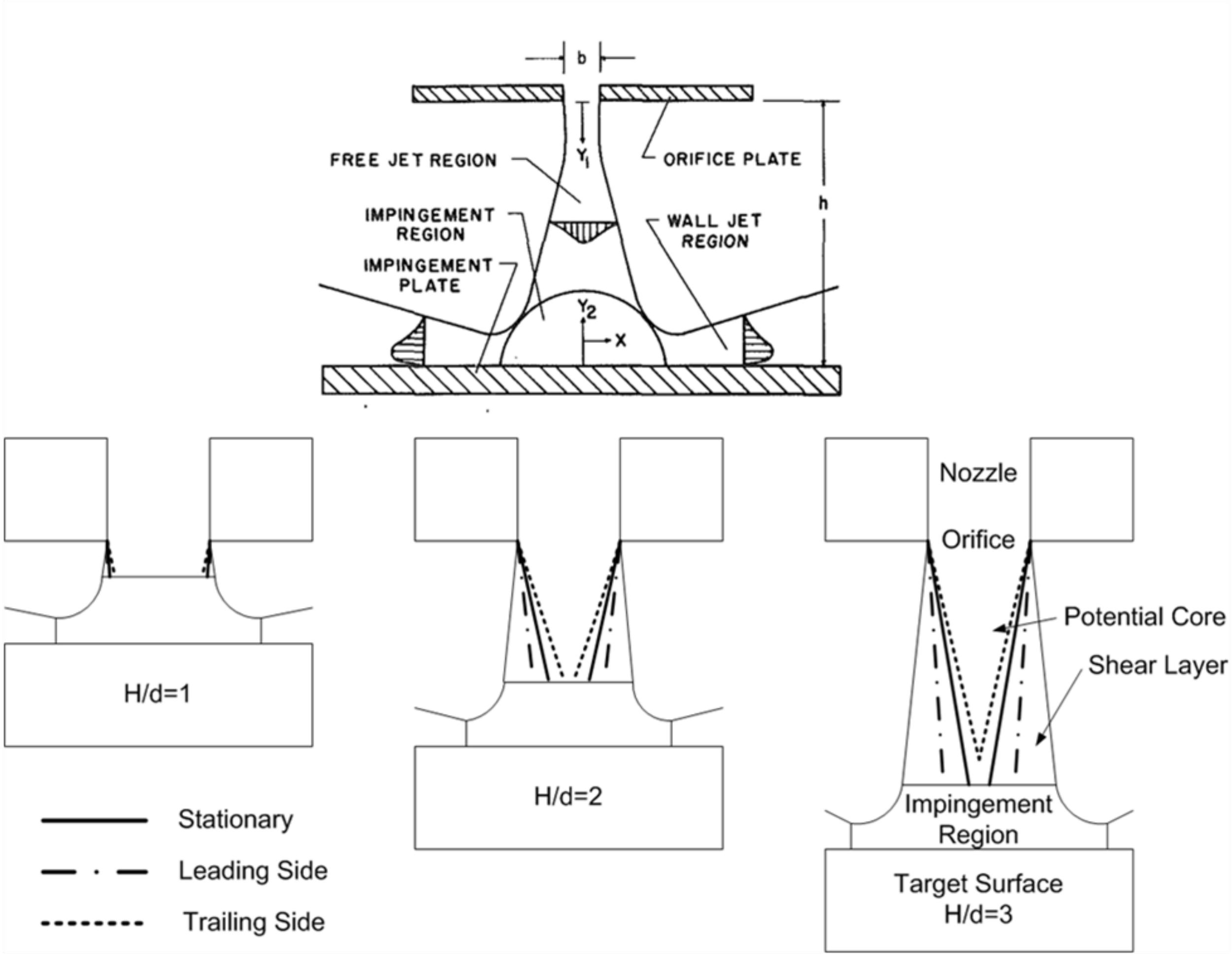

Figure 7.11: Illustrations of potential core development during rotation for all $H/d_j$ cases (top picture from Striegl and Diller [53]).

side experiences the Coriolis force favorably, causing an increase of the heat transfer. The leading side experiences a detrimental effect from the Coriolis force. The same phenomenon affecting jet impingement in the present configuration affects traditional serpentine channels, but with the additional complexity of crossflow and jet length. The Coriolis force plays a major role in the development of the potential core of the jets, greatly altering the heat transfer distributions.

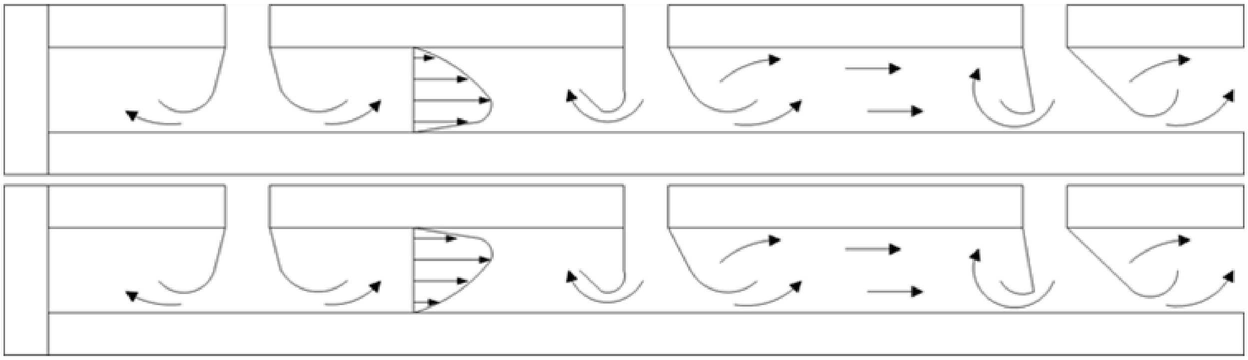

Figure 7.12: View inside of the impingement channel. The first jet experiences little to no crossflow. The later jets are bent due to crossflow. (top) Velocity profile in the trailing side channel. (bottom) Velocity profile in the leading side channel.

# 8. Various Jet Impingement Configurations with Rotation

The present study examines the effect of rotation on a double row of impingement jets with a crossflow exit condition similar to Parsons et al. [17]. A novel transient liquid crystal technique is used to measure local heat transfer coefficients. The present study uses chilled air and room temperature walls to obtain the proper buoyancy effect for testing and to allow the use of clear acrylic walls for liquid crystal color capture. The present study models a single radially outward coolant channel with jet impingement. The study focuses on the effects of rotation for two different jet configurations: 90° and 70° orientation and jet-to-target surface distance. Previous rotational studies of both serpentine channels and jet impingement have highlighted the importance of the leading and trailing sides of the coolant channel, as the Coriolis force acts normally away from and into the these walls, respectively, as shown in Fig. 8.1.

## 8.1 Test Section

Several test section configurations are explored in this study. Figure 8.2 (top) shows an inward view of the 90° and 70° test configurations. All configurations consist of a main channel which feeds the coolant to the impingement jets. The inlet to the main channel is a step from a 2.54 cm circular cross section to a 2.54 x 2.54 $cm^2$ square cross section. The main channel is square in cross section with 2.54 cm sides. The jet diameter (d) is held constant for this study at 0.3175 cm (0.125 in). The jet length (b) is also held constant at 0.3175 cm (0.125 in). The width of the impingement channel is held at 2.54 cm, while the height (H)

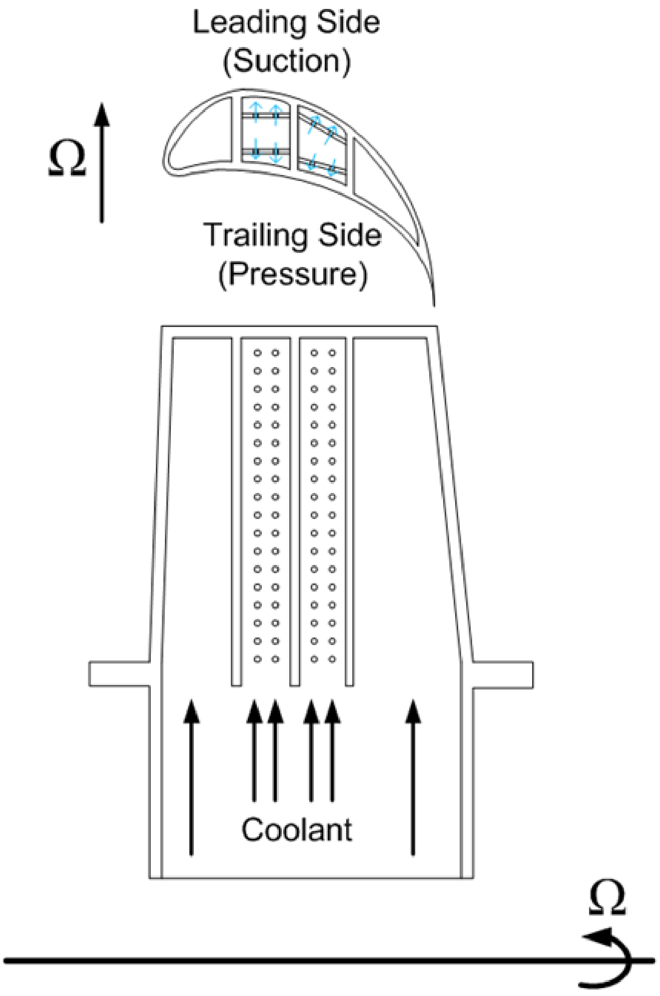

Figure 8.1: A standard turbine blade with internal coolant channels. (Top) cross section of blade. (Bottom) cutaway view of coolant channels.

varies by 1d, 3d, and 5d. Liquid crystals are applied to the target surface, as it is the area of interest that will be studied. Under rotation, the target surface is both the leading and trailing side (depending on the direction of rotation). Case I has two rows of jets oriented 90° to the target surface, Case II has two rows of jets oriented at 70° to the target surface. Figure 8.2 (bottom) shows a side view of the test section. The total length (L) of the test section is 72d and the width (w) is 8d. The double row of jets have a pitch (P) of 5d, but the rows are spaced 3d apart (5/2d from edge with respect to the inlet of the jet).

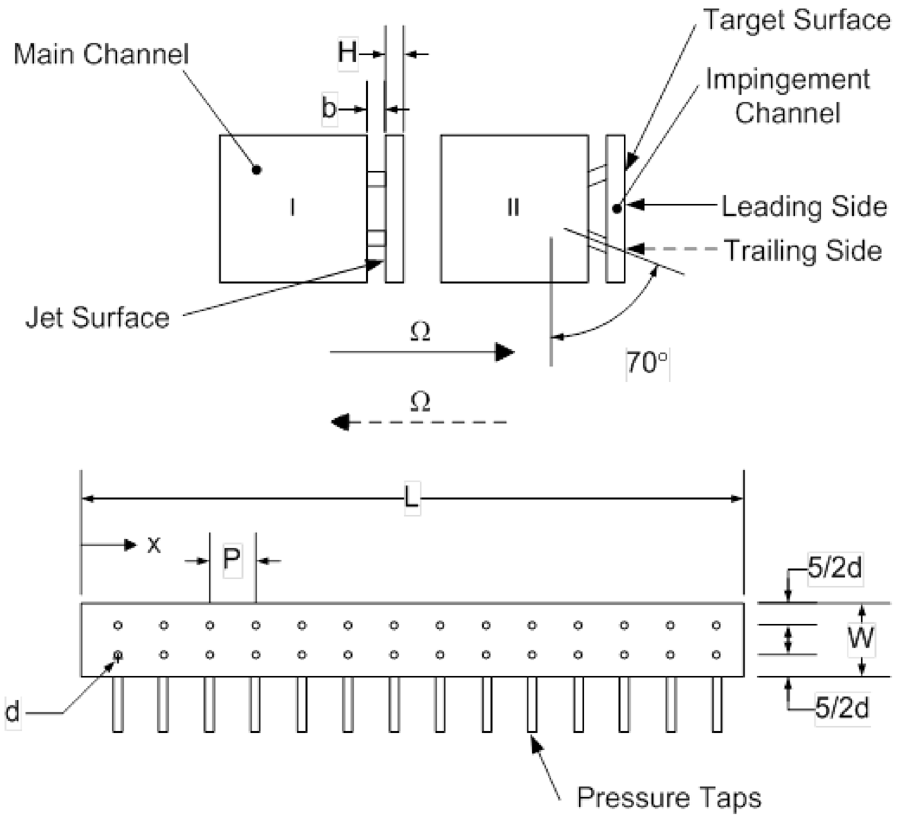

Figure 8.2: (Top) Inward view of the test sections. (Bottom) Lengthwise view of the test section.

## 8.2 Results and Discussion

Results presented in this section show how rotation affects heat transfer on the leading and trailing side walls compared to a stationary wall. The flow distribution is calculated for the stationary cases to verify that the model is consistent with expectations and previous studies and to help explain the heat transfer results. Heat transfer results are presented by determining the span-wise average heat transfer along the length of the channel. The stationary spanwise average is presented for all cases studied. Area averaged heat transfer results are calculated for all cases studied in locations like that shown in Fig. 8.3; the rotational case results are presented relative to the stationary cases. The impingement channel size is varied by altering the distance from the jet surface to the target surface (H) by H/d=1,3, and 5. Each configuration is studied at rotational speeds of 0 and 216 rpm. The buoyancy parameter (BP) for all cases is much less than 1, therefore, buoyancy is not a dominating factor for the flow patterns. Each case ran at Re=5,000; $\Delta T/T = 0.08$; and varied from Ro=0 to 0.00303.

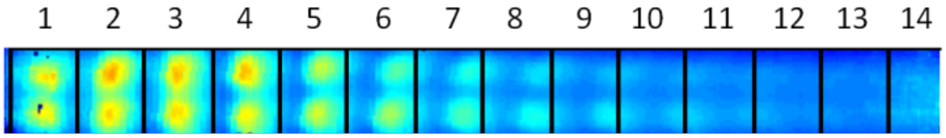

Figure 8.3: Regions used for area average heat transfer calculations.

### 8.2.1 Flow Distribution

Pressure measurements before and after the coolant flows through the jets allow an estimation of how much coolant is passing through each jet. This information aids in the explanation of heat transfer distributions, presented in the following sections. The static pressure in the main channel is taken in three locations: the entrance, mid-point, and end of channel. For all cases studied, the static pressure remains the same at each location. All pressure measurements are taken for the stationary case, as it is assumed that the flow distribution changes little during rotation. The mass flow rate of coolant through each jet is determined using the same method as Gritsch et al. [51]. This method requires the static pressure of the main channel and the static pressure after the jet, which is taken from the impingement channel. Figure 8.4 shows percent mass flow rate through each row of jets (as there are two columns of jets). For both the 90° and 70° jet orientations, when H/d=1, the mass flow distribution varies considerably from the entrance to the exit. This is due to the small cross section of the impingement channel, causing the coolant to accelerate to a high velocity towards the end of the channel. The high velocity causes a drop in the static pressure, which is why more coolant is drawn towards the end of the channel. Distributions are very similar for H/d=3 & 5, where the slightly higher variation in H/d=3 is caused by the same reasons H/d=1 varies, just to a much less extent. Both of the 90° and 70° jet types have similar flow distributions, however, the 70° varies slightly more for all H/d cases. This is due to the added turning of the jet, which increase the pressure drop.

Figure 8.4 shows the percent crossflow for all cases studied. H/d=5 shows the least percent crossflow, as the cross section is the largest. Distributions are similar for 90° and 70°. Similar distributions are also present in H/d=3 & 1. The H/d=1 crossflow result curves are not as smooth as that in the H/d=5 & 3. H/d=1 has the smallest cross section, which creates higher velocities perhaps making the flow distribution much more complicated.

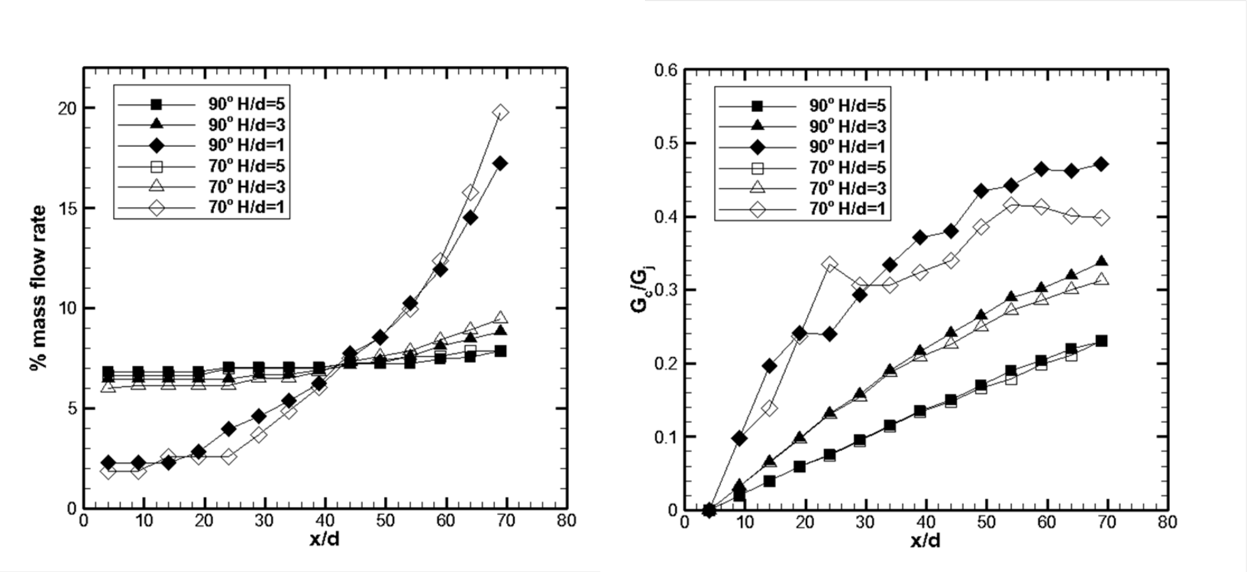

Figure 8.4: (Left) Percent mass flow through each set of jets for all stationary cases studied. (Right) Crossflow of the spent coolant from upstream jets for all stationary cases studied

### 8.2.2 Double Row 90° Jets

Figure 8.5 shows the detailed results for all stationary H/d cases as well as line plots for the spanwise average along the length of the impingement channel. Each line plot shows the spanwise average Nu value along the length of the channel for the stationary case. Similar spanwise average calculations are done for the rotating cases, the leading and trailing sides. The rotating average values are compared to the stationary results, generating $Nu/Nu_o$ values.

#### 8.2.2.1 H/d=5

The detailed heat transfer measurements show the coolant flows from from left to right. The beginning of the impingement channel shows relatively high heat transfer, then tapers off as x/d increases, which is evident in the upper right spanwise average plot of Fig. 8.5. Although H/d=5 experiences the least crossflow of the three H/d cases studied, the jet still overcomes the greatest distance from the exit of the jet surface to the target surface. With this increased distance, the crossflow is powerful enough to divert the jet away from the target surface. The upper right plot of Fig. 8.5 shows the comparison between the rotating and stationary cases. During rotation, heat transfer varies slightly. The upper right plot of Fig. 8.5 shows stationary and rotating results from Parsons et al. [17]. Stationary heat transfer are similar to that seen in the present case. Although Parsons et al. [17] uses the same pitch between jets along the length of the channel, the spacing between the rows is 5d instead of 3d, which is used in the present study. Also, the jet developing length in Parsons et al. [17], b, is larger than that used in the present study (5.2d instead of 1d which is used in the present study). These differences may explain the small discrepancy in the stationary results.

#### 8.2.2.2 H/d=3

The detailed results show the heat transfer remains relatively constant along the length of the channel. The maximum values taper down to lower values, but the average remains the same. This is also evident in the lower left plot of Fig. 8.5, showing the spanwise average along the length. As x/d increases the minimum and maximum values dampen down to a constant average value, indicating crossflow effects. The discrete high heat transfer regions caused by the jets at the beginning of the impingement channel steadily merge together as x/d increases. The crossflow velocity is large enough to increase the heat transfer, whereas in the larger H/d=5 channel, the crossflow does not aid in heat transfer. Heat transfer on the leading and trailing sides do not change considerably compared to the stationary value. The small changes are relatively constant along the length of the channel for both leading and trailing sides.

#### 8.2.2.3 H/d=1

Detailed results show the heat transfer steadily increases as x/d increases. Since H/d=1 cases have the smallest cross section of any cases studied, the crossflow velocity is much greater. The high velocity coolant at the end of the channel draws more coolant out of the jets at the end of the channel. The coolant is drawn out of the jets at the end of the channel with enough force to break past the crossflow and impact the target surface. In contrast to the H/d=3 results, the crossflow was enough to aid in heat transfer, but reduced the effectiveness of the jets at the end of the channel, which is evident by the dampening of the minimum and maximum heat transfer values. For H/d=1, the oscillation between minimum and maximum values of the spanwise average remains for all jets.

In traditional cooling techniques using channels with ribs or dimples, the trailing side ex-

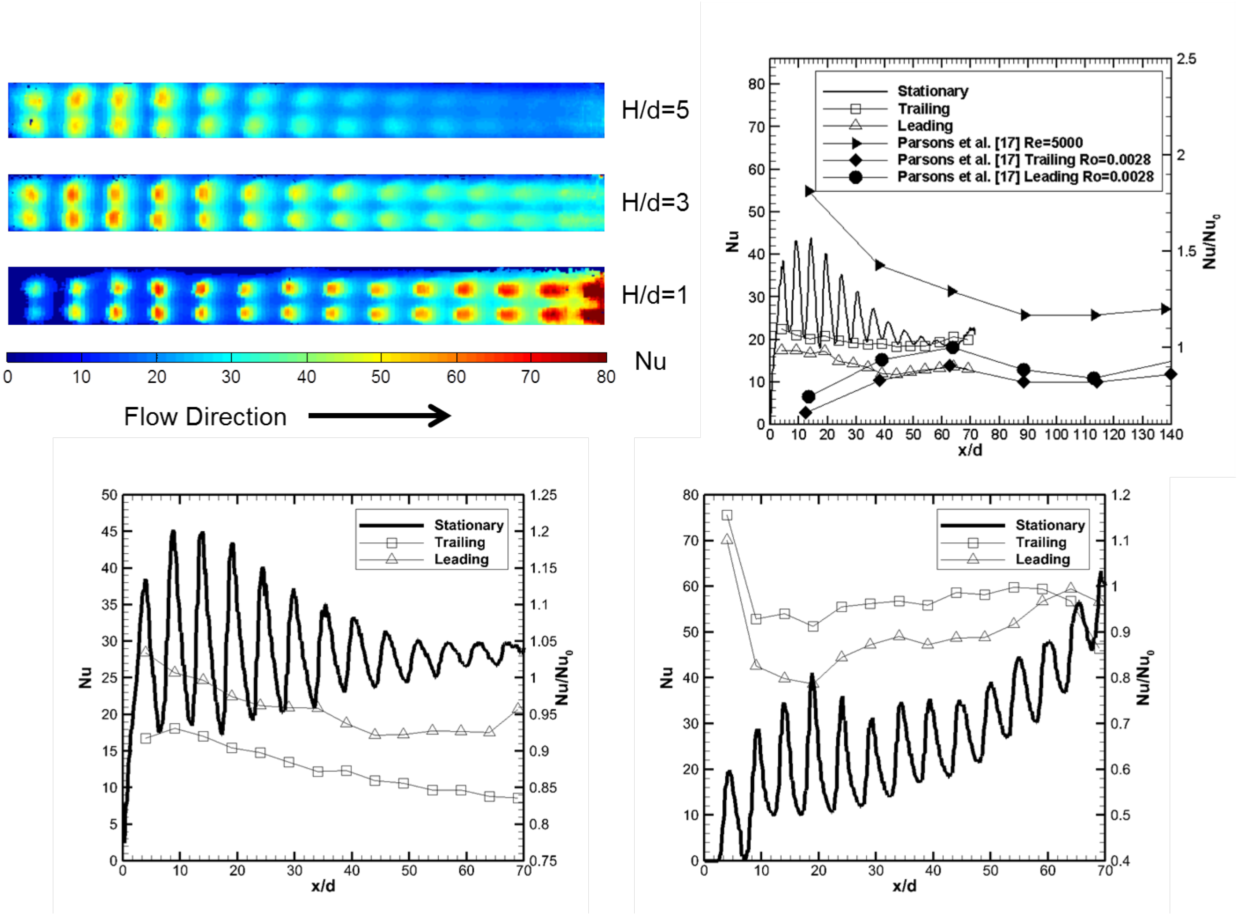

Figure 8.5: 90° Results. (Top left) Detailed heat transfer results for the stationary cases. Span-wise average results along the length of the channel for stationary case with relative changes during rotation for H/d=5 (Top right), H/d=3 (Bottom left), and H/d=1 (Bottom right).

periences an increase in heat transfer, while the leading side experiences a decrease. This is due to the Coriolis force. Both of the leading and trailing sides of the present study's impingement channel vary little or drop compared to the stationary case. As shown in the upper right plot of Fig. 8.5, the leading and trailing side heat transfer values hover at or below 1, which is true for Parsons et al. [17]. The development of the boundary layer inside the impingement channel is affected by the Coriolis force. Although the Coriolis force acts differently on the leading and trailing sides, the jet penetrates both boundary layers, making it more difficult for the jet to penetrate through. This reduces the effectiveness of the jets.

### 8.2.3 Double Row 70° Jets

#### 8.2.3.1 H/d=5

Similar to the 90° jet case, the high initial heat transfer tapers off as x/d increases. The maximum and average heat transfer are similar to that of the 90° case. The most noticeable difference for the 70° case is the separation of the impact locations for the jets on the target surface. Although the developing length of the jet, b, is relatively short, the jet is able to direct the coolant. In the latter part of the impingement channel, a low heat transfer region is in the center, due to the separation of the impact locations. The jets, although greatly affected by the crossflow at the end of the channel, are slightly more effective than the 90° jets, as shown in the detailed plot of Fig. 8.6 by the heat transfer enhancement along the edges of the channel, where the 70° jets are directing the coolant. Also, the upper right plot of Fig. 8.6 shows the stationary average heat transfer to be slightly higher than that seen in the corresponding 90° case. Similar to the 90° case, the effects of rotation are not great, as heat transfer varies little to the stationary case.

#### 8.2.3.2 H/d=3

Similar to the 90° case, heat transfer maximums and minimums dampen as x/d increases, but maintains a constant average. The points of impact of the jets on the target surface are more spread out than the 90° case, but not as spread out as the H/d=5 case. Again, the rotating case results are similar to the stationary results.

#### 8.2.3.3 H/d=1

Compared to the 90° case, 70° span-wise average heat transfer in the lower right plot of Fig. 8.6 are considerably less. The 90° and 70° cases have similar mass flow distributions, however little coolant is passing through the jets at lower x/d values, the angle of the 70° jets are not effective as they divert coolant slightly away from the target surface. During rotation, the H/d=1 case experiences the largest relative changes for both the leading and trailing sides. Since the heat transfer is relatively low in the stationary case, slight changes in the heat transfer due to rotation cause more relative changes than the other H/d cases. Even at large x/d values, the span-wise average results are less than that in the 90° H/d=1 case.

### 8.2.4 90° and 70° Comparisons

Figure 8.7 shows the 90° and 70° plots comparing the individual H/d cases. For H/d=5, the 70° jets provide similar, if not slightly higher span-wise average values than the 90° case. Changes due to rotation are similar for both cases, with only slight changes compared to the stationary. H/d=3 shows almost identical results for both the 90° and 70° cases. Again, the changes due to rotation are similar for both cases. H/d=1 shows noticeable differences between the 90° and 70° spanwise average values, where the 90° shows higher results. Both cases show a similar rising trend. Changes due to rotation are more prevalent for the 70° case than the 90° case.

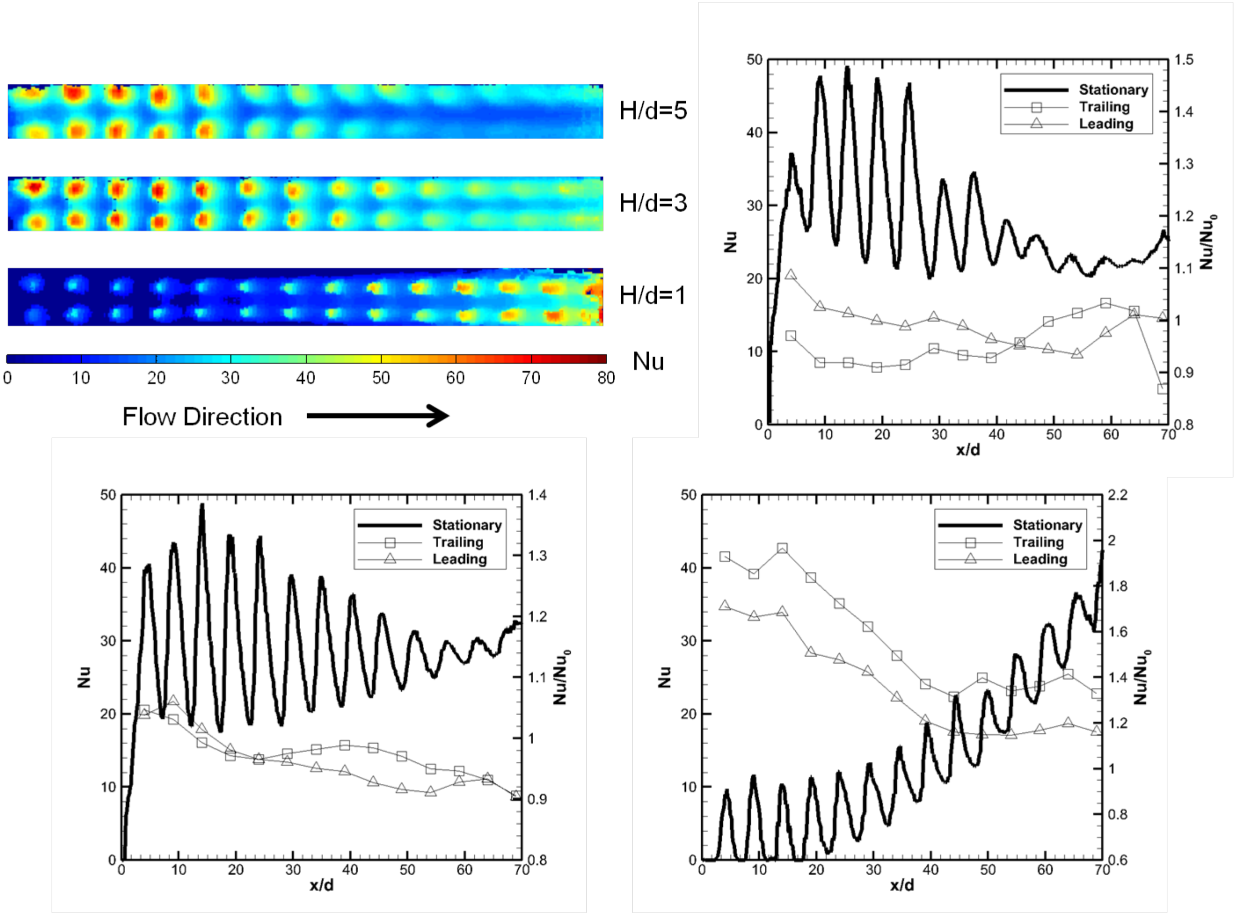

Figure 8.6: 70° Results. (Top left) Detailed heat transfer results for the stationary cases. Span-wise average results along the length of the channel for stationary case with relative changes during rotation for H/d=5 (Top right), H/d=3 (Bottom left), and H/d=1 (Bottom right).

## 8.3 Comparison with Ribbed and Jet Impingement Studies

Figure 8.8 shows all results, stationary and rotating, for ribbed and jet impingement cooling schemes studied in this dissertation. Figure 8.8 plots the average Nu for each case compared to the dimensionless pressure drop in the system. Dimensionless pressure drop is defined as the ratio of the static and dynamic pressure. Pressure drop in the two-pass channel is defined as the loss between the first rib of the first pass and the last rib of the second pass. Coolant for the jet impingement schemes exit to atmosphere, therefore the pressure drop is from the inlet of the main supply channel to atmosphere.

For jet impingement schemes, Nu is based on the channel hydraulic diameter of the main supply. This is a different definition from their respective chapters, however, Nu was manipulated to provide apples-to-apples comparisons between jet impingement and two-pass channels. The main supply channel for jet impingement schemes are the same dimensions as the two-pass channel (1inx1in). Total mass flow through the jet impingement and two-pass systems are provided in Tab 8.1. The study with a single row of jets, collectively use less coolant, but with fewer jets than the double row, higher jet Re is achieved.

All jet impingement schemes have higher pressure losses compared to the normal two-pass channel configurations. Although the mass flow of coolant in the single row of jets is less than the other cases, the dimensionless pressure required is considerably higher. More coolant is passing through each individual jet for the single row of jets, as shown in Tab. 8.1, causing much higher pressure losses. Single row jets H/d=2 and 3, double row 90° and 70° H/d=3 and 5 have similar average Nu, however, the pressure losses are significantly higher for the single row of jets. The double row 90° H/d=1 average Nu is relatively high, however, much higher pressure losses are associated compared to H/d=3 and 5. Double row 70° H/d=1 has very high pressure loses with very little Nu benefit compared to the 90° jets case. Higher heat transfer is achievable with jet impingement, but pressure losses can be severe. As H/d increases from 1 to 5, pressure losses are reduced remarkably, while maintaining high heat transfer on the target surface.

Table 8.1: Total mass flowrates of jet impingement and two-pass channel studies.

| | **Jet Angle** | **total mass flow(kg/s)** | **Re$_j$** | **Re$_{ch}$** |
|---|---|---|---|---|
| **Jet Impingement - Single Jet** | **90°** | 0.00357 | 9000 | 7952 |
| **Jet Impingement - Double Jet** | **90°** | 0.0063 | 5000 | 14021 |
| **Jet Impingement - Double Jet** | **70°** | 0.0063 | 5000 | 14021 |
| **Two-Pass Ribbed Channels** | **-** | 0.007 | N/A | 15579 |

## 8.4 Conclusions

The present study focuses on the effects of rotation, H/d, and jet orientation for a jet impingement cooling scheme with a crossflow exit condition. For Ro=0.003, heat transfer varies little compared to the stationary cases. There are, however, considerable differences in the heat transfer magnitude and distribution along the length of the channel. The crossflow for H/d=5 negatively affects the jets at larger x/d values. The jets are diverted away from the target surface, reducing the heat transfer. For H/d=3, the crossflow also deflects the jets away from the target surface, but not to the extent in H/d=5. For H/d=3, the impingement channel becomes similar to a traditional coolant channel, where the crossflow velocity is large enough to enhance the heat transfer. At low jet-to-target spacing, H/d=1 shows significant differences from the H/d=3 & 5 cases. The crossflow velocity becomes very high, causing the static pressure at the end of the channel to drop low enough that more coolant is extracted from the jets at larger x/d values, making the jets at low x/d values ineffective. Heat transfer distributions and magnitudes are similar for both 90° and 70° jet orientations. The location on the target surface where the jets impact is one of the only real differences between the 90° and 70° jets. The separation caused by the 70° jets creates a noticeable low heat transfer region at high x/d values for H/d=5, but does not change the average heat transfer values much compared to the 90° case. The largest difference in magnitude observed is for the H/d=1 case at 70° orientation. The heat transfer is considerably less than that in the 90°

case, because at low x/d values, little coolant passes through the jets. The 70° orientation diverts the coolant away from the target plate, providing very little benefit.

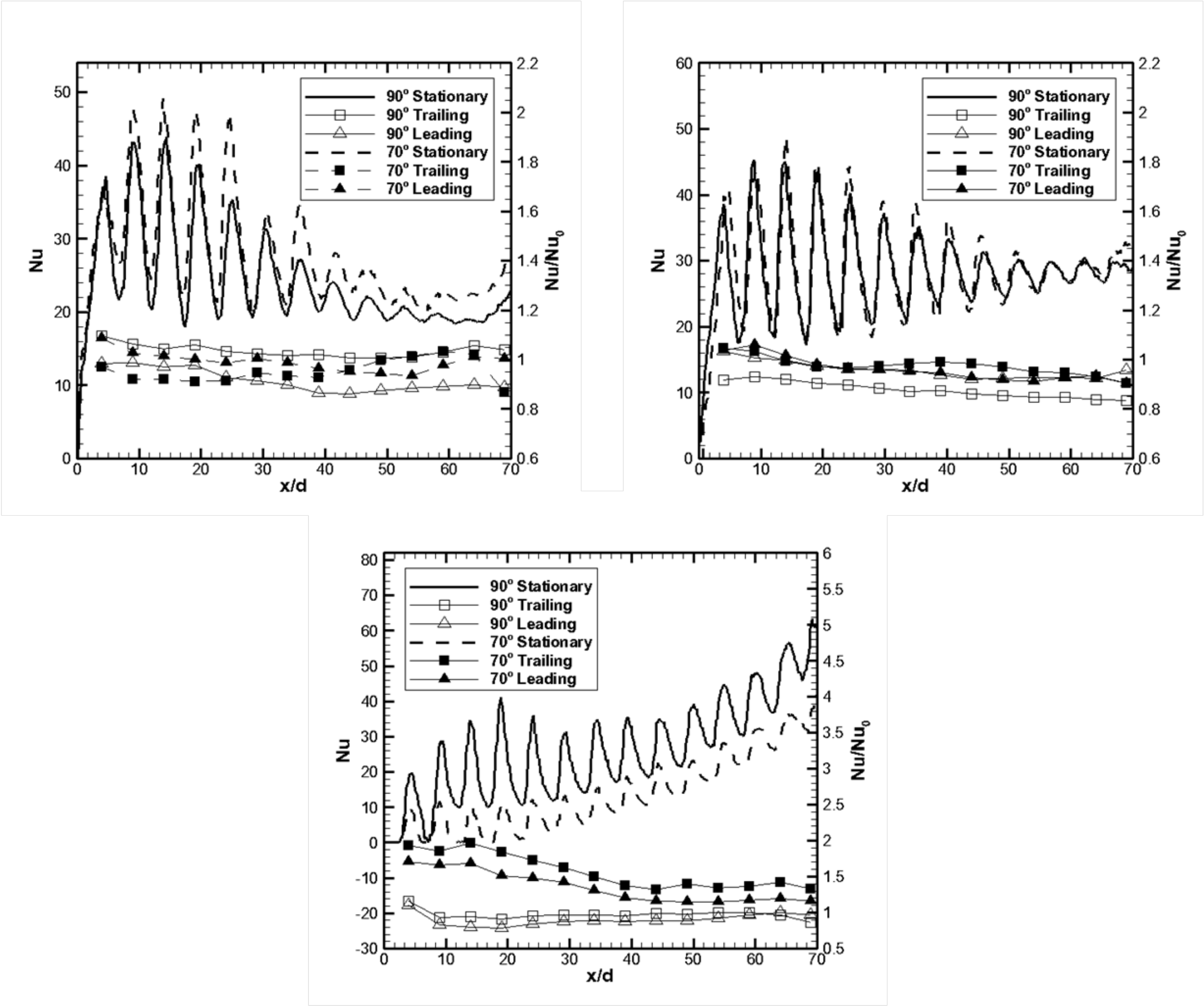

Figure 8.7: Comparative results between the 90° and 70° cases for H/d=5 (Top left), H/d=3 (Top right), and H/d=1 (Bottom).

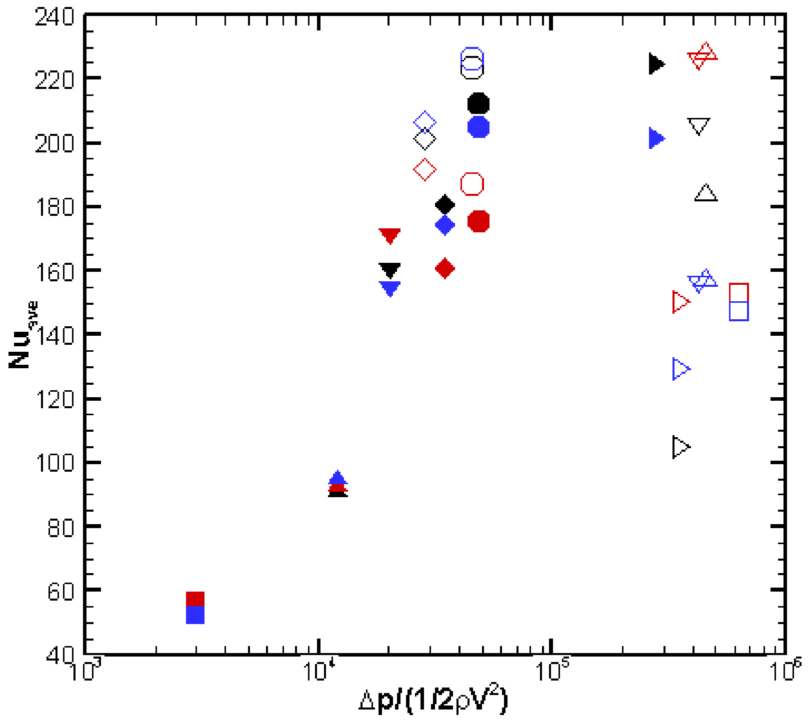

(a) Average Results

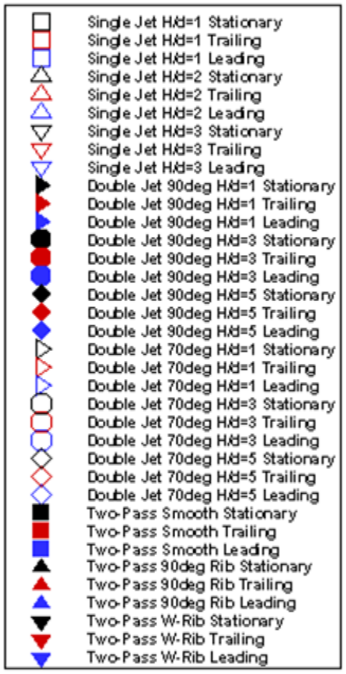

(b) Legend

Figure 8.8: Average Nu compared to Re for Ribbed and Jet Impingement cases.

# 9. Heat Transfer Enhancement in Narrow Diverging Channels

The current study focuses on heat transfer enhancement geometries in a narrow diverging channel. Different rib geometries and concavity geometries are evaluated in terms of overall heat transfer enhancement and pressure drop at a single channel flow Reynolds number of 28,000.

## 9.1 Test Section

Figure 9.1 shows the test section geometry. The channel is diverging. The channel height (H) in the transverse direction is fixed at 0.635 cm, whereas the channel increases in area in the spanwise direction. Dimensions are given in Table 9.1. The rib turbulators are made of thin-gage stainless steel wire and are glued to the test surface after painting the surface with liquid crystals.

Figure 9.2 shows three different rib configurations that are studied for heat transfer enhancement. The rib height and pitch for these configurations are identical. The three rib configurations are 90° ribs, 60° ribs and 45° V ribs.

Figure 9.3 shows the dimple configurations. Dimensions of the patterns and dimples used are located in Tab. 9.3. All configurations use hemispherical dimples. The dimples are machined on the test surfaces using a milling machine and then polished to provide light transmissivity. The liquid crystal is painted on top of the dimples and then the color change was measured from the outside looking into the backside of the dimples. Results from contour plots show no loss of data due to the machined features. The effect dimple depth is studied for the same

Table 9.1: Dimensions of the test section as shown in Fig. 9.1

| | |
|---|---|
| Height, H(cm) | 0.635 |
| L/H | 30 |
| Inlet Width/Height, $w_{in}$/H | 3 |
| Outlet Width/Height, $w_{out}$/H | 4.57 |
| Degree of Expansion, $\theta$(deg) | 3 |

dimple diameter, cases 3 and 4. The inline dimples of cases 3 and 4 are closer together than the pattern used in case 2.

Table 9.2: Dimensions used for rib configurations.

| | |
|---|---|
| Rib Height, e(mm) | 0.735 |
| Entrance Length, $L_e$(cm) | 3.493 |
| Pitch, P(cm) | 0.9525 |
| Rib Angle (deg) | 60 |
| V Angle (deg) | 45 |
| Pitch/Rib Height (P/e) | 12.5 |
| e/H (blockage ratio) | 0.12 |

Table 9.3: Pattern dimensions for the five dimple cases studied.

| Case | x/d | y/d | d/D | $L_e$/d |
|---|---|---|---|---|
| 1 | 5 | 1.83 | 4.5 | 9 |
| 2 | 1.5 | 2.75 | 3.0 | 9 |
| 3 | 1.75 | 1.31 | 5.0 | 9 |
| 3 | 1.75 | 1.31 | 10 | 9 |

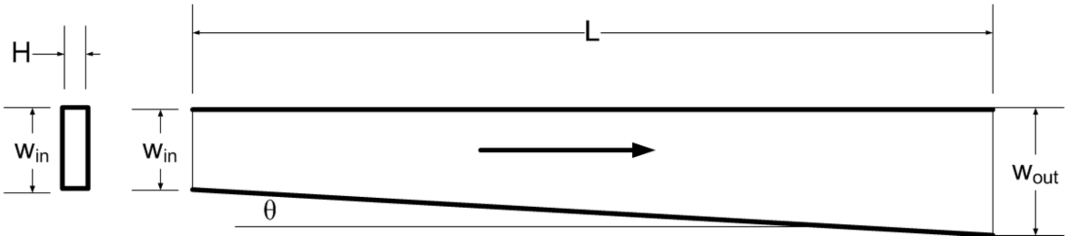

Figure 9.1: Test section geometry

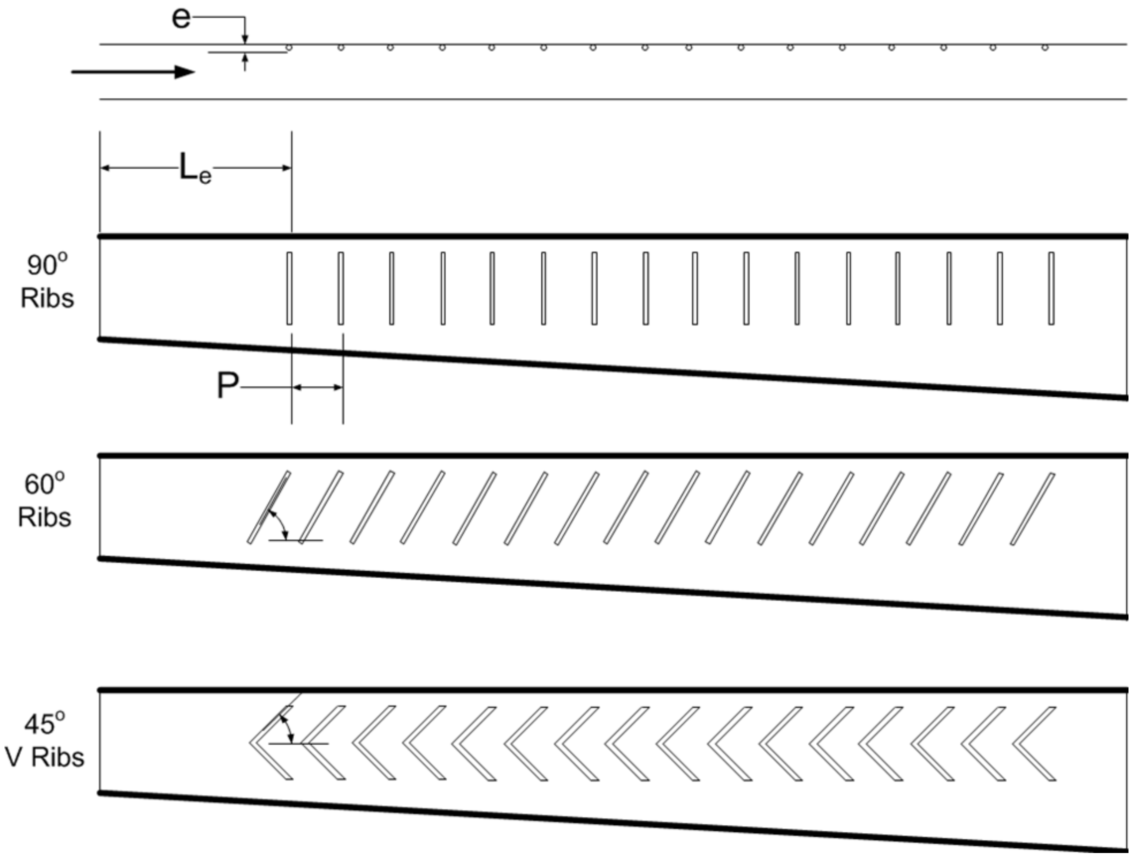

Figure 9.2: Rib turbulator geometries.

## 9.2 Results and Discussion

All the experiments are performed at a channel inlet Reynolds number of 28,000 based on inlet hydraulic diameter. First, the baseline is calculated. The baseline results are used for comparison of all proceeding heat transfer enhancement geometries.

Figure 9.4 presents the baseline heat transfer for a smooth channel. The heat transfer is significantly higher in the entrance region due to strong acceleration of flow into the narrow channel from the plenum. As the flow develops into the channel, the heat transfer drops rapidly and becomes non-uniform. This geometry is the baseline case and new geometries that are studied should provide higher heat transfer than this baseline case. The overall

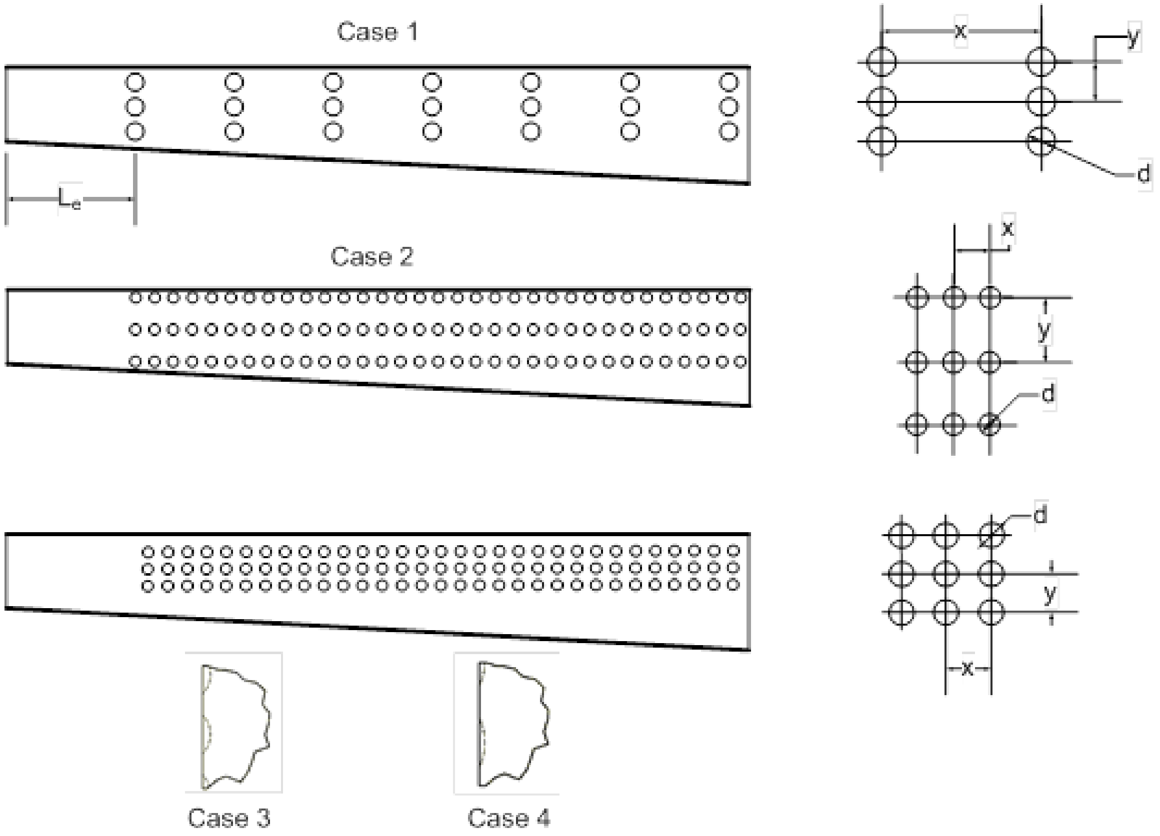

Figure 9.3: Dimple configurations used for testing.

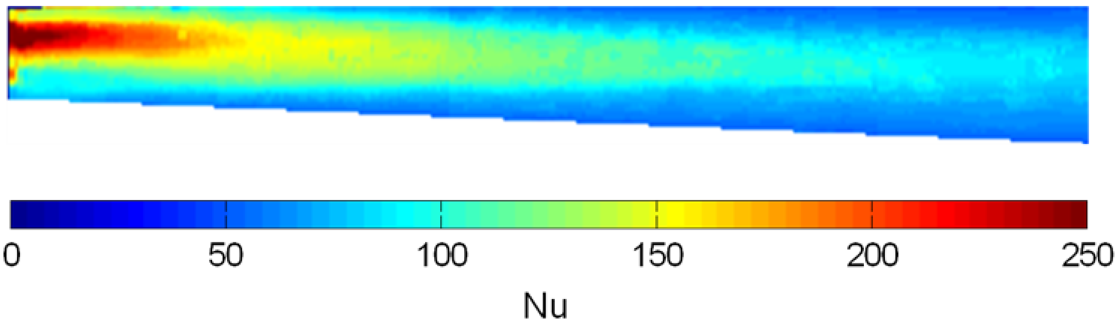

Figure 9.4: Detailed Nu distributions for baseline smooth surface.

average Nu for the baseline based on the inlet hydraulic diameter is measured to be $Nu_o$= 34.25. The smooth tube correlation (based on Dittus-Boelter) for the Nu based on inlet hydraulic diameter provides similar levels. However, in our study, the baseline is lower as the flow decelerates inside the diverging channel and reduces overall heat transfer.

### 9.2.1 Rib Turbulated Geometry

Figure 9.5 (top three) presents the heat transfer enhancement ratio comparing each of the rib cases with the baseline case. All three cases with ribs do not lose any major regions of data due to the presence of ribs on the test surface. For the 90° rib case, Nu is enhanced as is typical for orthogonal ribs to the flow shown by previous studies. The flow separates at the downstream end of each rib and reattaches in the middle of the pitch of the ribs and enhances heat transfer coefficients. Noticeable enhancements are present at the corners of the rib due to vorticity production. Vortices are created because the rib does not span the entire width of the channel causing accelerated flow in the narrow regions along the edges. A small separation zone is upstream of the ribs. As the channel increases in size, the enhancement factor increases downstream, which is expected as heat transfer enhancement is higher at lower velocities. The entrance region is almost unaffected by the presence of the downstream ribs, where $Nu/Nu_o$ at the entrance which is approximately 1.0.

For the 60° rib case, heat transfer enhancement is along the rib direction going from the angled wall to the straight wall of the channel. The enhancement level is similar for all ribs along the channel length. Mild enhancement is present in the entrance region due to the downstream ribs. Enhancement levels are clearly superior compared to the 90° rib case. The trend is similar to earlier studies. However, the enhancement is always limited to the region at the beginning of the rib along the angled wall. There is very little enhancement along the straight wall.

For the 45° V rib case, heat transfer enhancement levels are significantly higher than that for the 90° rib case and comparable to the 60° rib case. However, the enhancement region is much larger for the 45° V rib case. There is more uniform enhancement in the spanwise direction compared to the 60° rib case. Enhancement levels increase as the flow decelerates downstream. Overall averages show V rib provides higher and more uniform enhancement than the other cases.

### 9.2.2 Dimpled Channel Geometry

Figure 9.5 (4th and 5th from the top) presents the Nu ratios for three dimpled configurations shown in Fig. 9.3. Contour plots do not show any loss of data inside or around the dimples due to machining. For case 1, the enhancement is much higher for the row of dimples along the centerline of the channel. Clear enhancement is evident downstream of the dimples. However, the dimples are not clustered close enough to cause additional secondary enhancement from the downstream dimples. The enhancement decreases for the downstream dimples. For case 2, the enhancement is significantly higher along the centerline dimples. In this case, the dimples are closer together, therefore, affected by upstream dimples. Overall enhancement for all the dimple cases is much lower than for the rib turbulator cases.

### 9.2.3 Effect of Dimple Depth

Figure 9.5 (6th and 7th result from top) presents the detailed Nu ratio for cases shown in Fig. 9.3 . The dimples are closely packed and are in-line with each other in three rows. Enhancement is higher than cases shown in Fig. 9.5 (4th and 5th) due to the close packing. The decrease in depth from 0.0635 cm to 0.03175 cm reduced heat transfer enhancement due to smaller disturbance to the boundary layer. It appears that there is an optimum depth for the dimples at around 0.0635 0.085 cm. The results shown in Fig. 9.5 (cases 3 and 4) are for dimples on only one sidewall. Dimples on both side walls enhance heat transfer even further shown in Fig. 9.6.

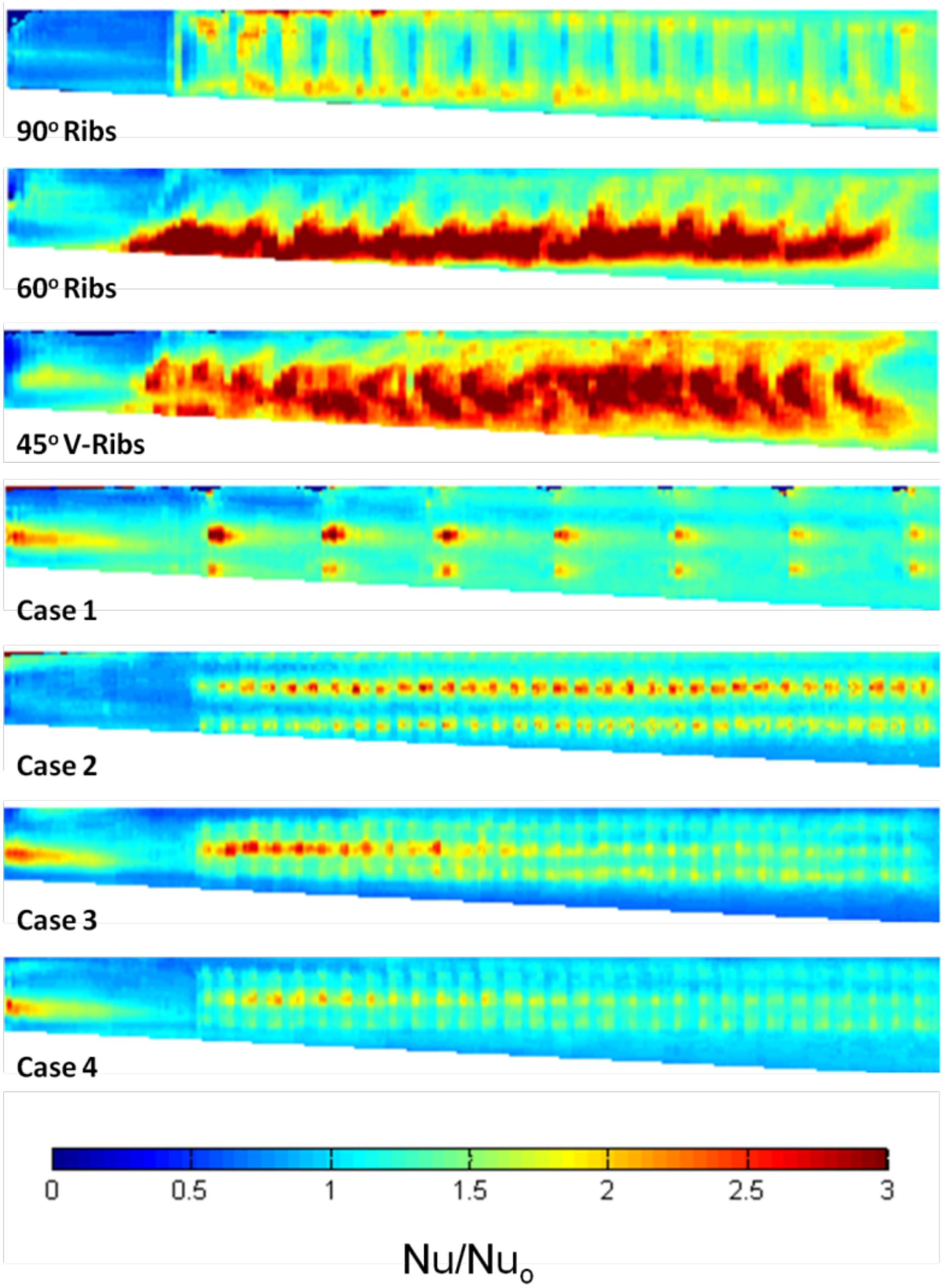

Figure 9.5: Detailed heat transfer results for ribs and dimples. (From top to bottom) 90° ribs, 60° ribs, 45° V-ribs, case 1, case 2, case 3, and case 4.

### 9.2.4 Pressure Drop Measurements

Overall pressure drop measurements are for all geometries. Pressure taps are placed in the plenum and the difference between ambient and the plenum pressure is calculated. The pressure drop (ΔP) is normalized by the pressure drop obtained for the baseline smooth case ($\Delta P_o$). All of the cases, including the baseline case, have the entrance and exit losses factored in the measurements, it is believed that the comparative results will show similar trends as the pressure drop for only the transport augmenting features.

### 9.2.5 Overall Performance Results

Figure 9.6 presents the overall averaged heat transfer coefficient ratios plotted against the overall pressure drop ratio for each case. Nu ratio for the V ribs is the highest but also has the highest pressure drop. The rib turbulated channels provide higher heat transfer coefficients with a higher pressure drop cost. Packing more dimples improves heat transfer enhancement without costing too much on pressure drop as is seen for the 0.0635 cm dimple cases compared to Cases 1 and 2.

Table 9.4 presents the overall results for all the geometries. In addition to overall heat transfer coefficient ratios and pressure drop ratios, an overall performance parameter is presented. The Performance Enhancement Factor (PEF) is used for heat exchanger design [54] and is defined in Eqn. (1.6).

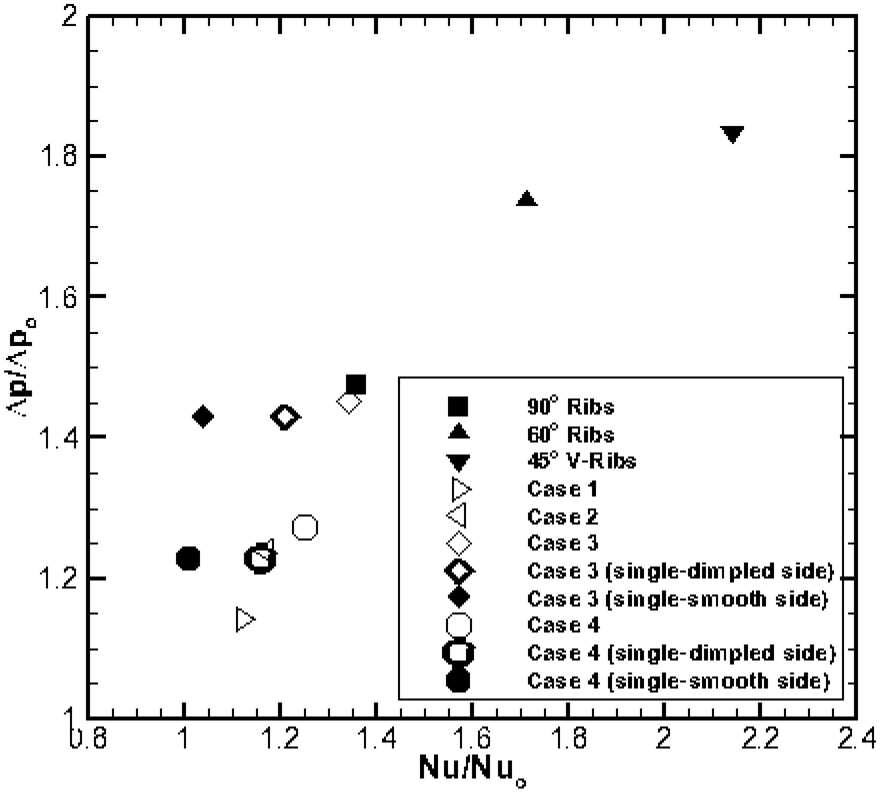

Figure 9.6: Comparing overall heat transfer ratios with overall pressure drop ratio for all cases (single sided only).

## 9.3 Conclusions

Detailed heat transfer measurements are presented for diverging channels with different enhancement geometry treatments. A transient liquid crystal measurement technique is used to obtain the detailed 2-D surface measurements. The main conclusions for the study are:

1. Rib turbulators enhance heat transfer significantly compared to other enhancement features but also cause higher pressure drop. The V rib geometry provides the highest

Table 9.4: Overall average heat transfer and pressure drop results.

| | Nu/$Nu_o$ | $\Delta p/\Delta p_o$ | PEF |
|---|---|---|---|
| Ribs | | | |
| 60° Ribs (single sided) | 1.71 | 1.74 | 1.42 |
| 90° Ribs (single sided) | 1.36 | 1.48 | 1.19 |
| V Ribs (single sided) | 2.14 | 1.83 | 1.75 |
| Dimples | | | |
| Case 1 (double sided) | 1.12 | 1.14 | 1.07 |
| Case 2 (double sided) | 1.17 | 1.24 | 1.09 |
| Case 3 (double sided) | 1.34 | 1.45 | 1.18 |
| Case 3 (single sided-dimple side) | 1.21 | 1.43 | 1.07 |
| Case 3 (single sided-smooth side) | 1.04 | 1.43 | 0.92 |
| Case 4 (double sided) | 1.25 | 1.27 | 1.15 |
| Case 4 (single sided-dimple side) | 1.16 | 1.23 | 1.08 |
| Case 4 (single sided-smooth side) | 1.01 | 1.23 | 0.944 |

heat transfer enhancement ratios but also causes the highest pressure drop.

2. Dimples cause local enhancement and increase heat transfer in and around the dimples. Close packing of the dimples provides further enhancement due to secondary enhancement from the upstream and downstream dimple interactions.

3. Dimple depth effect indicates an optimum depth value around d/D of 3-5.

# 10. Radially Outward Ducts at High Rotation Speed

The last study of this dissertation uses a modified setup of the rotating rig. The rig is modified to reach higher rotational speeds than any previous study of this dissertation. The purpose of this study is to analyse six radially outward coolant channels for generator rotor windings. As the channels model the real geometry of an existing machine, realistic geometric features are captured. Complex geometric features would not be manufacturable without the aid of modern manufacturing techniques, i.e. rapid prototyping. This chapter discusses the modified test setup, the test section, flow conditions, and results for both stationary and rotating conditions

## 10.1 Modified Test Setup

The difference between the setup for the rotating rig used in the previous chapters and the current chapter is that the drive shaft is horizontal instead of vertical. Figure 10.1 shows a photograph of the rig. With this setup, concrete anchors fasten the rig to the ground. Vibration absorbers dampen the vibrations from rotation. Quarter inch aluminum shielding is bolted all around the structure to contain any flying parts to due failure. Figure 10.2 shows the test section mounted into the new horizontal orientation. The parts are the same as the original setup, just horizontally oriented. The control of the rotating rig is through LABVIEW. A diagram of the rig system and control is given in Fig. 10.3. The system uses the cold fluid injection method, as previously performed. Nitrogen gas is vented into the coolant path to prepare the test. The nitrogen vents to atmosphere at the "Atmosphere/Test

Section Flow Swith", as shown in Fig. 10.3. For the test, the "N2/Air Flow Switch" and "Atmosphere/Test Section Flow Switch" are changed to allow air from the compressor to enter the test section. The control station turns on the "Solenoid Valve Flow Switch" to allow air into the test section. The control station monitors the flow rate of air with pressure transducers measuring the pressure drop across the orifice meter. A Variable Frequency Drive (VFD) is controlled at the control station, allowing motor speed to be set. Signals from the tachometer are sent back to the control station to monitor the rotational speed. A thermocouple module is included in the control station, to monitor and capture temperature signals. A light bulb inside the rotating rig is also controlled. This bulb serves two purposes.

The interior of the rig is dark due to the enclosure. A bulb is mounted inside to provide light when working on the rig or test section. The other purpose of the light bulb is to que the video camera when the test begins. The video camera is untethered, so there is not a direct means of knowing, in the video, the official start of the test. The control software is designed to initiate everything at once. Simultaneously, the solenoid valves are switched, temperature data is recorded, and the light bulb is turned off. During the data analysis procedure, when the bulb turns off, the video is trimmed and begins from this point as time, t=0 s.

The camera mount is altered compared to the previous setup, as shown in Fig. 10.4. For this study, t-slotted aluminum extrusions are used as the camera support. The aluminum is light weight and high strength. The t-slot feature allows much freedom in the positioning of the camera. For the setup shown in Fig. 10.4, the camera has three degrees-of-freedom. Three degrees of freedom is convenient, as camera placement is flexible. This camera setup is used in the *Experimental Heat Transfer Rigs* chapter, *Camera Mounting* subsubsection.

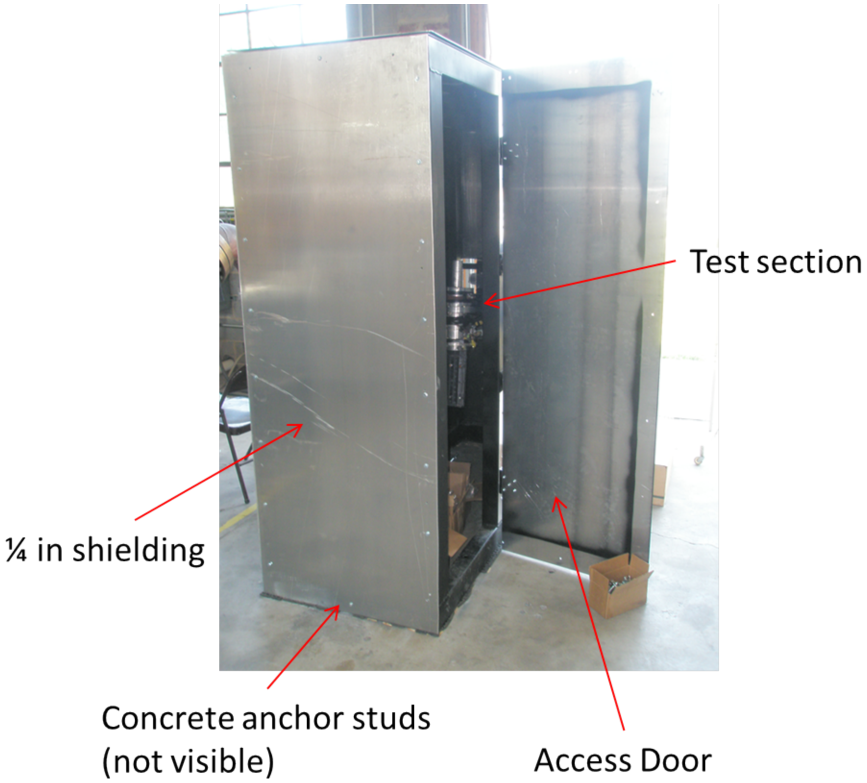

Figure 10.1: Rotating rig tipped on its side for a horizontal drive shaft orientation.

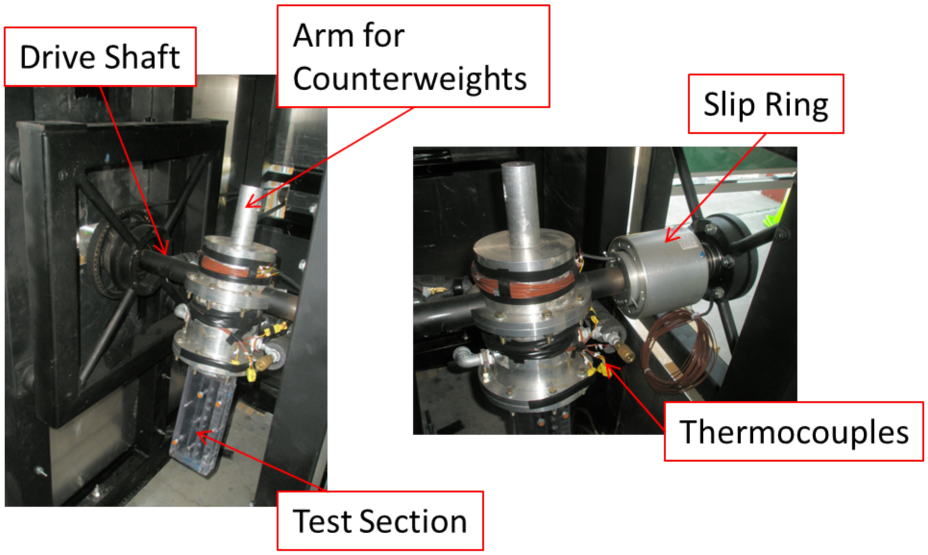

Figure 10.2: Images of test section and support for horizontally oriented rotation.

## 10.2 Test Section

The test section is the same from the *Experimental Heat Transfer Rigs* chapter, *Sample Test Section* subsubsection, as shown in Fig. 10.5. There are six radially outward channels and one inlet. Each channel has triangular grooves, as shown in Fig. 10.6 and Fig. 10.7. Table 10.1 shows the sizing used in the radial channels and the size of the plenum channel.

Table 10.1: Radial and plenum channel sizing.

| | |
|---|---|
| $W_D/H_D$ | 11.5 |
| $P/H_D$ | 3.31 |
| $r_D/H_D$ | 0.5 |
| $W_P/H_D$ | 13.3 |
| $H_P/H_D$ | 12.7 |
| $H_g/H_D$ | 0.8 |
| $d_g/H_D$ | 0.3 |

## 10.3 Flow Conditions

Three Re conditions are explored for the stationary setup: 7000, 14000, and 21000. For the rotating condition, Re=10000 is used. The test section rotates at 750 rpm, creating Ro=0.031. Compared to previous rotating channel studies ([4],[5],[15],[37] and others) Ro=0.031 is relatively low. According to general trends from previous studies, both the leading and trailing side heat transfer should not deviate much from the stationary case at Ro=0.031. For each Re case, pressure measurements are taken in each channel. The reported Re is the average based on the total inlet flowrate. Specific flow rates in each channel is calculated by taking the pressure drop across each channel.

## 10.4 Results and Discussion

Pressure drop and heat transfer coefficients are measured in each channel. Pressure drop measurements allow the flow rate in each channel to be calculated for each average Re case studied. Pressure measurements are only measured for the stationary cases, as a method for taking pressure measurements in rotation is unavailable at this time. Heat transfer measurements are taken in both stationary and rotating conditions. Detailed plots are provided, as well as spanwise averaged results along the length of the channels.

### 10.4.1 Flow Measurements

Static pressure measurements are taken at the inlet to each channel for the three Re cases. Air exits the channels to atmosphere, so pressure drop is respect to atmospheric pressure. Tables 10.2a, 10.2b, and 10.2c lists the static pressure drop for each channel for Re=7000, 14000, and 21000, respectively. Table 10.2 lists the percent mass flow of coolant in each channel, volumetric flow rate, in cubic feet per minute (cfm) for each channel, and Re in each channel. For all three Re cases, channel 1 receives the least amount of coolant. The reduced flow in channel 1 may occur because the coolant experiences a sudden expansion as it exits the round hose and enters the rectangular plenum channel, as shown in Fig. 10.5. The expanding jet may cause the coolant to jump past the 1st channel just enough cause a reduction.

### 10.4.2 Stationary Heat Transfer Results

Figure 10.8a shows results for Re=7000, Fig. 10.8b shows results for Re=14000, and Fig. 10.8c shows results for Re=21000. For all of the cases studied, channel 1 & 6 have the least

Table 10.2: Flow measurements for each channel for each flow condition and average Nu compared to Dittus-Boelter.

| **Ch #** | **P$_s$(inH$_2$O)** | **%flow** | **cfm/ch** | **Re/ch** | **Nu$_{DB}$** | **Nu$_{avg}$/Nu$_{DB}$** |
|---|---|---|---|---|---|---|
| **1** | 3.0 | 14.86 | 3.40E+02 | 5.78E+03 | 20.94 | 2.564 |
| **2** | 3.8 | 16.73 | 3.83E+02 | 6.51E+03 | 23.02 | 2.658 |
| **3** | 3.8 | 16.73 | 3.83E+02 | 6.51E+03 | 23.02 | 2.763 |
| **4** | 4.0 | 17.16 | 3.93E+02 | 6.67E+03 | 23.50 | 2.183 |
| **5** | 3.9 | 16.94 | 3.88E+02 | 6.59E+03 | 23.26 | 2.093 |
| **6** | 4.2 | 17.58 | 4.02E+02 | 6.84E+03 | 23.96 | 2.241 |

(a) Re=7000

| **Ch #** | **P$_s$(inH$_2$O)** | **%flow** | **cfm/ch** | **Re/ch** | **Nu$_{DB}$** | **Nu$_{avg}$/Nu$_{DB}$** |
|---|---|---|---|---|---|---|
| **1** | 10.5 | 14.38 | 6.89E+00 | 1.17E+04 | 36.82 | 2.422 |
| **2** | 14.5 | 16.90 | 8.09E+00 | 1.38E+04 | 41.90 | 2.912 |
| **3** | 15.0 | 17.19 | 8.23E+00 | 1.40E+04 | 42.47 | 2.807 |
| **4** | 15.0 | 17.19 | 8.23E+00 | 1.40E+04 | 42.47 | 2.510 |
| **5** | 15.0 | 17.19 | 8.23E+00 | 1.40E+04 | 42.47 | 2.324 |
| **6** | 14.9 | 17.14 | 8.20E+00 | 1.39E+04 | 42.36 | 2.104 |

(b) Re=14000

| **Ch #** | **P$_s$(inH$_2$O)** | **%flow** | **cfm/ch** | **Re/ch** | **Nu$_{DB}$** | **Nu$_{avg}$/Nu$_{DB}$** |
|---|---|---|---|---|---|---|
| **1** | 26.7 | 14.76 | 1.07E+01 | 1.81E+04 | 52.30 | 2.692 |
| **2** | 34.3 | 16.73 | 1.21E+01 | 2.06E+04 | 57.81 | 2.847 |
| **3** | 36.0 | 17.14 | 1.24E+01 | 2.11E+04 | 58.94 | 2.589 |
| **4** | 36.0 | 17.14 | 1.24E+01 | 2.11E+04 | 58.94 | 2.219 |
| **5** | 36.0 | 17.14 | 1.24E+01 | 2.11E+04 | 58.94 | 2.312 |
| **6** | 35.8 | 17.09 | 1.24E+01 | 2.10E+04 | 58.81 | 2.131 |

(c) Re=21000

symmetric Nu distributions than the remaining channels. Channel 1 is closest to the inlet. The inlet has an expanding jet effect which may partially skip over the inlet to the channel 1, in addition to a $90^{/}circ$ turn from the plenum channel. This causes the coolant to hug the right hand wall, which shows up as the higher Nu region compared to that on the left hand wall. As the flow develops, the Nu distribution evens out along the entire span of the wall. Channel six is next to the end cap of the plenum channel. The plenum channel termination causes a recirculation region just outside the inlet to channel 6. This recirculation region causes the coolant to enter channel 6 in a non-symmetric manner, similar to that of channel

1. The flow, however, hugs the left hand wall, as the recirculation region at the inlet partially blocks the right hand side inlet to channel 6. As the flow develops, the heat transfer along the spans evens out. The interior channels, 2-5, experiences relatively even flow distribution from inlet to outlet.

Figure 10.8d shows the spanwise average along the length of channel 2 for all Re. Channel 2 is chosen as an example, as similar distributions are given in the remaining channels. For all cases studied, the effects of the grooves are present. As the groove expands out, a recirculation region occurs. This recirculation region is identified by the low heat transfer region, as noted in Fig. 10.8d. As the groove abruptly terminates, turbulence increases causing a spike in Nu. The Nu steadily decreases after the groove, then the boundary layer restarts again after each groove. Table 10.2 also shows the average Nu for each flow condition and channel compared to the calculated $\mathrm{Nu}_{DB}$. Nu ratios range from 2-3, showing considerable enhancements in the channels due to the triangular grooves.

### 10.4.3 Rotating Heat Transfer Results

Results are located in Figs. 10.9a and 10.9b. Because Ro=0.03, the leading and trailing sides vary little from each other. The average Nu from Fig. 10.9a is 70, while the average from Fig. 10.9b is 66. The percent difference between the results is 6%, which is well within the experimental uncertainty. Figure 10.10 shows spanwise average line plots. The peaks and troughs from the grooves are both evident in the results, proving the camera is able to capture detailed effects at high rotational speeds. The spanwise averages of both the leading and trailing sides deviate very little from each other, reinforcing the prediction that low Ro will not affect the cooling channel.

## 10.5 Conclusions

A series of radially outward coolant channels are studied in stationary and rotating conditions. These channels possess triangular grooves which enhance the heat transfer inside the channel. The channels are approximately 25D, reaching a fully developed flow condition. Comparing Nu for each channel and each flow condition, the triangular grooves enhance the heat transfer, on average, by a factor of 2 compared to Dittus-Boelter. The effects of the grooves are evident in the spanwise average results, with distinguished peaks and troughs. The AR of the channels are approximately 11.5. At a rotational speed of 500 rpm, Ro=0.03. Ro=0.03 is relatively low and previous rotating channel studies show minimal effects of rotation at this condition. This study confirms this notion, by showing little to no variation in heat transfer between the leading and trailing sides for Re=10000. Major modifications to the rig allows high rotational speed measurements. All equipment, including the camera, function as designed and data capture is capable.

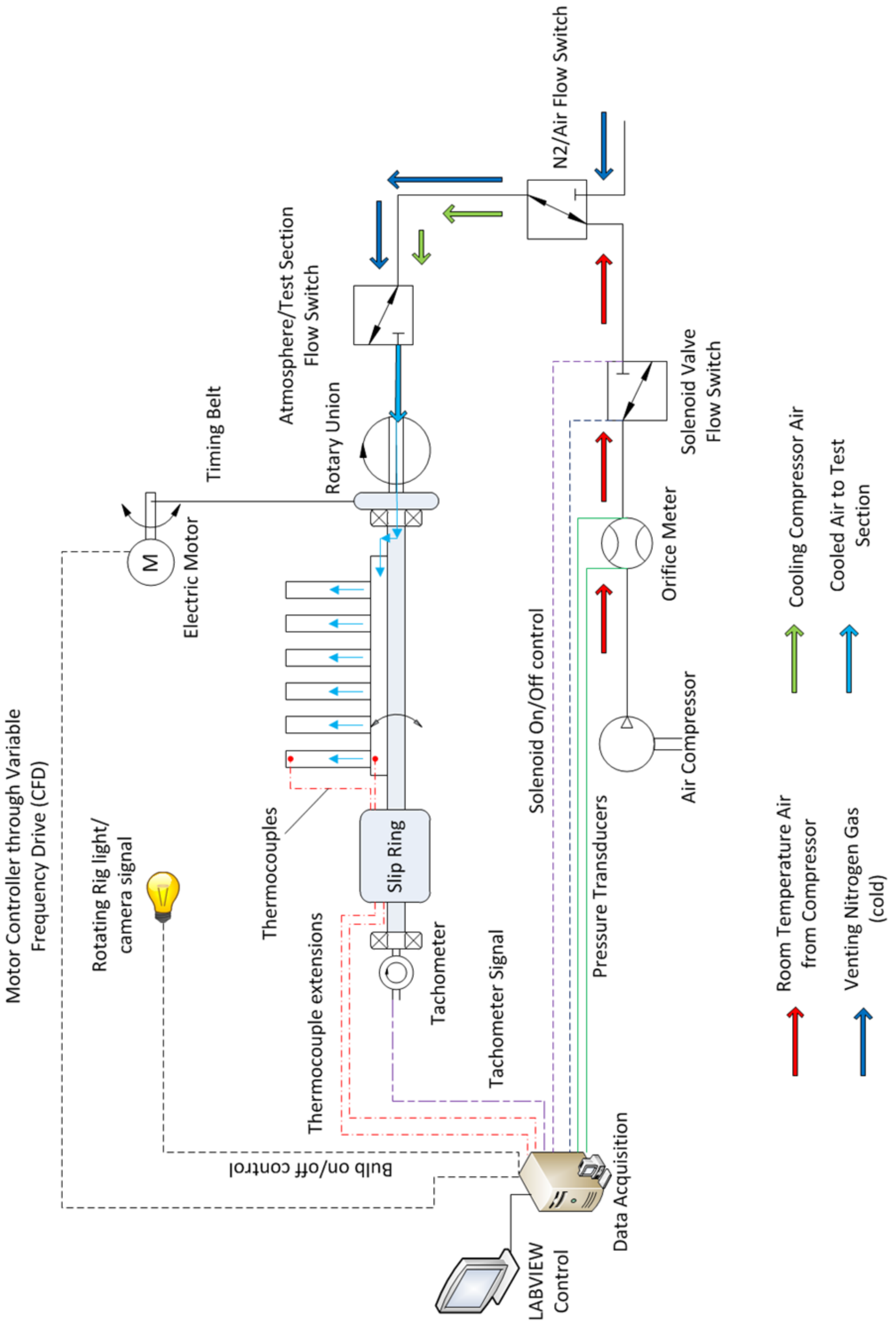

Figure 10.3: Rotating rig and rig control

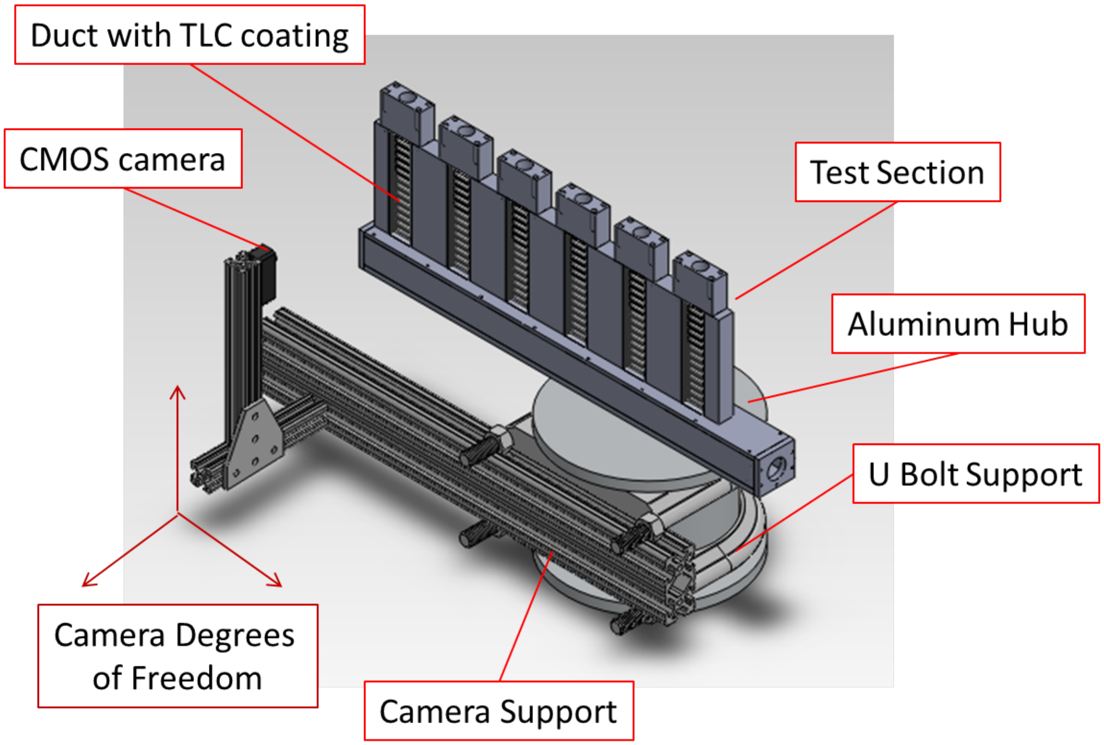

Figure 10.4: Camera mount used with three degrees of freedom.

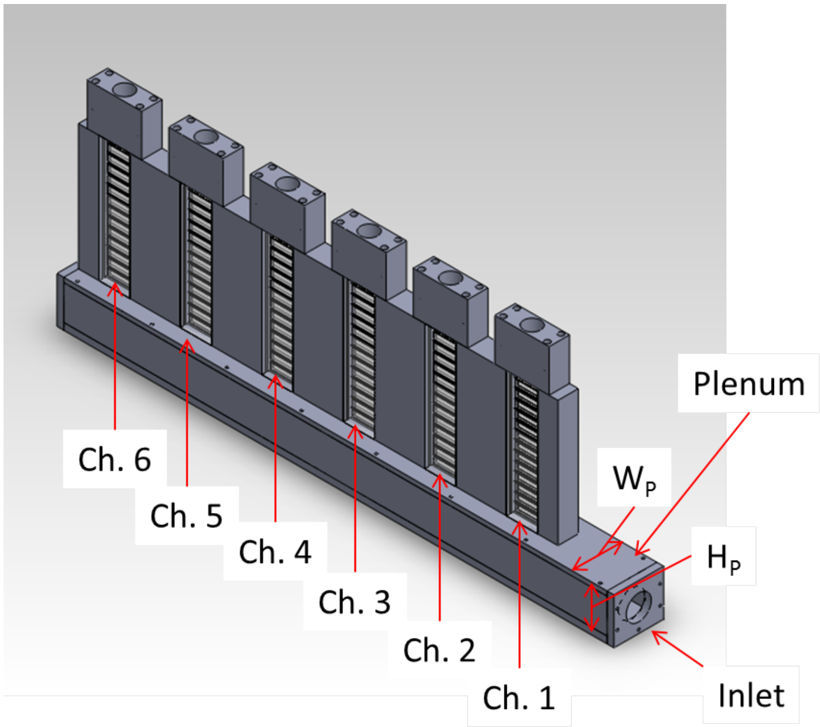

Figure 10.5: Test section used with six radially outward channels.

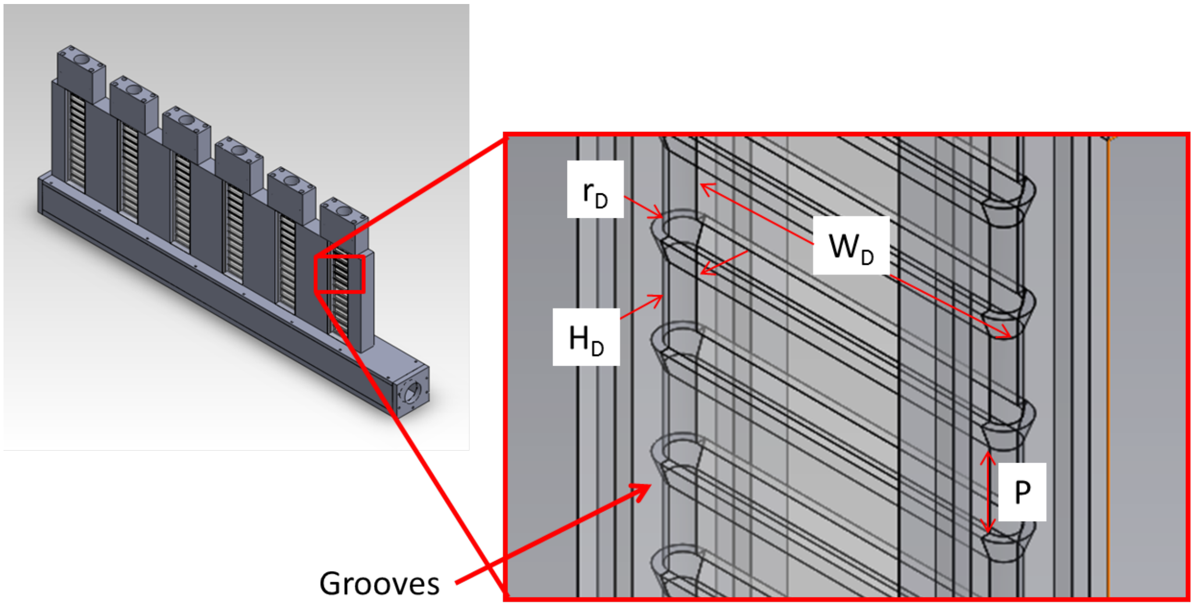

Figure 10.6: Channel with triangular grooves and nomenclature.

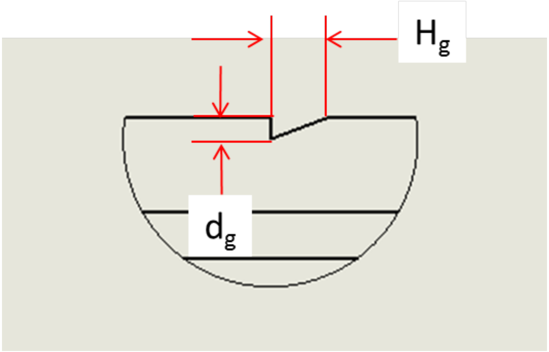

Figure 10.7: Triangular grooves.

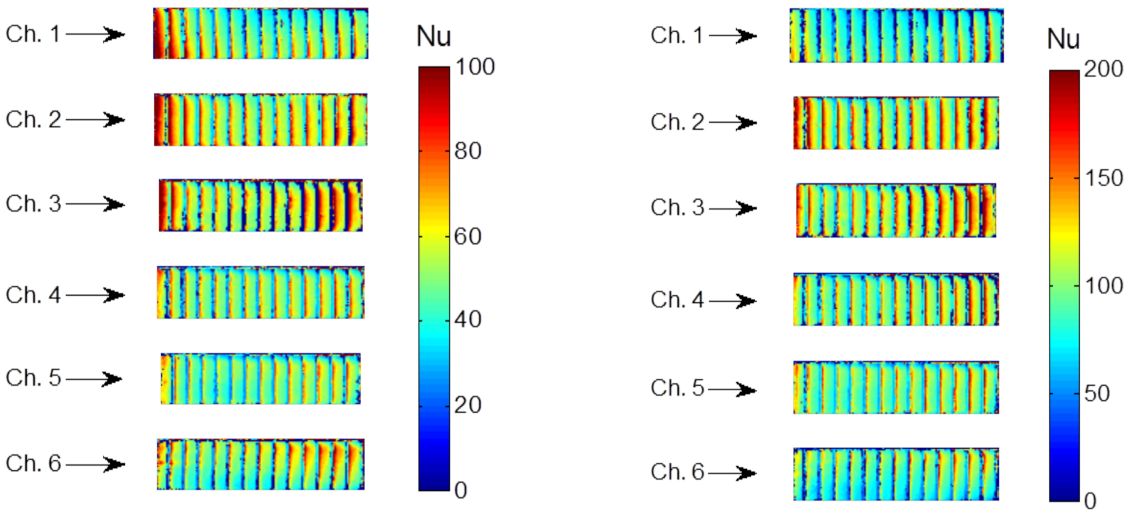

(a) Re=7000

(b) Re=14000

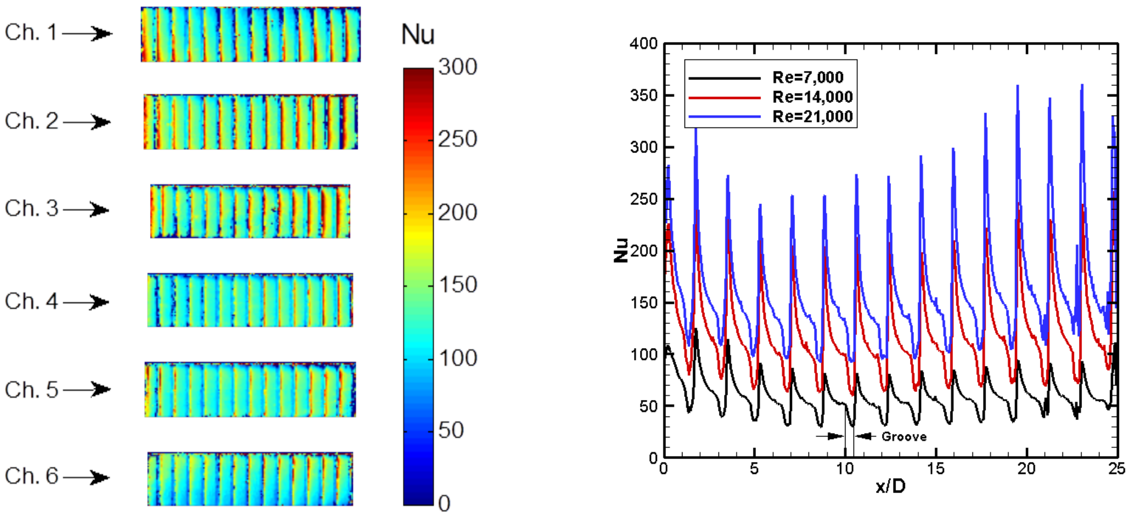

(c) Re=21000

(d) Sample spanwise average line plot of Ch. 2.

Figure 10.8: Detailed stationary results.

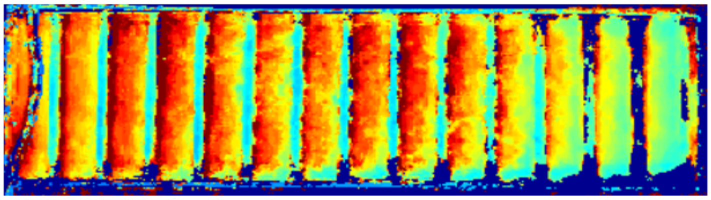

(a) Leading Side

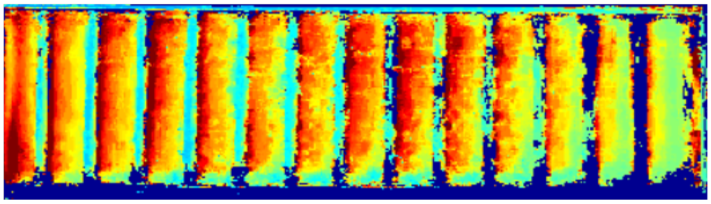

(b) Trailing Side

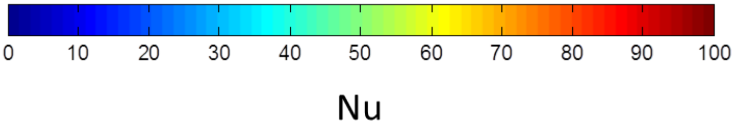

Figure 10.9: Rotating Results for Re=10,000 and 500 rpm.

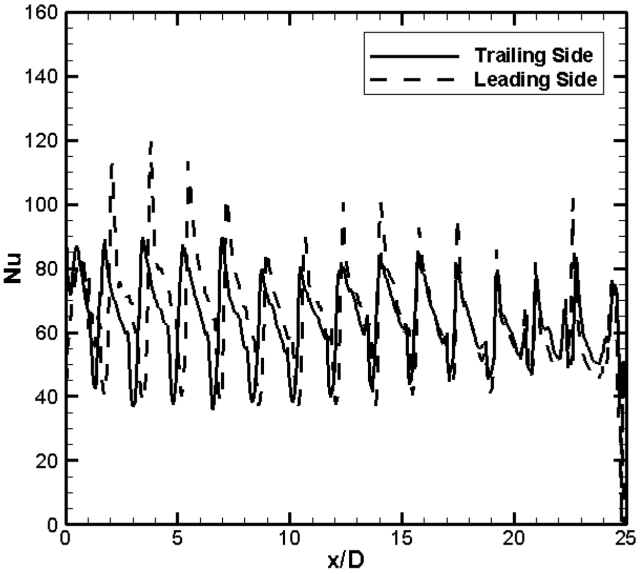

Figure 10.10: Spanwise average line plots.

# 11. Research Conclusions

A rotating experimental rig was designed and constructed to perform rotating channel heat transfer studies. A detailed stress analysis was performed to ensure safe operation of the rig. This was critical, as the sizeable mass of the test section and counter weights at speeds in excess of 500 rpm generates devastating power. Simple, but conservative mechanical design techniques ensured the safe operation. A thorough understanding of the experimental procedure was outlined for the transient liquid crystal technique. Obstacles to the experimental method such as proper lighting on a rotating frame was addressed and solved. Data reduction challenges such as eliminating the black hue contamination in calculation were discovered and resolved. High rotational speeds cause high g-forces on the camera gathering data. An epoxy potting compound was used to solidify the camera's internal components, making it immune to high g-forces. Several studies are performed on the rotating rig, many are similar to studies by other researchers. Experimental results show good alignment with previous studies, validating the experimental setup. Two-pass channel studies with smooth, 90° ribs and, W-shaped ribs were performed to validate the early experimental setup. This is the first study to show heat transfer patterns of W-shaped ribs. A large diameter channel study was created to examine higher rotation number systems without significantly higher rotational speeds, as performed on the smaller two-pass channel. Results show that the entrance effects are significant enough to reduce the effectiveness of 90° ribs and W/M-shaped ribs of 45° and 30° angles. This is the first study to show the heat transfer patterns created by the W/M-shaped ribs at different steepness angles. Single and double row impingement channels were studied at H/d values of 1,2,3, and 5. Results show significant changes in total heat transfer and heat transfer distributions between the varying H/d types. The rotational speeds examined show the resistance to rotational effects of the jet impingement cooling schemes. Jet impingement can achieve high heat transfer, some schemes achieving higher heat transfer than M-shaped ribs. However, associated pressure losses are significant with jet impingement. As H/d approaches 1, pressure losses increase significantly. For 90° orientation jets at H/d=1, total heat transfer is similar to H/d=3, however, the pressure losses do not warrant their use. For 70° orientation jets at H/d=1, pressure losses are high with no added value in heat transfer. The fewer the jets, the higher the pressure losses. Although less total mass flow of coolant passed through the single row of jets, non-dimensional pressure losses are considerably higher than the double row jet impingement studies. A study was performed on expanding ducts with ribs and dimples. Ribs were very effective in heat transfer augmentation, however, have significant pressure losses. Of the three rib types studied, 90°, 60°, and 45° V shaped ribs, the V shaped ribs perform the best. Of the dimple type studies, dimples that are grouped closer together and deeper into the surface outperform other configurations. Although the ribs have higher pressure losses, the hydraulic-thermal performance factor warrants their use; significant heat removed from the system for modest increases in the required pumping power. Improvements in the rig allowed very high speeds to be achieved. The design and physical effort put into the rotating rig has allowed many studies to be performed. The latest improvements will allow future operators the ability to reach higher and higher rotation numbers, which will aid in the validation of computational models for the gas turbine and generator industry which was previously unavailable.

# Nomenclature

| | |
|---|---|
| $\Delta$x | Camera distance to test section |
| $\Delta p$ | Pressure drop from inlet to outlet |
| $\Delta p_o$ | Pressure drop from inlet to outlet of channel without turbulators |
| $A_c$ | Cross sectional area |
| $a_c$ | Coriolis acceleration |
| AR | Aspect Ratio |
| B | Test section plate thickness |
| b | Cross sectional base length |
| BP | Buoyancy parameter |
| c | Cross sectional height length |
| cfm | Cubic feet per minute |
| D | Hydraulic diameter |
| $d_g$ | Depth of grooves |
| $d_j$ | Jet diameter |
| $D_{rod}$ | Hanging rod diameter |
| dF | Differential force contribution |
| dm | Differential mass contribution |

| | |
|---|---|
| dr | Differential radial coordinate |
| e | Rib height |
| e/H | Blockage ratio |
| Err | Error between estimated and measured wall temperature |
| F | Force |
| FOS | Factor of Safety |
| g | gravity |
| $G_c$ | Mass flux of crossflow coolant |
| $g_c$ | Gravitational constant for English system |
| $G_j$ | Mass flux of jet coolant |
| $Gr_D$ | Grashoff Number |
| H | Height of channel or distance from jet to target wall |
| h | Heat transfer coefficient |
| $H_g$ | Height of grooves |
| $H_{TS}$ | Viewable height of camera based on distance, $\Delta$x |
| $H/d_j$ | Non-dimensional jet-to-target wall distance |
| I | Second moment of area |
| k | Thermal conductivity |
| $k_f$ | Thermal conductivity of fluid |

| | |
|---|---|
| $k_w$ | Thermal conductivity of solid |
| L | Channel length |
| $L_e$ | Entrance length to dimples |
| M | Bending moment |
| Nu | Nusselt number |
| $Nu_o$ | Nusselt number of channel without turbulators |
| $Nu_{db}$ | Dittus-Boelter Nusselt number |
| P | Pitch, distance between ribs or jets |
| $P_s$ | Static pressure |
| Pr | Prandtl number |
| R | Rotating radius (distance to center of rotation) |
| r | Radial coordinate |
| $R_i$ | Inner Radial distance |
| $R_m$ | Mean rotating radius |
| $R_o$ | Outer Radial distance |
| Re | Reynolds number for internal flow |
| Ro | Rotation number |
| $S_p$ | Proof strength |
| t | time |

| | |
|---|---|
| $T_i$ | Initial wall temperature |
| $T_m$ | Mainstream or bulk fluid temperature |
| $T_m*$ | Non-dimensional mainstream/bulk fluid temperature |
| $T_w$ | Surface or wall temperature |
| $T_w*$ | Non-dimensional wall temperature |
| $T_{shear}$ | Shear stress of threads in aluminum hub |
| $T_{w,est}$ | Estimated wall temperature |
| T(0,t) | Temperature of solid at x=0 and time, t |
| T(x,t) | Temperature of solid at coordinate x into material and time, t |
| t* | Non-dimensional time |
| V | Particle/fluid velocity |
| $w_{in}$ | Inlet width of diverging channel |
| $w_{out}$ | Outlet width of diverging channel |
| $W_{TS}$ | Viewable width of camera based on distance, $\Delta$x |
| X | X coordinate |
| x | Distance into solid material |
| Y | Y coordinate |
| y | Outside edge-to-centroidal axis distance |
| Z | Z coordinate |

| | |
|---|---|
| $\alpha$ | Thermal diffusivity |
| $\beta$ | Degree of expansion for diverging channel |
| $\eta$ | Thermal-hydraulic performance |
| $\frac{\Delta\rho}{\rho}$ | Coolant-to-wall density ratio |
| $\gamma$ | Volumetric thermal expansion coefficient |
| $\nu$ | Kinematic Viscosity |
| $\rho$ | density of fluid or solid |
| $\sigma$ | Normal stress |
| $\tau$ | Non-dimensionalizing time constant |
| $\theta$ | Rib angle with respect to horizontal |
| $\vec{\omega}$ | Rotational velocity |
| $\sigma_b$ | Bending stress |

# References

[1] Johnston, J. P., Hanneen, R. M., and Lezius, D. K., 1972. "Effects of spanwise rotation on the structure of two-dimensional fully developed turbulent channel flow". *Cambridge Journal of Fluid Mechanics,* ***56***(3), pp. 533–557.

[2] Han, J. C., Dutta, S., and Ekkad, S. V., 2000. *Gas Turbine Heat Transfer and Cooling Technology.* Taylor and Francis, New York, NY.

[3] Han, J. C., Zhang, Y. M., and Kalkeuhler, K., 1993. "Uneven wall temperature effect on local heat transfer in a rotating two-pass square channel with smooth walls". *ASME Journal of Heat Transfer,* ***115***(4), pp. 912–920.

[4] Wagner, J. H., Johnson, B. V., and Kopper, F. C., 1991. "Heat transfer in rotating serpentine passages with smooth walls". *ASME Journal of Turbomachinery,* ***113***(3), pp. 321–330.

[5] Wagner, J. H., Johnson, B. V., and Graziani, R. A., 1992. "Heat transfer in rotating passages with trips normal to the flow". *ASME Journal of Turbomachinery,* ***113***(4), pp. 847–857.

[6] Taslim, M. E., Rahman, A., and Spring, S. D., 1991. "An experimental investigation of heat transfer coefficients in a spanwise rotating channel with two opposite rib-roughened walls". *ASME Journal of Turbomachinery,* ***113***(1), pp. 75–82.

[7] Parsons, J. A., Han, J. C., and Zhang, Y., 1994. "Wall heating effect on local heat transfer in a rotating two-pass square channel with 90 rib turbulators". *International Journal of Heat Transfer,* ***37***(9), pp. 1411–1420.

[8] Zhang, Y. M., Han, J. C., Parsons, J. A., and Lee, C. P., 1995. "Surface heating effect on local heat transfer in a rotating two-pass square channel with 60 deg angled rib turbulators". *ASME Journal of Turbomachinery,* ***117***(2), pp. 272–280.

[9] Johnson, B. V., Wagner, J. H., Steuber, G. D., and Yeh, F. C., 1994. "Heat transfer in rotating serpentine passages with selected model orientations for smooth or skewed trip walls". *ASME Journal of Heat Transfer,* ***116***(4), pp. 738–744.

[10] Taslim, M. E., Li, T., and Kercher, D. M., 1996. "Experimental heat transfer and friction in channels roughened with angled, v-shaped, and discrete ribs on two opposite walls". *ASME Journal of Turbomachinery,* ***118***(1), pp. 20–28.

[11] Lee, E., Wright, L. M., and Han, J. C., 2005. "Heat transfer in rotating rectangular channels with v-shaped and angled ribs". *AIAA Journal of Thermophysics and Heat Transfer,* ***19***(1), pp. 48–56.

[12] Wright, L. M., Fu, W.-L., and Han, J. C., 2004. "Thermal performance of angled, v-shaped, and w-shaped rib turbulators in rotating rectangular cooling channels (ar=4:1)". *ASME Journal of Turbomachinery,* ***126***(4), pp. 604–614.

[13] Griffith, T. S., Al-Hadhrami, L., and Han, J. C., 2003. "Heat transfer in rotating rectangular cooling channels (ar=4) with dimples". *ASME Journal of Turbomachinery,* ***125***(3), pp. 555–563.

[14] Kim, S., Lee, Y. J., Choi, E. Y., and Kwak, J. S., 2011. "Effect of dimple configuration on heat transfer coefficient in a rotating channel". *AIAA Journal of Thermophysics and Heat Transfer,* ***25***(1), pp. 165–172.

[15] Chang, S. W., Liou, T. M., Yang, T. L., and Hong, G. F., 2010. “Heat transfer in radially rotating pin-fin channel at high rotation numbers”. *ASME Journal of Turbomachinery,* ***132***(2), pp. 021019–021030.

[16] Park, J. S., Kim, K. M., Lee, D. H., Cho, H. H., and Chyu, M., 2011. “Heat transfer in rotating channel with inclined pin-fins”. *ASME Journal of Turbomachinery,* ***133***(2), pp. 021003–021010.

[17] Parsons, J. A., Han, J. C., and Lee, C. P., 120. “Rotation effect on jet impingement heat transfer in smooth rectangular channels with four heated walls and radially outward cross”. *ASME Journal of Heat Transfer,* ***120***(1), pp. 79–85.

[18] Parsons, J. A., and Han, J. C., 2005. “Jet impingement heat transfer in rotating channels with staggered extraction flow”. *AIAA Journal of Thermophysics and Heat Transfer,* ***19***(2), pp. 156–162.

[19] Akella, K. V., and Han, J. C., 1999. “Impingement channel cooling in rotating two-pass rectangular channel with ribbed walls,”. *AIAA Journal of Thermophysics and Heat Transfer,* ***13***(3), pp. 364–371.

[20] Griffith, T. S., Al-Hadhrami, L., and Han, J. C., 2002. “Heat transfer in rotating rectangular cooling channels (ar=4) with angled ribs”. *ASME Journal of Heat Transfer,* ***124***(4), pp. 617–625.

[21] Wright, L. M., Fu, W. L., and Han, J. C., 2005. “Influence of entrance geometry on heat transfer in rotating rectangular cooling channels (ar=4:1) with angled ribs”. *ASME Journal of Heat Transfer,* ***127***(4), pp. 378–387.

[22] Al-Hadharami, L., Griffith, T., and Han, J. C., 2003. “Heat transfer in two-pass rotating rectangular channels (ar=2) with five different orientations of 45 deg v-shaped turbulators”. *ASME Journal of Heat Transfer,* ***125***(2), pp. 232–242.

[23] Fu, W. L., Wright, L. M., and Han, J. C., 2005. “Heat transfer in two-pass rotating rectangular channels (ar=1 : 2 and ar=1 : 4) with smooth walls”. *ASME Journal of Heat Transfer,* ***127***(3), pp. 265–277.

[24] Fu, W. L., Wright, L. M., and Han, J. C., 2005. “Heat transfer in two-pass rotating rectangular channels (ar=1:2 and ar=1:4) with 45 deg angled rib turbulators”. *ASME Journal of Turbomachinery,* ***127***(1), pp. 164–174.

[25] Zhou, F., Lagrone, J., and Acharya, S., 2007. “Internal cooling in 4 : 1 ar passages at high rotation numbers”. *ASME Journal of Heat Transfer,* ***129***(12), pp. 1666–1675.

[26] Fu, W. L., Wright, L. M., and Han, J. C., 2006. “Heat transfer in two-pass rotating rectangular channels (ar=2:1) with discrete ribs”. *AIAA Joural of Thermophysics and Heat Transfer,* ***20***(3), pp. 569–582.

[27] Parsons, J. A., Han, J. C., and Zhang, Y., 1995. “Effect of model orientation and wall heating condition on local heat transfer in a rotating two-pass square channel with rib turbulators”. *International Journal of Heat and Mass Transfer,* ***38***(7), pp. 1151–1159.

[28] Dutta, S., and Han, J. C., 1996. “Local heat transfer in rotating smooth and ribbed two-pass square channels with three channel orientations”. *ASME Journal of Heat Transfer,* ***118***(3), pp. 578–584.

[29] Park, C. W., and Lau, S. C., 1998. “Effect of channel orientation of local heat (mass) transfer distributions in a rotating two-pass square channel with smooth walls”. *ASME Journal of Heat Transfer,* ***120***(3), pp. 624–632.

[30] Dutta, S., Han, J. C., and Lee, C. P., 1996. "Local heat transfer in a rotating two-pass ribbed triangular duct with two model orientations". *International Journal of Heat and Mass Transfer,* ***39***(4), pp. 707–715.

[31] Dutta, S., Han, J. C., and Lee, C. P., 1995. "Experimental heat transfer in a rotating triangular duct: Effect of model orientation". *ASME Journal of Heat Transfer,* ***117***(4), pp. 1058–1061.

[32] Lee, D. H., Rhee, D. H., Kim, K. M., Cho, H. H., and Moon, H. K., 2009. "Heat transfer and flow temperature measurements in a rotating triangular channel with various rib arrangements". *Heat Mass Transfer,* ***45***(12), pp. 1543–1553.

[33] Liu, Y. H., Huh, M., Han, J. C., and Moon, H. K., 2010. "High rotation number effect on heat transfer in a triangular channel with 45 deg, inverted 45 deg, and 90 deg ribs". *ASME Journal of Heat Transfer,* ***132***(7), pp. 071702–071711.

[34] Huh, M., Lei, J., Liu, Y. H., and Han, J. C., 2011. "High rotation number effects on heat transfer in a rectangular (ar=2:1) two-pass channel". *ASME Journal of Turbomachinery,* ***133***(2), pp. 021001–021011.

[35] Huh, M., Lei, J., and Han, J. C., 2012. "Influence of channel orientation on heat transfer in a two-pass smooth and ribbed rectangular channel (ar=2:1) under large rotation numbers". *ASME Journal of Turbomachinery,* ***134***(1), pp. 011022–011035.

[36] Liu, Y. H., Huh, M., Han, J. C., and Chopra, S., 2008. "Heat transfer in a two-pass rectangular channel (ar=1:4) under high rotation numbers". *ASME Journal of Heat Transfer,* ***130***(8), pp. 0817011–0817019.

[37] Chang, S. W., Liou, T. M., and Chen, W. C., 2012. "Influence of radial rotation on heat transfer in a rectangular channel with two opposite walls roughened by hemispherical

protrusions at high rotation numbers". *ASME Journal of Turbomachinery,* ***134***(1), pp. 011010–011019.

[38] Goldstein, R. J., and Cho, H. H., 1995. "A review of mass-transfer measurements using naphthalene sublimation". *Experimental Thermal and Fluid Science,* ***10***(4), pp. 416–434.

[39] Dhungel, A., 2002. "Film cooling from a row of holes supplemented with anti vortex holes". Master's thesis, Louisiana State University and Agriculteral and Mechanical College.

[40] Munson, B. R., Young, D. F., and Okiishi, T. H., 2006. *Fundamentals of Fluid Mechanics*, 5th ed. John Wiley and Sons, ch. 8.6.

[41] Budynas, R. G., Nisbett, J. K., and Shigley, J. E., 2008. *Shigley's Mechanical Engineering Design*, 8th ed. McGraw-Hill.

[42] Cooper, T. E., Field, R. J., and Meyer, J. F., 1975. "Liquid crystal thermography and its application to the study of convective heat transfer". *ASME Journal of Heat Transfer,* ***97***(3), pp. 442–450.

[43] Figliola, R. S., and Beasley, D. E., 2006. *Theory and Design for Mechanical Measurements*, 5th ed. John Wiley and Sons, ch. 7.

[44] Yan, Y., and Owen, J. M., 2002. "Uncertainties in transient heat transfer measurements with liquid crystal". *International Journal of Heat and Fluid Flow,* ***23***(1), pp. 29–35.

[45] Ekkad, S. V., and Han, J. C., 1997. "Detailed heat transfer distributions in two-pass square channels with rib turbulators". *International Journal of Heat and Mass Transfer,* ***40***(11), pp. 2525–2537.

[46] Liou, T. M., Chen, C. C., and Chen, M. Y., 2001. “Tlct and ldv measurements of heat transfer and fluid flow in a rotating sharp turning duct”. *International Journal of Heat and Mass Transfer,* ***44***(9), pp. 1777–1787.

[47] Liou, T. M., Chen, M. Y., and Tsai, M. H., 2002. “Fluid flow and heat transfer in a rotating two-pass square duct with in-line 90-deg ribs”. *ASME Journal of Turbomachinery,* ***124***(2), pp. 260–268.

[48] Taslim, M. E., and Wadsworth, C. M., 1997. “An experimental investigation of the rib surface-averaged heat transfer coefficient in a rib-roughened square passage”. *ASME Journal of Turbomachinery,* ***119***(2), pp. 381–389.

[49] Florschuetz, L. W., Truman, C. R., and Metzger, D. E., 1981. “Streamwise flow and heat transfer distributions for jet array impingement with crossflow”. *ASME Journal of Heat Transfer,* ***103***(2), pp. 337–342.

[50] Uysal, U., Li, P.-W., Chyu, M. K., and Cunha, F. J., 2005. “Heat transfer on internal surfaces of a duct subjected to impingement of a jet array with varying jet hole-size and spacing”. *ASME Journal of Turbomachinery,* ***128***(1), pp. 158–165.

[51] Gritsch, M., Schulz, A., and Wittig, A., 1998. “Discharge coefficient measurements of film-cooling holes with expanded exits”. *ASME Journal of Turbomachinery,* ***120***(3), pp. 557–563.

[52] Huang, L., and Mohamed, S. E., 1994. “Heat transfer of an impinging jet on a flat surface”. *International Journal of Heat and Mass Transfer,* ***37***(13), pp. 1915–1923.

[53] Striegl, S. A., and Diller, T. E., 1984. “An analysis of the effect of entrainment temperature on jet impingement heat transfer”. *ASME Journal of Heat Transfer,* ***106***(4), pp. 804–810.

[54] Webb, R. L., 2006. *Principles of Enhanced Heat Transfer*, 2nd ed. Taylor and Francis, New York, NY.